ALKALI METAL EXCHANGE REACTIONS

by

John Christopher Whitehead

of

Queens' College,
Cambridge.

A dissertation submitted in partial fulfilment
of the requirement for the degree
of Doctor of Philosophy in the University of Cambridge.

October 1972

To My Parents

and

Rosemary.

ABSTRACT

The technique of crossed molecular beams has been employed to study the elastic and reactive scattering of alkali atoms and dimers. The apparatus is capable of producing a high purity beam of alkali dimers or a mixed beam of atoms and dimers. This beam is then crossed by a beam of a halogen-containing molecule or an alkali atom. The angular distributions of elastic and reactive scattering are measured.

The reactive scattering of a supersonic K beam with Br_2, BrCN, $SnCl_4$, PCl_3, CCl_4 and CH_3I has been observed. The atom beam is produced from a nozzle source giving a narrow velocity distribution, peaked at a higher velocity than the conventional thermal beam. Total reaction cross sections are found to decrease with energy, those for Br_2, BrCN and CCl_4, showing increased forward scattering. For $SnCl_4$, it is suggested that the observed differential reaction cross section indicates a long-lived collision complex dissociating by two reaction paths.

By comparing the elastic scattering of potassium atoms and dimers with Br_2, IBr, BrCN and $SnCl_4$, approximate laboratory and centre of mass angular distributions of reactive K atom scattering from K_2 + Br_2, IBr and BrCN are presented. Comparison is made with the existing KBr, KCN angular distributions and provides more detailed insight into the four centre reaction dynamics. For K_2 + $SnCl_4$ no reactively scattered K atom was found.

Semi-empirical potential-energy surfaces for alkali-metal exchange reaction have been calculated using methods based on the London equation and the method of "diatomics-in-molecules". Results are presented for the systems Li + Li_2, Na + Li_2, Li + NaLi, Li + Na_2,

Na + LiNa and Na + Na_2.

The scattering of Na + K_2, Rb_2, Cs_2; K + Rb_2; Cs + Rb_2, K_2 and Rb + K_2 has been observed by modifying the existing apparatus to provide an alkali atom source and a quadrupole mass filter detector. For Na + K_2, Rb_2, Cs_2 and K + Rb_2 the reactive and elastic scattering can be kinematically separated, although no definitive distribution of reaction products can be determined. The total reaction cross sections are large ($\sim 100 \text{Å}^2$) and are compatible with the reaction being governed by long range van der Waals forces.

Finally, angular distributions of the elastic scattering of alkali atom - alkali atom systems have been obtained. The systems studied are K + Na, Cs, Rb; Rb + Cs, K, Na and Cs + Na. Structure due to rainbow scattering is observed for K + Cs, Rb and Rb + Cs and the triplet well depths estimated.

PREFACE

This work was carried out in the University Chemical Laboratory, Cambridge under the supervision of Dr. R. Grice. It was performed on the molecular beam reactive scattering apparatus, designed and constructed by G. M. Kendall and P. B. Foreman, which was modified by myself for the experiments of Chapters IV and V. The experimental data, analysed in Chapters I and II was obtained jointly with D. R. Hardin. The work is otherwise original.

ACKNOWLEDGEMENTS

There are many people without whose labours, ideas, advice and encouragement this work would not have been possible. Firstly, I must thank my supervisor, Dr. Roger Grice, whose advice, encouragement and endless energy saw this project through from its conception to its conclusion. His insight and guidance have contributed greatly to my scientific education. Gerry Kendall and Paul Foreman, who designed and built Aphrodite and passed on their accumulated knowledge and expertise with great patience. Doug Hardin, with whom I first ran experiments, has helped me in many ways during the last three years.

I have also enjoyed the friendship and benefited from the knowledge of many present members of the molecular beams group and of the theoretical chemistry department.

Much of the success of this project is due to the technical staff of the department, particularly the workshops who did excellent work in producing the pieces of equipment described here.

I would also like to acknowledge an S.R.C. Research Studentship.

Finally, I must thank Rosemary, who has helped me in many ways, not least of which are proof reading the manuscript and printing all the figure drawings.

INDEX

CHAPTER I

REACTIVE SCATTERING OF A SUPERSONIC ALKALI BEAM: $K + Br_2$, BrCN, $SnCl_4$, PCl_3, CCl_4 and CH_3I

Introduction

The reactions of alkali atoms with halogen-containing molecules have been extensively studied at thermal energies (1). Angular distribution measurements (2-8) and more recently velocity analysis measurements over a wide angular range (9-13) have given a comprehensive picture of the variation in dynamics as the halogen-containing molecule changes from the diatomic halogens (2-5, 9, 11) through triatomic (6) and polyhalide molecules (7, 13) to the alkyl halides (8, 10, 12). The dynamics are well explained by an electron jump model (1) in which charge transfer occurs in the entrance valley of the potential surface

$$M + XY \longrightarrow M^+XY^- \longrightarrow M^+X^- + Y \quad (1)$$

However, work has mostly been confined to thermal initial kinetic energies ($E \sim 1.0 - 1.5$ kcal mole^{-1}) except that of Gersch and Bernstein (14) who accelerated CH_3I in a seeded nozzle beam ($E \sim 13$ kcal mole^{-1}). The dependence of the reactive scattering on initial kinetic energy, especially for a series of molecules, is likely to provide further insight into the dynamics. Indeed, it has been suggested (15-18) that the covalent potential surface is lowered for internuclear distances greater than the electron jump radius ($R > R_c$) sufficiently to perturb trajectories at thermal energies. Thus we would expect trajectories in this region to be sensitive to the initial kinetic energy.

Recent studies of potassium dimer reactive scattering have drawn heavily (19, 20) on the analogous alkali atom reactions in their interpretation. However, initial kinetic energies for potassium dimers formed in a Laval nozzle expansion (21) ($E \sim 8.5$ kcal mole^{-1})

are well above the thermal energy range. Thus measurement of potassium atom scattering at energies above the thermal range would provide a more reliable basis for comparison. Such studies are especially inviting since the potassium dimer source produces (21) a potassium atom flux of almost the same velocity distribution as the dimers and three times more intense. Indeed, some of the K atom elastic scattering data from the present measurements has been employed (22) to estimate angular distributions of reactively scattered K atoms in the analogous K_2 dimer reactions.

Experimental Conditions

The apparatus and procedures used in these experiments were the same as those employed (20, 21) in the potassium dimer studies, where an inhomogeneous magnetic field deflected potassium atoms, and allowed only dimers to pass into the scattering chamber. If the magnet energizing current is switched off, the atoms are undeflected and a mixed potassium atom and dimer beam enters the scattering chamber. Thus in a series of scattering measurements made with the magnet off and then on at each angle, the scattering due to potassium atoms may be obtained simply by subtraction. As before the scattered signal is measured on a W filament which ionises potassium dimers, atoms and halides and on a Pt/W filament which is insensitive to potassium halides. The potassium atom beam intensity $\sim 3.5 \times 10^{-8}$A is attenuated by $\sim$ 5% by the cross beam, giving an alkali halide product intensity $\sim 1 \times 10^{-12}$A corresponding to $\sim 1 \times 10^{9}$ molecule cm^{-2} sec^{-1} at the peak of the product distribution.

Results

The primary data for K + Br_2, BrCN and CH_3I are shown in Fig.1; for K + $SnCl_4$, CCl_4 and PCl_3 in Fig.2. Relative intensity (signal at angle Ⓗ divided by K atom beam attenuation) is plotted logarithmically against laboratory scattering angle Ⓗ (the K beam is at Ⓗ = 0° and the cross beam at Ⓗ = 90°). It is apparent that the relative intensity measured on the W filament falls off much more slowly at wide angles than that measured on the Pt/W filament. This discrepancy is greatest for Br_2 and least for CH_3I. Comparison of this raw data with that obtained with thermal Maxwell Boltzmann alkali beams (1-8) reveals a higher resolution in the present experiments. The shape and peak position of the KX distribution is immediately apparent from inspection of the data. This is particularly noticeable in the CCl_4 data where peaks at Ⓗ = 50°, -45° are clearly resolved. This contrasts with the thermal K + CCl_4 scattering (7) where magnetic deflection analysis (23) was necessary to confirm a bimodal distribution of this kind. The resolution arises from a rapid fall in the elastic scattering for Ⓗ > 10° which is due to the narrow velocity distribution and high velocity of the alkali nozzle beam.

Elastic Scattering. The laboratory angular distribution measured on the Pt/W filament is transformed to the centre of mass system using the kinematic relations appropriate to the most probable velocity in each parent beam; $1.86\alpha_o$ for K (21) and α_o for the cross beam, where α_o is the most probable velocity of a Maxwell-Boltzmann beam in each case. The intensity in centre of mass coordinates $I_{cm}(\Theta)$ weighted by $\sin\Theta$ is shown as a function of the centre of mass scattering angle Θ in figure 3. The small angle scattering ($\Theta \leq 10°$) for Br_2, BrCN, $SnCl_4$ shows no rainbow structure but such structure is resolved

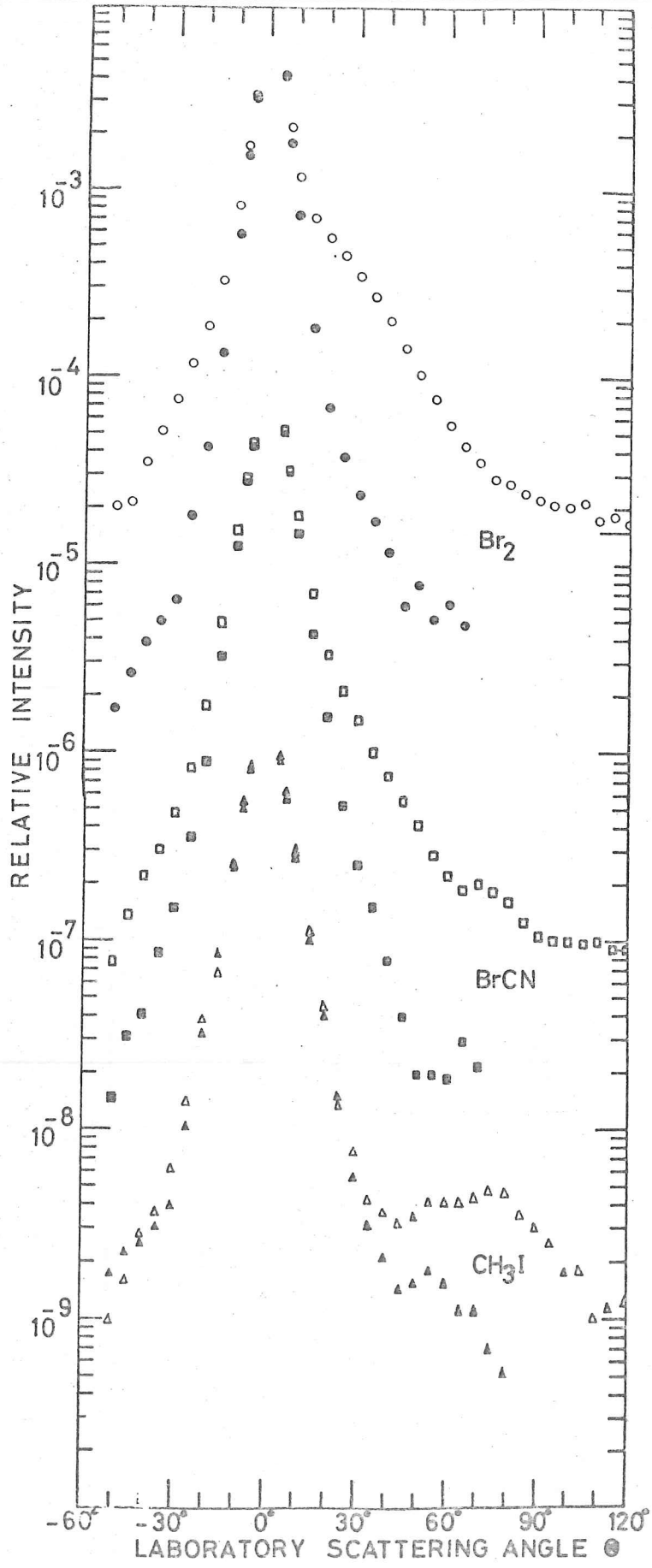

Figure 1: Primary data for K + Br_2, BrCN, CH_3I, laboratory system. Successive curves are shifted by two decades for clarity. Open symbols are signals on W filament, solid symbols on Pt/W filament.

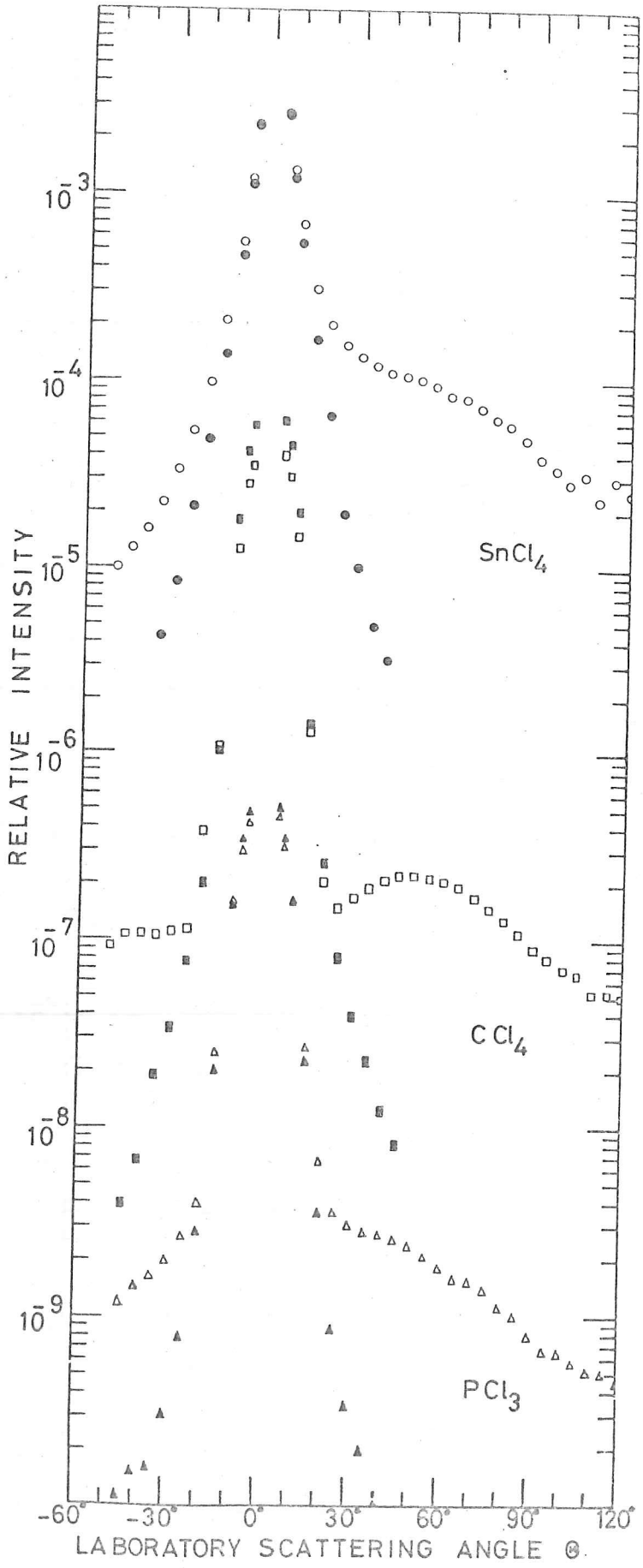

Figure 2: Primary data for K + $SnCl_4$, CCl_4, PCl_3, laboratory system. Successive curves are shifted by two decades for clarity. Open symbols are signals on W filament, solid symbols on Pt/W filament.

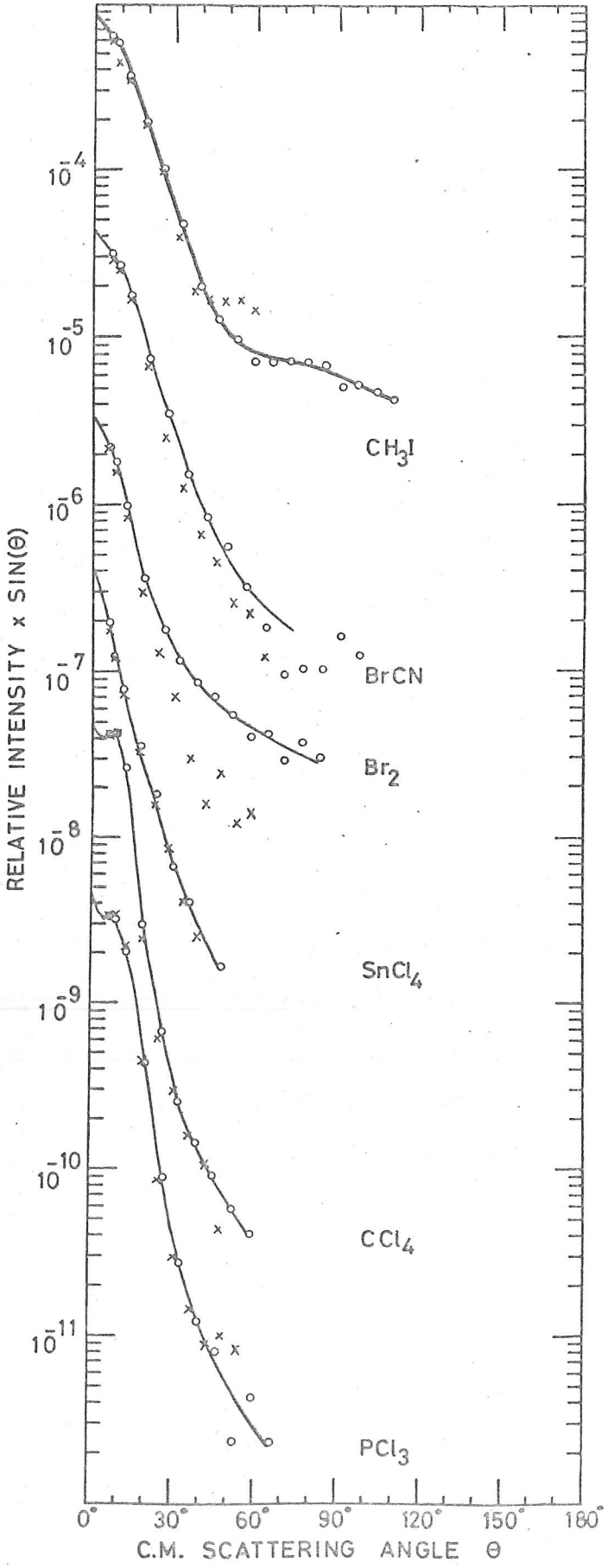

Figure 3: Angular distributions of elastic scattering in centre of mass coordinates by transformation of Pt/W data. Successive curves are shifted by one decade for clarity. Open symbols denote principal branch, crosses negative branch.

for PCl_3, CCl_4 and partially resolved for CH_3I. As previous alkali atom elastic scattering measurements (17, 24, 25) have shown, this indicates that for Br_2, BrCN, $SnCl_4$ reaction occurs at large impact parameters, comparable to the van der Waals radius r_m. However, reaction occurs only at smaller impact parameters for PCl_3, CCl_4, CH_3I. The rainbow structure for CH_3I is probably (17) distorted by lack of spherical symmetry in CH_3I.

The high intensity of the K beam permits measurement of elastic scattering out to wider angles than has previously been the case (24) at energies ~ 5 kcal.mole^{-1}; (17) apart. All the distributions fall off more rapidly at wide angles than would be predicted (17) by a Lennard-Jones potential. This absence of repulsive wall elastic scattering is due to reaction occurring for smaller impact parameter collisions, and has been extensively investigated (17, 24, 25) by means of optical potential models. The two branches of the $K + Br_2$ data show some disagreement at wide angles which probably arises from ionization of a small fraction of the vibrationally excited KBr reaction product by the Pt/W filament (26, 17). Thus the accurate distribution probably falls more rapidly (17) as in the case of $SnCl_4$. The CH_3I distribution, however, does show much higher intensity at wide angles than the other molecules, indicating that the repulsive wall elastic scattering at small impact parameters is not fully quenched by reaction (17) in this case.

Reactive Scattering. The laboratory angular distributions of reactively scattered alkali halide (or cyanide) are determined by subtracting the Pt/W from the W relative intensity. The results are shown in figures 4 - 9, together with Newton diagrams constructed for the most probable velocities in the parent beams. Spheres (shown in

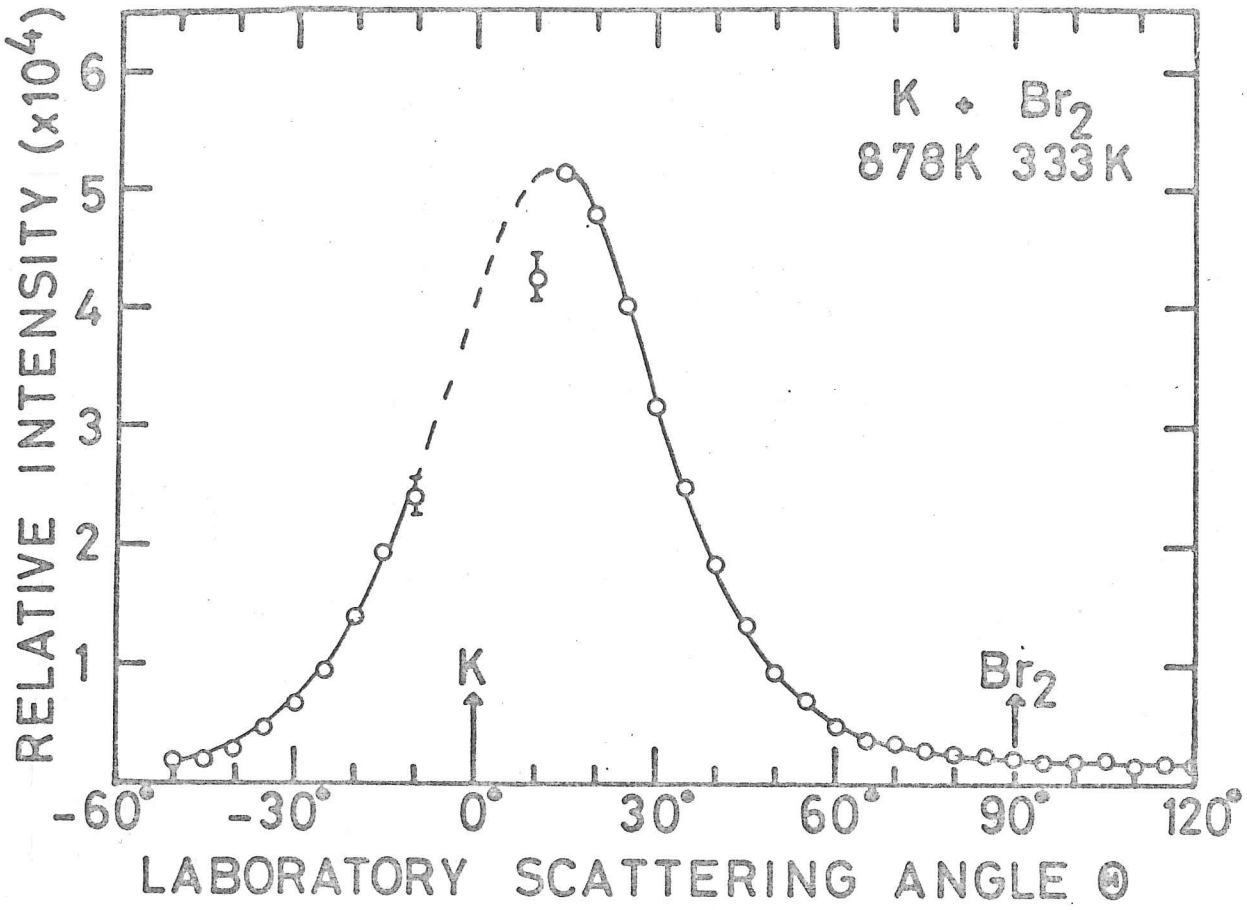

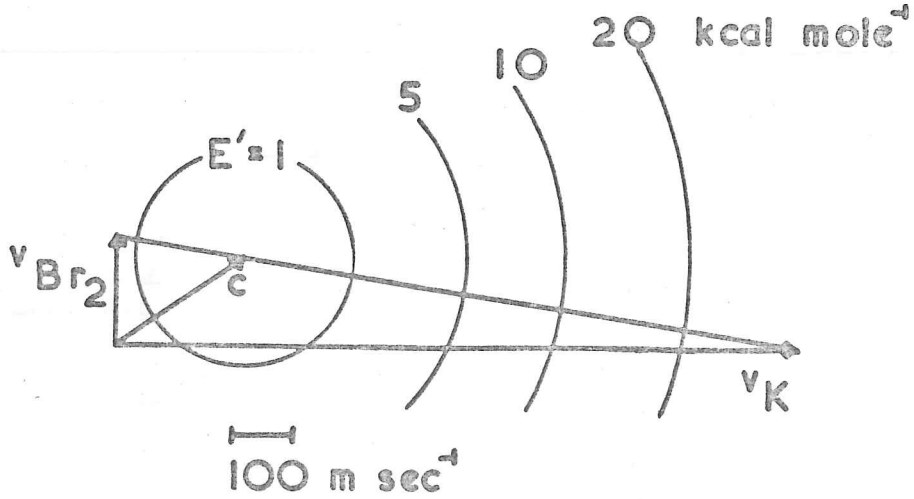

Figure 4: Angular distribution of reactively scattered KBr from K + Br_2 , laboratory system, with Newton diagram.

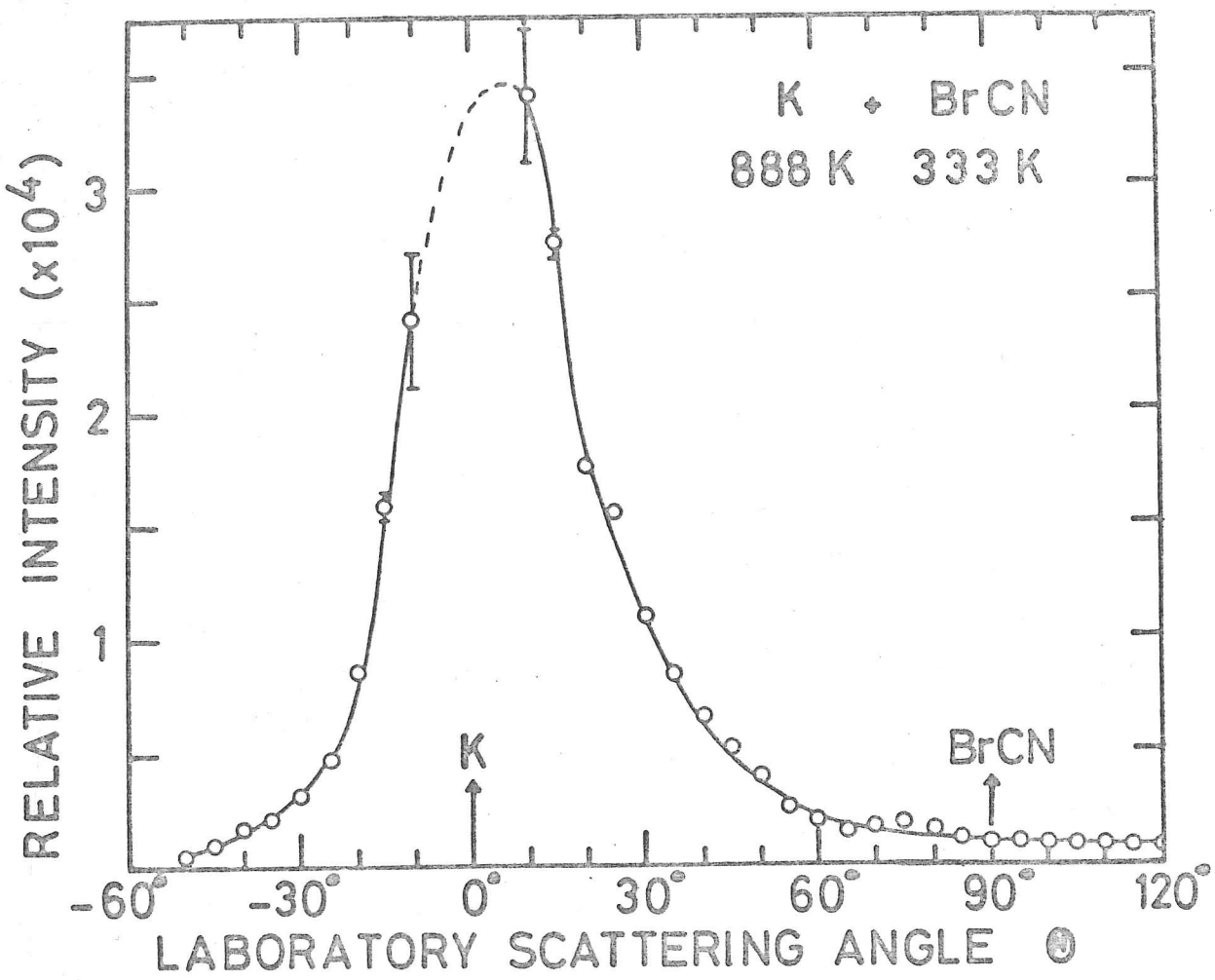

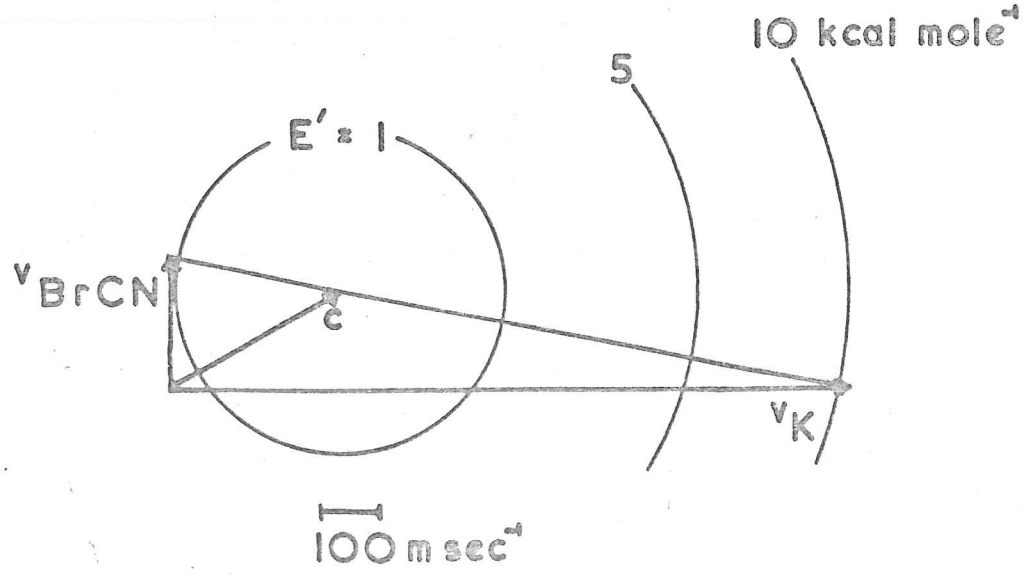

Figure 5: Angular distribution of reactively scattered KBr or KCN from K + BrCN, laboratory system, with Newton diagram.

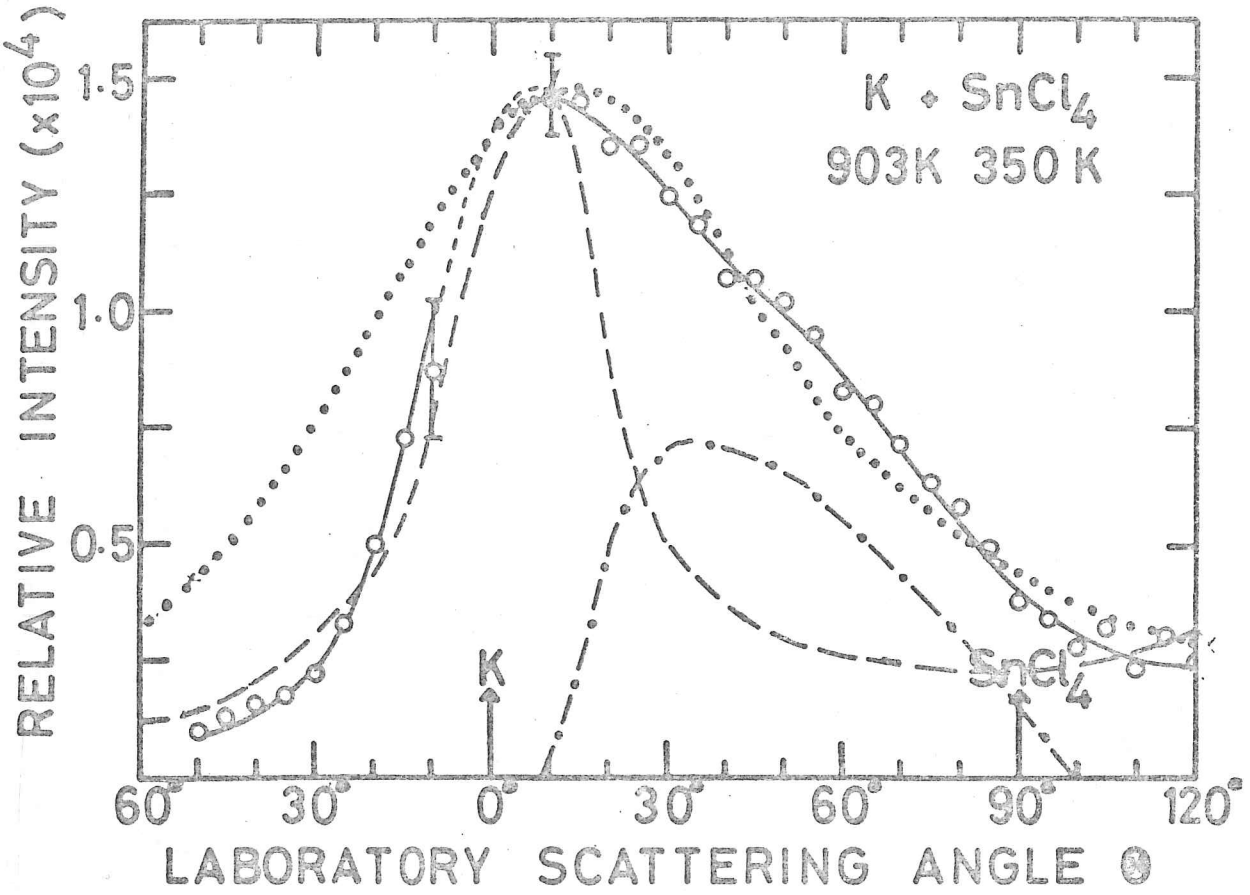

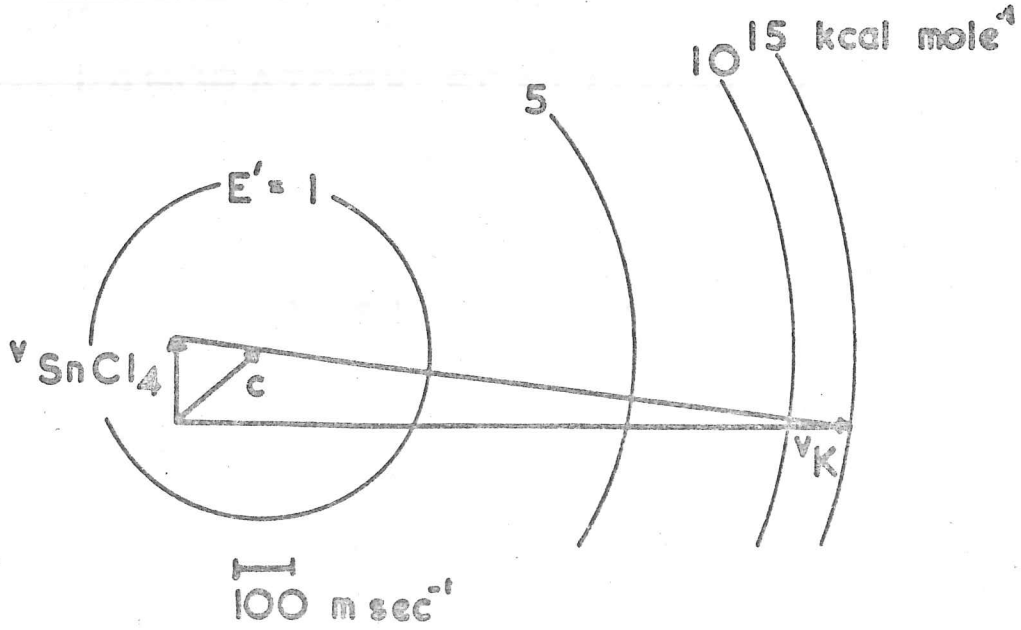

Figure 6: Angular distribution of reactively scattered KCl from K + $SnCl_4$, laboratory system, with Newton diagram. Dotted curve shows fit of stripping distribution, dashed curve complex distribution, dot-dashed curve 'low velocity' contribution.

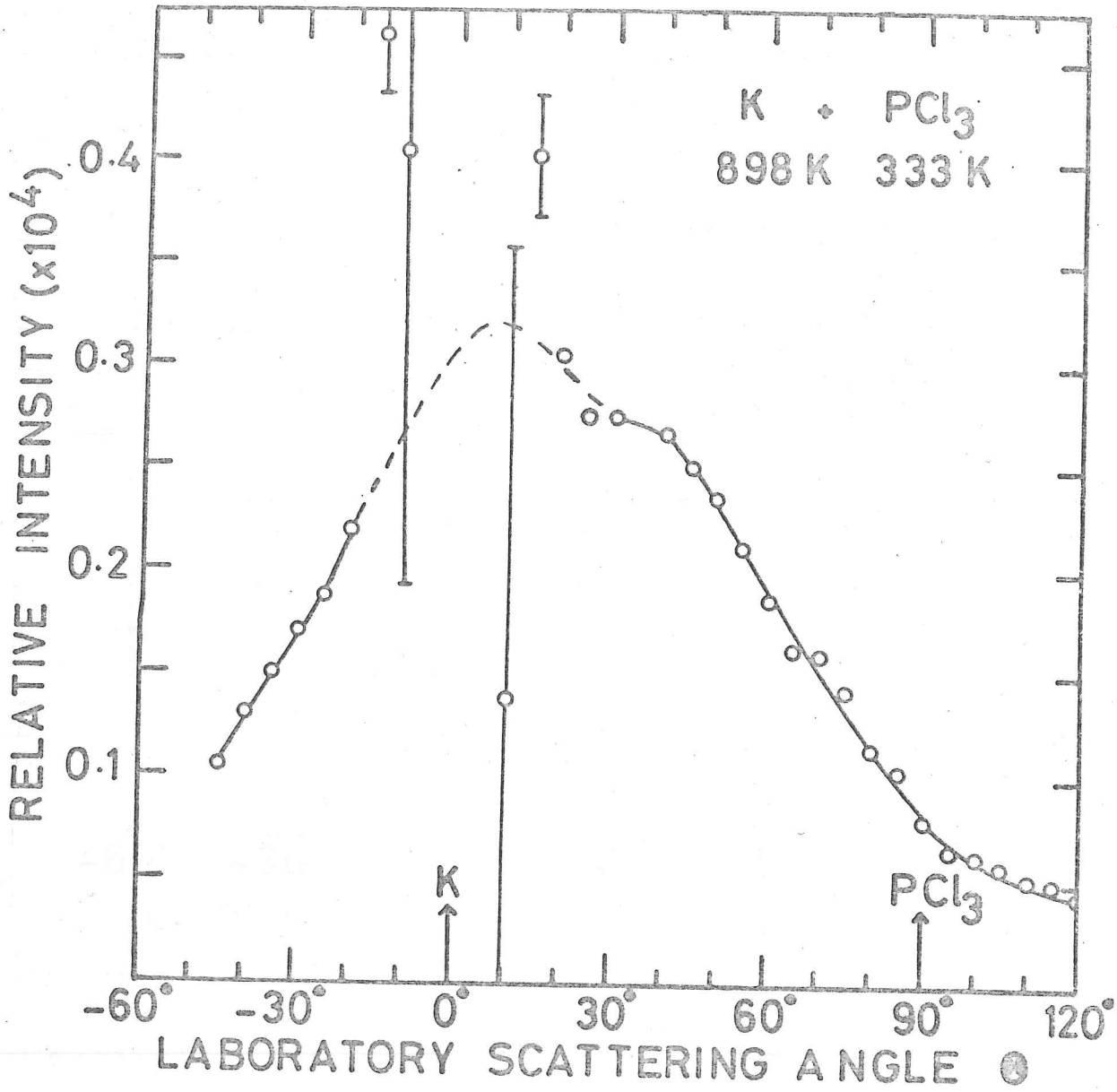

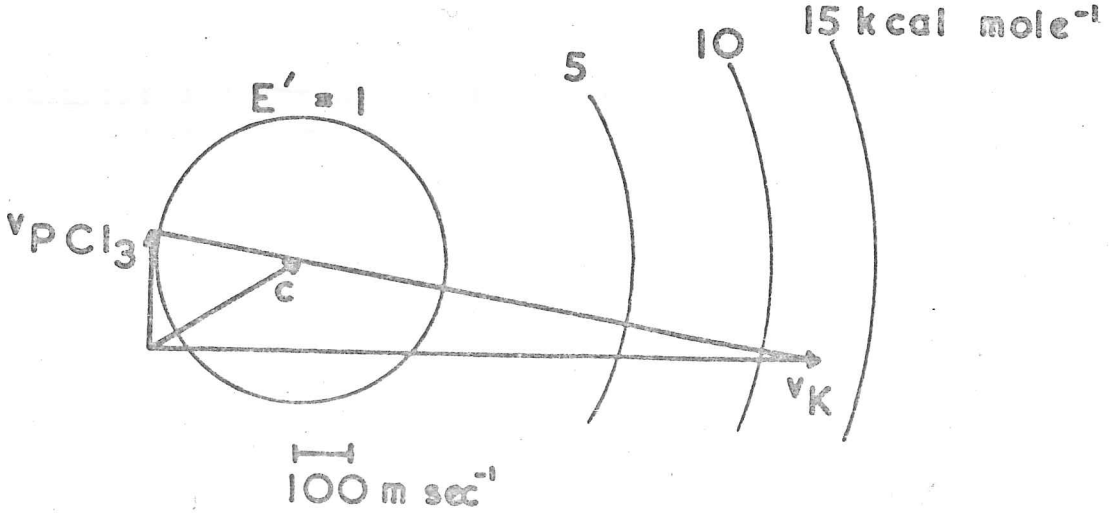

Figure 7: Angular distribution of reactively scattered KCl from K + PCl_3, laboratory system, with Newton diagram.

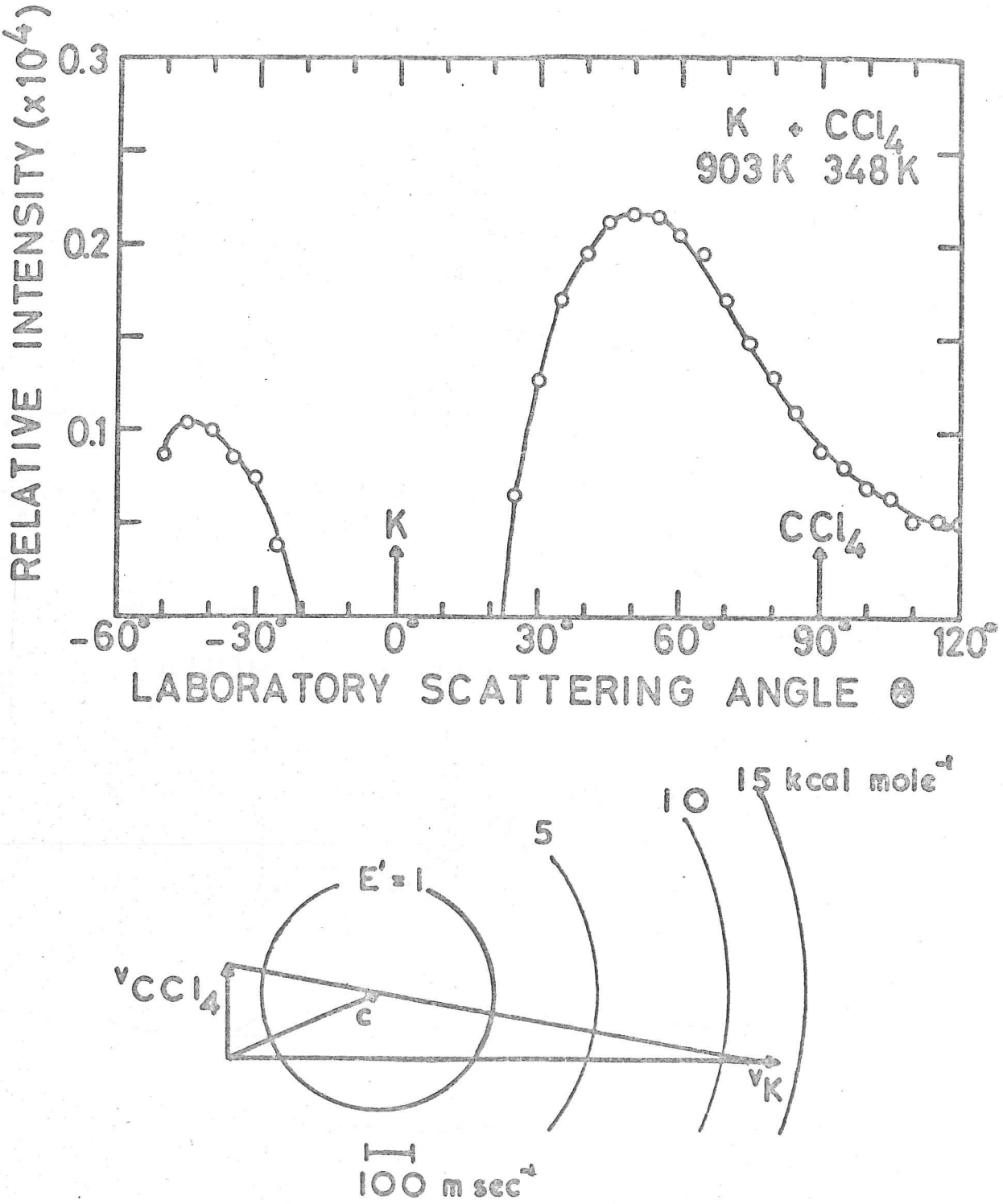

Figure 8: Angular distribution of reactively scattered KCl from K + CCl_4, laboratory system, with Newton diagram.

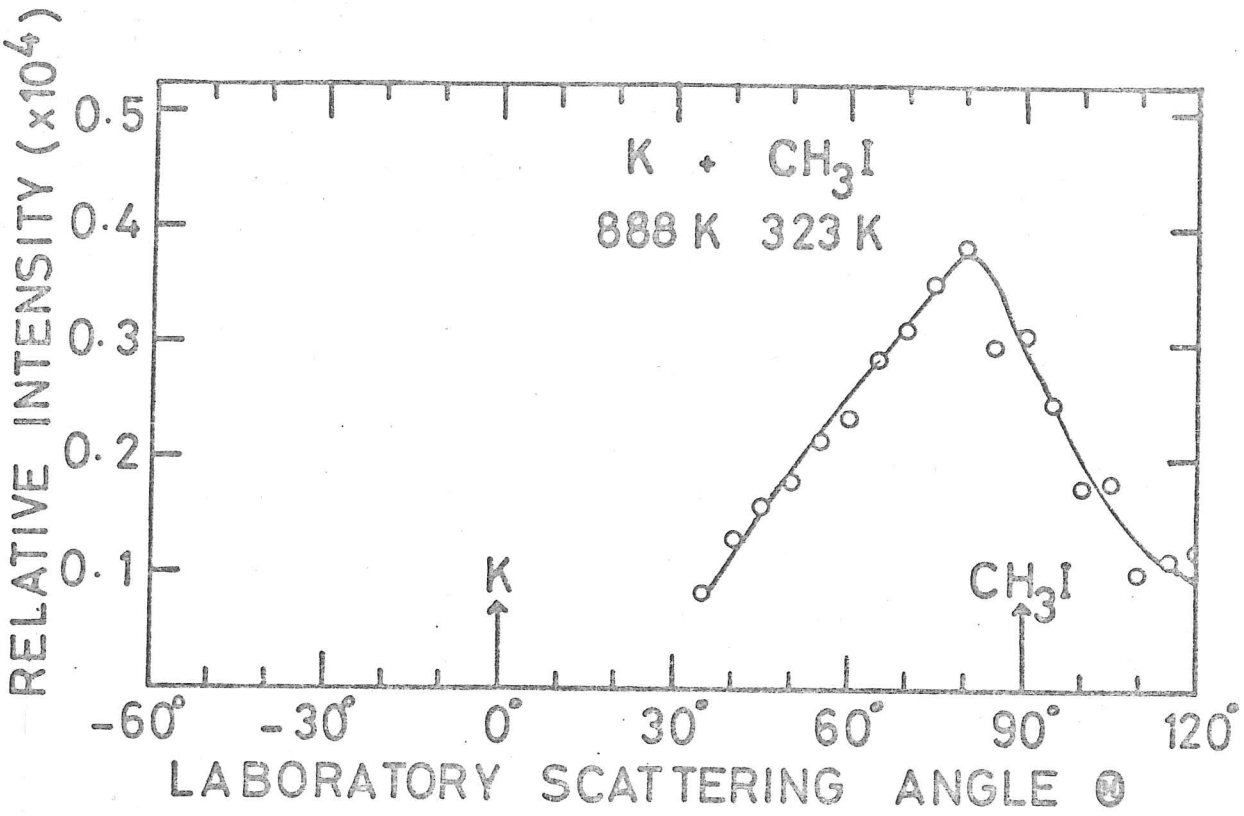

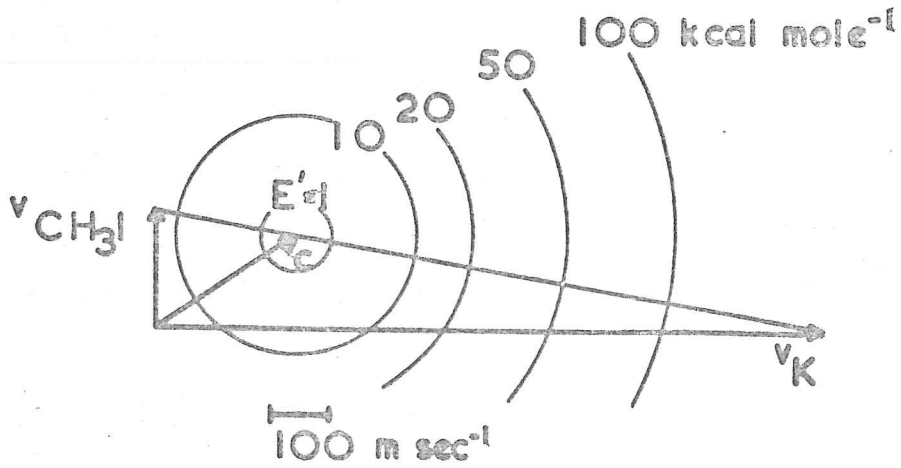

Figure 9: Angular distribution of reactively scattered KI from K + CH_3I, laboratory system, with Newton diagram.

part) about the tip of the centre of mass velocity vector $\underline{c}$ indicate the spectrum of recoil velocity vectors accessible to alkali halide with product relative translational energy E'. The data are least accurate at small laboratory scattering angles ($\Theta \leqslant 10^{o}$) since the intensity of reactive scattering is here much lower than the elastic scattering. However, for even slightly larger scattering angles ($\Theta \gtrsim 15^{o}$) the subtraction of elastic scattering becomes insignificant due to the rapid fall in the Pt/W data. The distributions for Br_2, BrCN peak sharply at small scattering angles close to the K beam. Comparison with the Newton diagrams indicates that this corresponds to KBr or KCN recoiling in the forward direction in centre of mass coordinates. The distributions for $SnCl_4$, PCl_3 also show peaking at small scattering angles but they are much broader, showing substantial intensity at wide angles. In view of the elongated Newton diagrams, Jacobian factors (27, 28) are expected to have a considerable distorting effect and the centre of mass distribution cannot be surmised accurately by inspection. The distribution for CCl_4 shows two distinct peaks (at $\Theta \simeq 50^{o}, -45^{o}$) and comparison with the Newton diagram suggests a sideways peaked centre of mass distribution. Finally, the distribution for CH_3I shows a peak at wide angles ($\Theta \simeq 80^{o}$) corresponding to backward peaking in the centre of mass system. This variation in scattering with cross beam molecule is very similar to that observed in thermal energy scattering (2-8). Thus the data must be transformed to the centre of mass coordinate system in order to make detailed comparison with the thermal energy differential cross sections.

Firstly, the laboratory angular distributions are transformed to the centre of mass coordinate system using the FV approximation (27),

in which the alkali halide centre of mass velocity vectors are taken to lie on a single velocity sphere. The magnitude of the centre of mass velocity is varied until redundant branches of the centre of mass angular distribution from different regions of the laboratory distribution, are brought into agreement. The resulting centre of mass differential cross sections are shown in figures 10 - 15. The results for Br_2 and BrCN, shown in figures 10 and 11, show sharp peaking in the forward direction ($\Theta = 0^o$). Comparison with the thermal cross sections (2, 6), shown as dashed curves, reveals little change in the magnitude of the forward peak.* However, there is a dramatic diminution by a factor~4 in the intensity in the backward hemisphere. The distributions for $SnCl_4$ and PCl_3, shown in figures 12, 13, are much flatter than the Br_2, BrCN stripping distributions. The $SnCl_4$ intensity is much higher than that for PCl_3, but the quality of agreement between the two branches for $SnCl_4$ is clearly extremely dubious and throws considerable doubt on the validity of the FV approximation in this case. The distribution for CCl_4, shown in figure 14, exhibits clear sideways peaking at $\Theta = 65^o$, comparable in intensity with the PCl_3 data at wide angles. Thermal energy FV differential cross sections are available (27) only for Cs + $SnCl_4$, Rb + PCl_3 and Rb + CCl_4. Since the change of alkali atom may alter the reaction dynamics more than the variation with energy for a given alkali (K), these thermal energy distributions are not shown for comparison, but they display qualitatively similar shapes but with considerably higher intensity. The centre of mass distribution for CH_3I, shown in figure 15, exhibits rebound behaviour, peaking in the

---

* The normalisation of the data depends on the determination of the total reaction cross section, see below, which is only approximate. Thus the exact agreement of the Br_2 forward peaks is fortuitous.

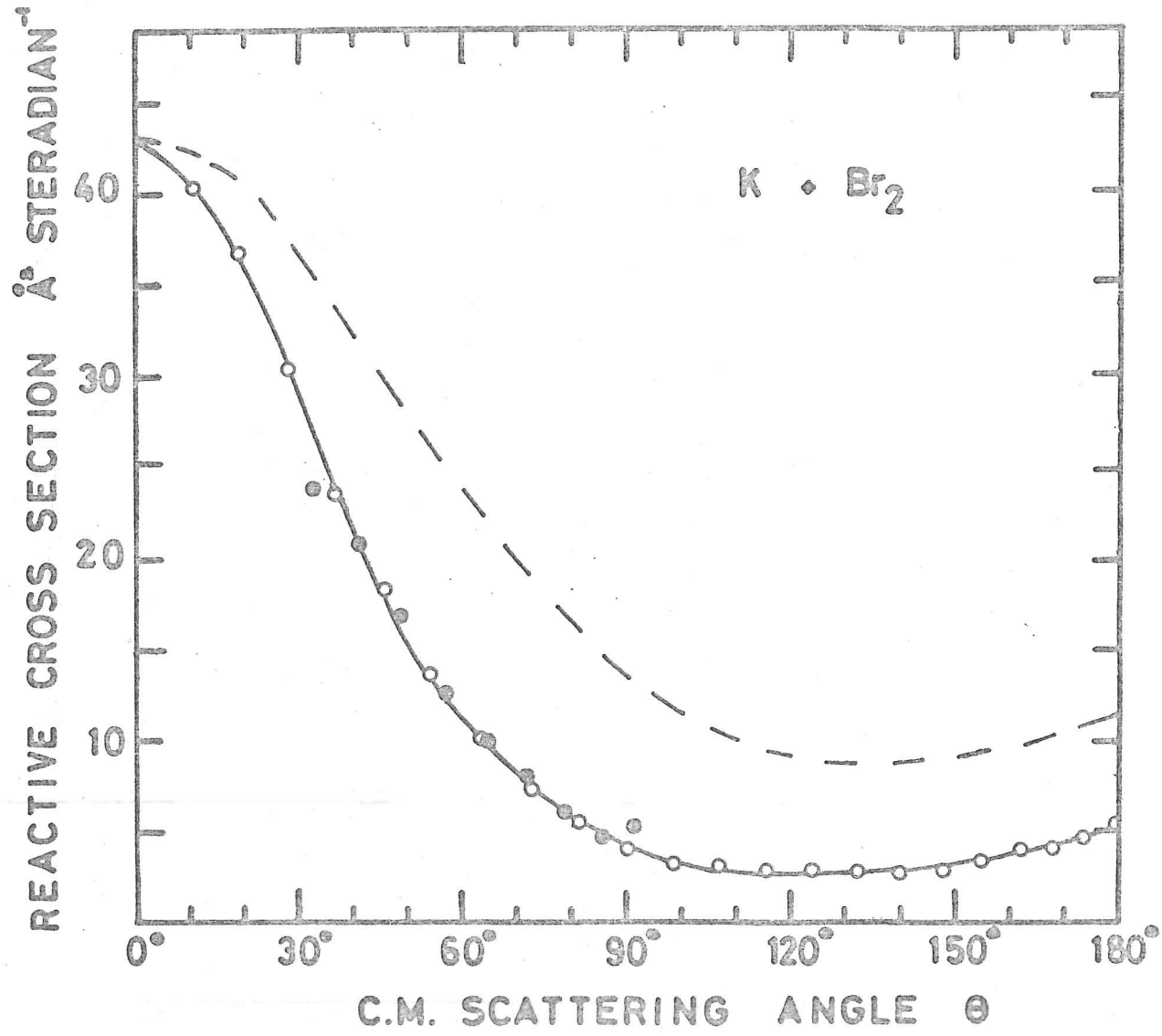

Figure 10: Differential cross section of reactively scattered KBr from K + Br_2, centre of mass system, calculated by F.V. approximation. Open symbols, positive branch; closed symbols, negative branch. Dashed curve shows cross section for thermal K + Br_2.

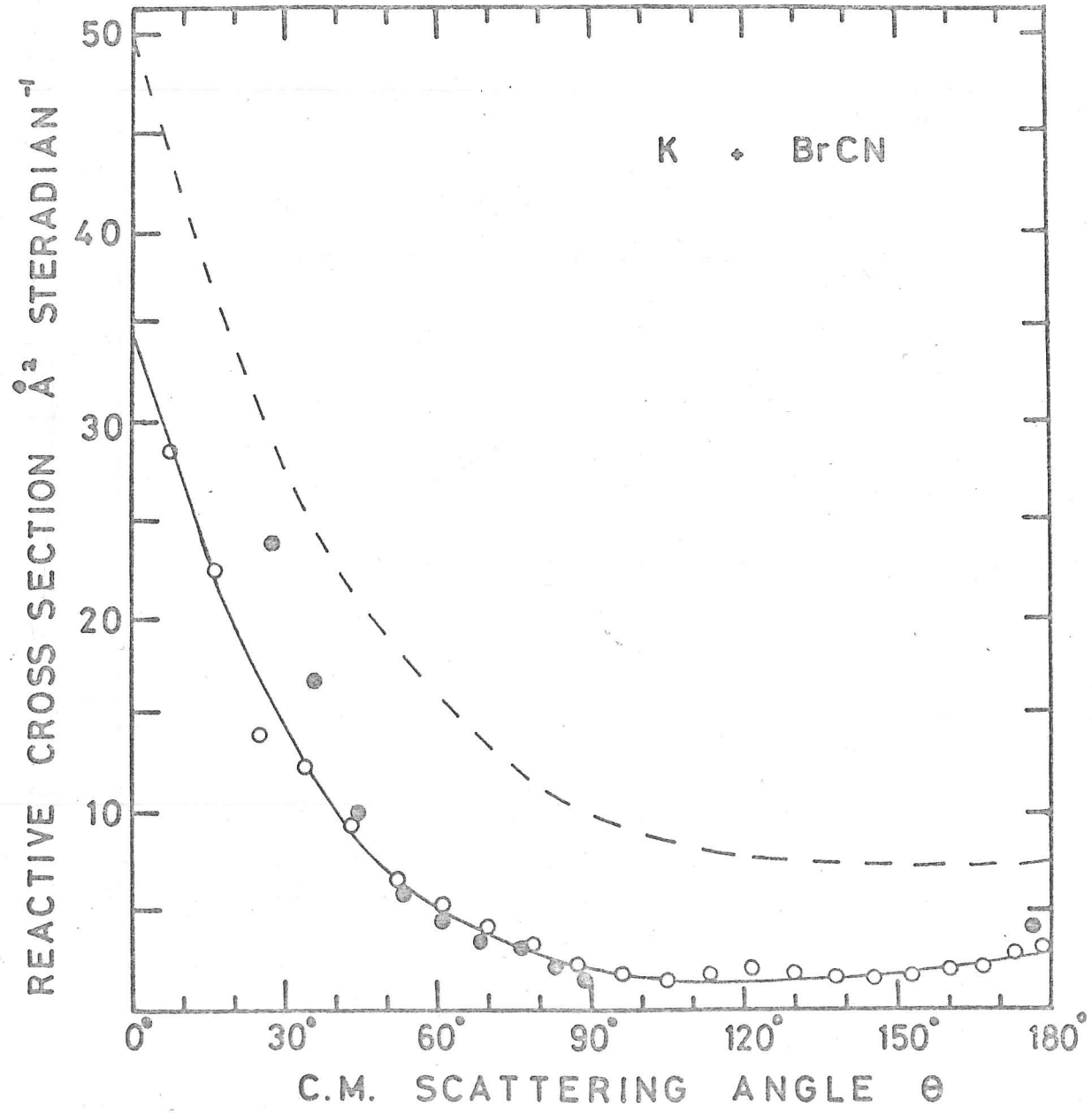

Figure 11: Differential cross section of reactively scattered KBr or KCN from K + BrCN, centre of mass system, calculated by F.V. approximation. Open symbols, positive branch; closed symbols, negative branch. Dashed curve shows cross section for thermal K + BrCN.

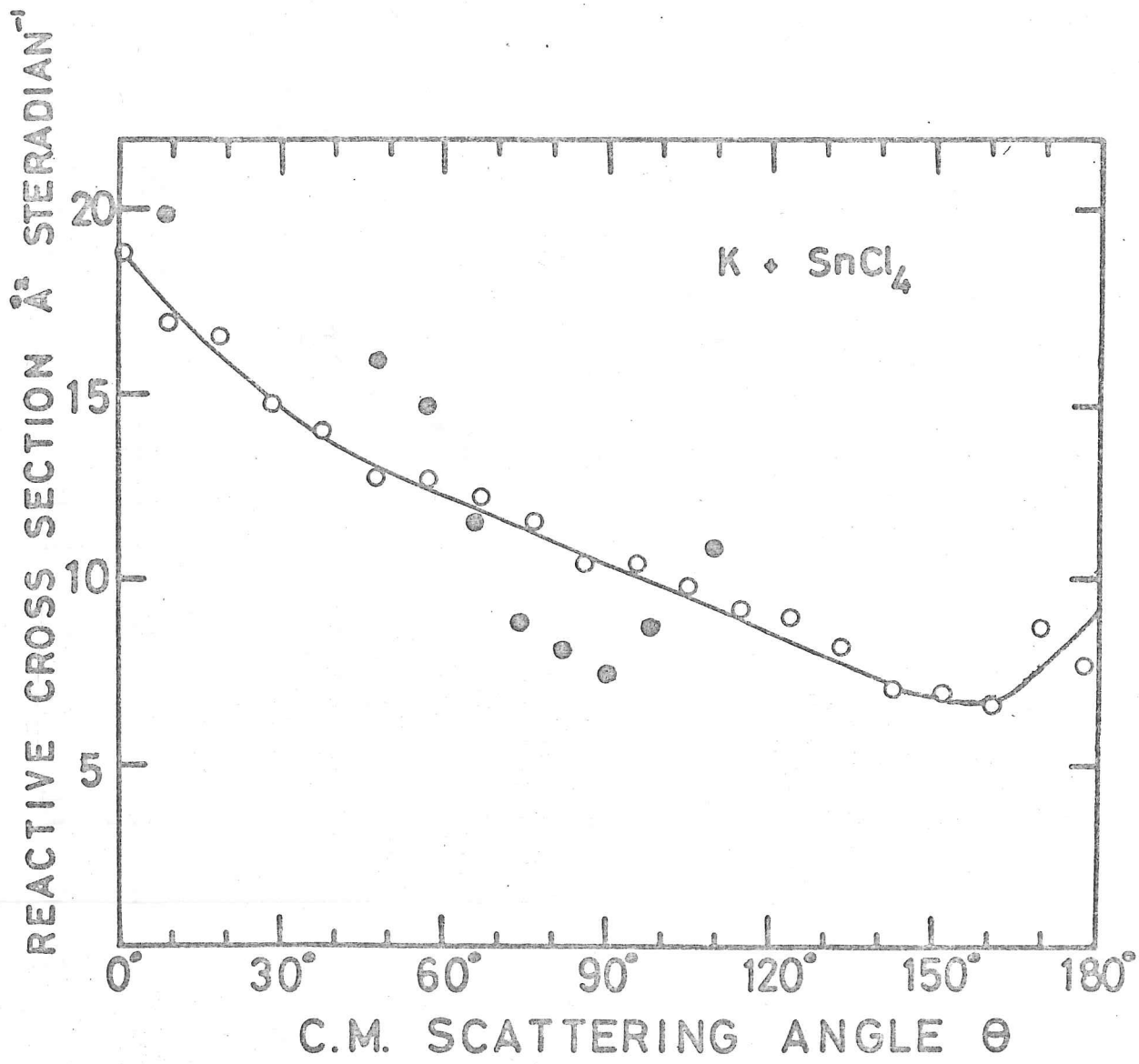

Figure 12: Differential cross section of reactively scattered KCl from K + $SnCl_4$, centre of mass system, calculated by FV approximation. Open symbols, positive branch; closed symbols, negative branch.

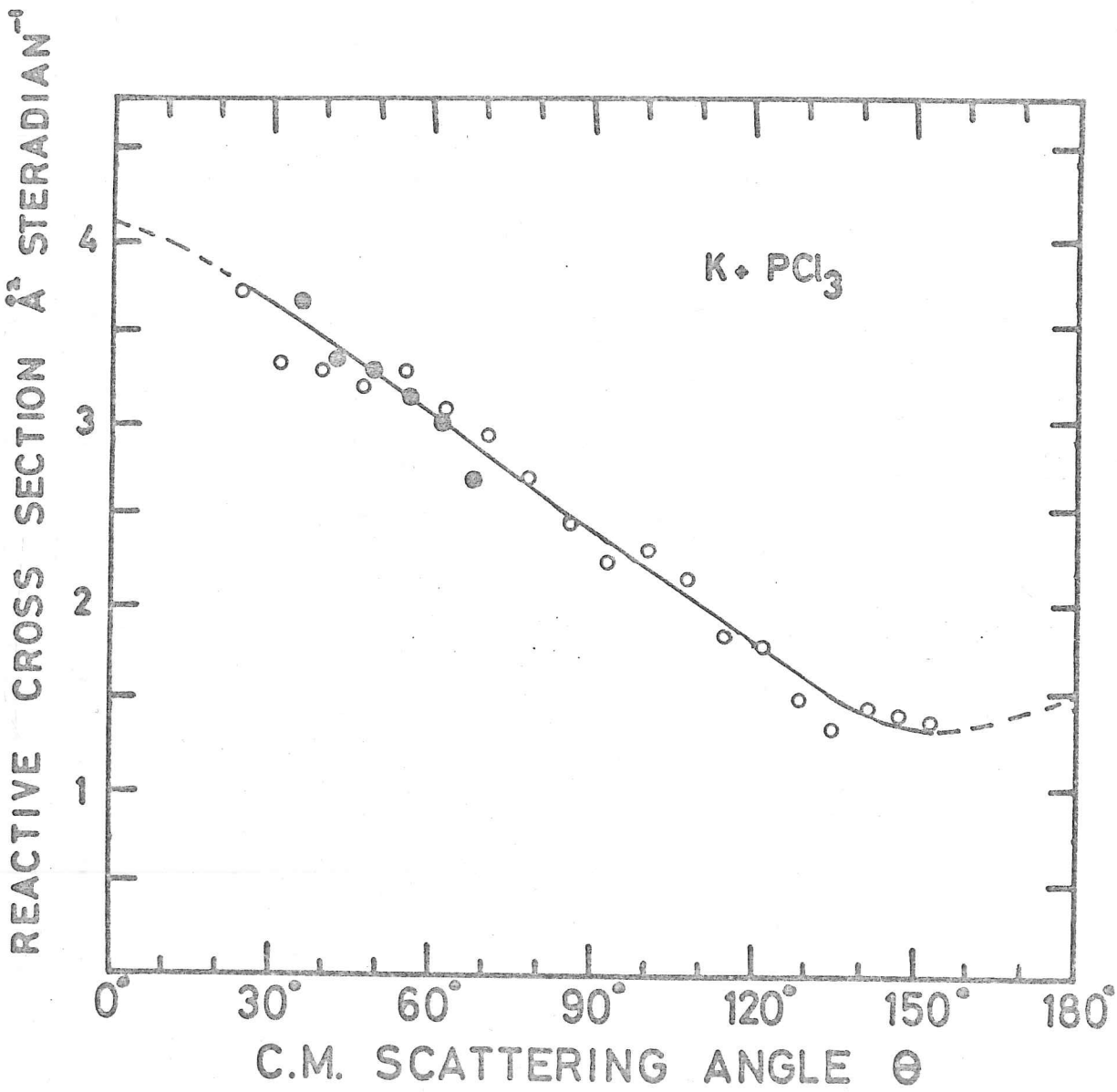

Figure 13: Differential cross section of reactively scattered KCl from K + PCl_3, centre of mass system, calculated by FV approximation. Open symbols, positive branch; closed symbols, negative branch.

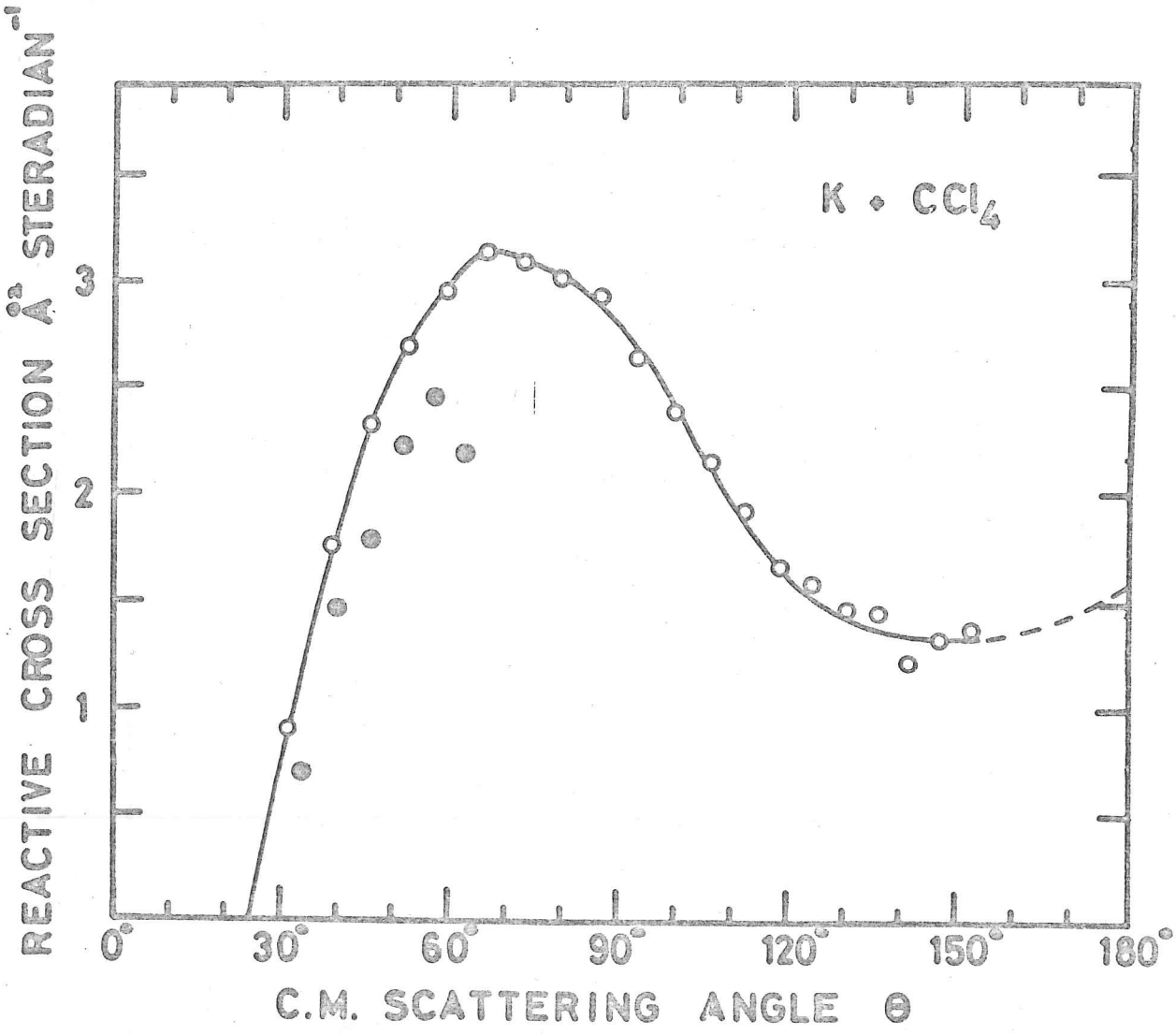

Figure 14: Differential cross section of reactively scattered KCl from K + CCl_4, centre of mass system, calculated by FV approximation. Open symbols positive branch, closed symbols, negative branch.

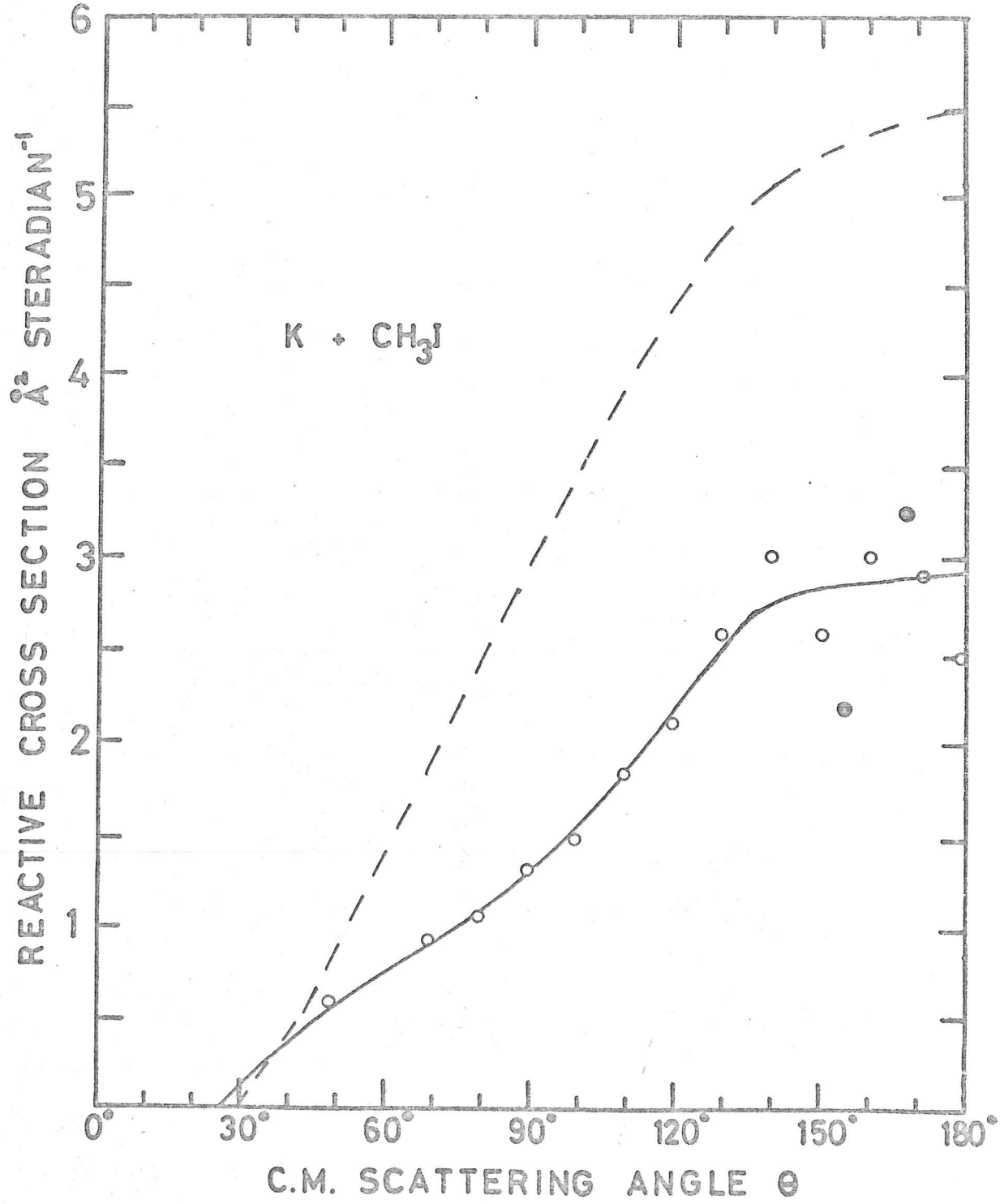

Figure 15: Differential cross section of reactively scattered KI from K + CH_3I; centre of mass system, calculated by FV approximation. Open symbols positive branch, closed symbols negative branch. Dashed curve shows cross section for thermal K + CH_3I.

backward direction, $\Theta = 180^{o}$. Comparison with the thermal K + CH_3I differential cross section (8) shown as a dashed curve, reveals a rather similar shape but uniformly higher intensity at thermal energy.

The product translational energies E' required for matching in the FV approximation are given in Table 1, as are the reactant translational energies E. Both energies are rather similar ($E \sim E'$) for the Br_2, BrCN, PCl_3 reactions. However, the product kinetic energy for the CCl_4 reaction and much more markedly the CH_3I reaction exceeds the reactant kinetic energy ($E < E'$), although reasonable matching in the FV analysis occurs over a wide range of E' for CCl_4 and an appreciable range for CH_3I. Because of the uncertainty in the FV analysis for $SnCl_4$, no estimate of E' is given, although the FV transformation of figure 12 would indicate an extremely low value of E' ($\sim \frac{1}{2}$ kcal.mole^{-1}). The reaction exoergicities ΔD_o are listed in Table 1. Only in the case of CH_3I (and possibly CCl_4) does a substantial amount of the reaction exoergicity appear in product translation.

In order to check the accuracy of the FV transformations, the centre of mass differential cross sections have also been determined by stochastic analysis (27). The angular function $T(\Theta)$ and recoil velocity function U(u) of the form employed by Entemann (27) with adjustable parameters were also used here. Initial trial values of the parameters were determined by reference to the FV results, they are then adjusted to give agreement upon transformation to laboratory coordinates with the experimental laboratory distributions. The resulting angular functions $T(\Theta)$ are shown in figure 16 as solid curves; $T(\Theta)$ functions for thermal reactions are shown for comparison

Table 1

Translational energies, E reactants, E′ products and reaction exoergicities ΔD_o.

	E	E′	ΔD_o
Br_2	4.9	4.3	45 ± 2
BrCN	4.6	2.9	19 ± 5
$SnCl_4$	5.4	-	25 ± 10
PCl_3	4.9	4.7	19 ± 10 36 ± 10
CCl_4	5.0	8.2	34 ± 10 12 ± 10
CH_3I	4.9	20.1	23 ± 2

Notes: a) Units: $kcal.mole^{-1}$.

b) ΔD_o values are taken from (2) Br_2, (6) BrCN, (7) $SnCl_4$, (8) CH_3I. Upper values for PCl_3, CCl_4 are based on bond energies from V.I.Vedeneyev et al., Bond Energies, Ionisation Potentials and Electron Affinities (Arnold, 1966). Lower value for PCl_3 on A.A.Sandoval et al., J.Phys.Chem. 67, 124 (1963); CCl_4 on JANAF Thermochemical Tables (1965). Alkali halide bond energies from A.G.Gaydon, Dissociation Energies, 3rd edition, (Chapman and Hall, 1968).

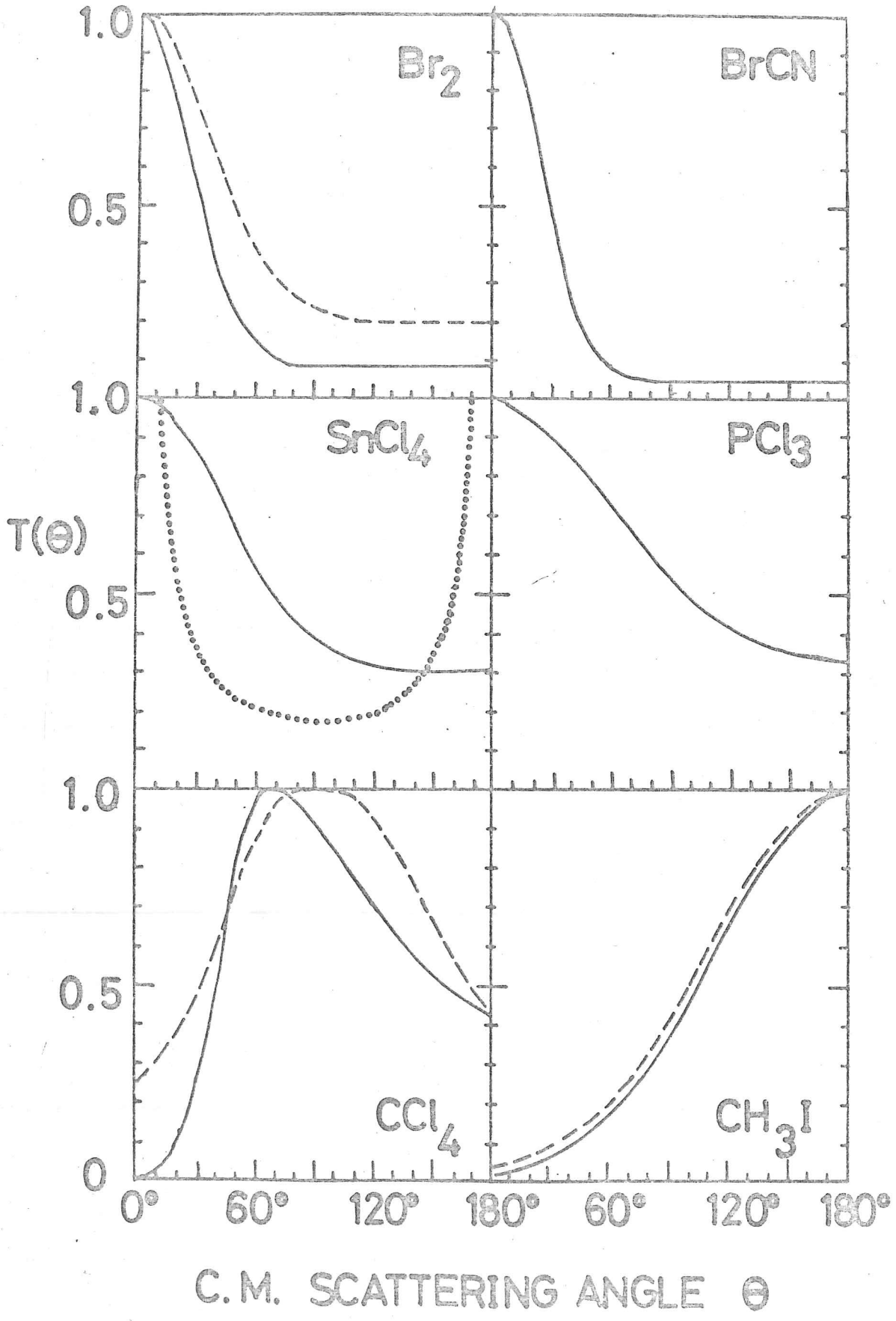

Figure 16: Angular distributions, centre of mass system, T (θ), for reactively scattered KX or KCN by stochastic analysis.

as dashed curves. The results for Br_2 and BrCN confirm the FV distributions exhibiting sharp forward peaking and little intensity in the backward hemisphere. Comparisons with the thermal K + Br_2 (dashed curve) reveal that the forward peak has become appreciably sharper and the intensity in the backward hemisphere has decreased by a factor ~ 2.5 at higher energy.

The stochastic analysis for $SnCl_4$ revealed that the laboratory data of figure 6 is not consistent with a centre of mass distribution with a single recoil velocity peak in the U(u) function and symmetrical about the initial relative velocity vector. This is illustrated by the two trial T(Θ) functions shown in figure 16 for $SnCl_4$. A stripping function shown as a solid curve in figure 16 may be adjusted to give a close fit to the positive angle laboratory data as indicated by the dotted curve in figure 6. However, it is clear that axial symmetry implies much too high an intensity at negative laboratory angles. The second trial T(Θ) function appropriate to a long-lived prolate complex (29) with a very narrow forward peak shown as a dotted curve in figure 16 gives a close fit to the laboratory data at negative laboratory angles, shown as a dashed curve in figure 6. However, in this case axial symmetry implies much too little intensity at positive laboratory angles. Thus the centre of mass reactive scattering distribution must have a more complicated form than the simple postulates of the trial functions. The negative angle laboratory data of figure 6 necessarily requires a rather narrow forward peak as indicated by the prolate complex trial T(Θ) (dotted curve in figure 16). In order to give some insight into the "extra" intensity at positive laboratory angles, the "complex" laboratory intensity (dashed curve in figure 6) is subtracted from

the experimental data. The result, indicated as a dot-dashed curve in figure 6, shows a peak at Ⓗ ~ 45° and a rather limited angular extent. Examination of the Newton diagram of figure 6 reveals that the direction of the centroid vector $\underline{c}$ lies at Ⓗ = 40° suggestively close to the peak of the dot-dashed curve. It suggests that the "extra" positive angle laboratory intensity arises from a second contribution due to KCl constrained close to the centroid vector, i.e. with very low recoil velocity. Now, a "complex" T(Θ) with equal forward and backward centre of mass intensity has been used to explain a narrow forward peak. The existence of a substantial backward peak in the centre of mass corresponding to the forward peak, has in fact contributed laboratory intensity at very wide positive laboratory angles as indicated by the dashed curve in figure 6. It is this intensity which has rendered the dot-dashed curve of figure 6 limited in extent for positive angles. Thus substantial backward intensity is necessary in the centre of mass high velocity contribution for the consistency of the analysis. The stochastic analysis indicates that the centre of mass recoil velocity distribution is strongly dependent on scattering angle which indeed invalidates the FV transformation (figure 12) for this reaction.

The result of the stochastic analysis for PCl_3 confirms the FV distribution, exhibiting a much flatter T(Θ) function than Br_2, BrCN with a broad peak in the forward direction and substantial intensity in the backward hemisphere. As before only thermal Rb + PCl_3 data (7) are available for comparison and are closely similar in shape. This is not shown for comparison since a change of alkali atom spoils the basis for observation of kinetic energy effects.

The T(Θ) function for CCl_4 confirms the FV distribution with remarkable fidelity, showing a peak sideways at $\Theta = 67^{\circ}$. Comparison with the T(Θ) function (27) for thermal K + CCl_4 reveals that the sideways peak lay at a wider angle ($\Theta = 90^{\circ}$) and has moved forward with increasing energy. Finally the result for CH_3I also confirms the FV analysis. Comparison with the T(Θ) function (27) for thermal K + CH_3I shows precise agreement to within experimental error. Thus in contrast to the other reactions, increase in initial kinetic energy for K + CH_3I does not alter the shape of the centre of mass differential cross section greatly.

The total reaction cross sections Q calculated by methods A, B and C of (2), and total scattering cross sections Q_t, estimated from the Landau-Lifshitz approximation (30) are given in table 2. Total reaction cross sections for the corresponding thermal K atom reactions are also given for comparison. In all cases the supersonic K atom cross sections are lower (by as much as a factor of two) than those of thermal K atoms. Despite the very approximate nature of the reaction cross section estimates, this discrepancy appears to be significant. No direct estimate of the K + $SnCl_4$ cross section was made but it is clear from the rapid fall in the centre of mass elastic scattering distribution, and the high intensity of reactive scattering in laboratory coordinates that the cross section must be large, say ≥ 100 Å^2.

Discussion

The elastic and reactive scattering of a supersonic K atom beam with a narrow Laval velocity distribution results in improved resolution over thermal K atom beam measurements. Thus rainbow

Table 2

Total Cross Sections

	Br_2	BrCN	$SnCl_4$	PCl_3	CCl_4	CH_3I
Q_t	700	765	770	890	855	1070
Q_t^{eff}	310	335	335	380	370	445
Q(A)	95	-	-	-	-	-
Q(B)	115	50	-	25	20	10
Q(C)	130	65	-	35	35	25
Q_{av}	115	60	≥ 100	30	25	20
Q_{th}	230	170	-	-	60	35

Notes: a) Q_t total scattering cross section, Q_t^{eff} total scattering cross section with resolution correction, Q(A) Q(B) Q(C) estimates of total reaction cross sections (Qau average), Q_{th} total reaction cross sections at thermal energies.

b) Units A^{o2}

structure is observed in the small angle elastic scattering without velocity selection. More importantly the elastic scattering falls so rapidly with increasing angle that reactive scattering greatly exceeds elastic scattering for $\textcircled{H} \gtrsim 15^{o}$ (except for the CH_3I data) and the subtraction of Pt/W intensity from W intensity with its associated uncertainty is insignificant. Thus the reactive scattering is particularly well resolved in these experiments. This is especially true in the $K + CCl_4$ reaction where the bimodal KCl distribution is immediately apparent and confirms conclusions from thermal measurements (7) which required magnetic deflection (22) for their resolution.

The reactive scattering distributions with reactant kinetic energies $E \sim 5$ kcal.mole^{-1}, show broadly the same features as the distributions at thermal energies ($E \lesssim 1.5$ kcal.mole^{-1}). However, the total reaction cross sections have decreased at the higher energies in all cases (roughly by a factor of two). Since the entrance valley in all these reactions is dominated by an electron jump (see equation (1)), a decrease in the reaction cross section can be anticipated from two causes:

(a) When the electronic matrix H_{12} between the covalent and ionic states (31) at the curve crossing radius R_c greatly exceeds the initial kinetic energy E the reaction cross section is governed (15, 16) by orbiting on the lowered adiabatic potential surface at $R \gtrsim Rc$. As the kinetic energy increases, the orbiting impact parameter b_{orb} decreases, decreasing the reaction cross section (15).

$$Q \gtrsim \pi b_{orb}^2. \qquad (2)$$

(b) If however the electronic matrix element H_{12} is comparable with the kinetic energy E, trajectories may pass through the crossing

radius R_c without an electron jump occurring, i.e. a diabatic transition. The probability of diabatic transition increases with kinetic energy (31) resulting in a decreasing reaction cross section.

Clearly effect (a) goes over into effect (b) for a sufficiently wide range of kinetic energies at a given crossing interaction H_{12}. However, after an electron jump has occurred the Coulomb interactions giving rise to products (equation 1) will be too strong for the reactant kinetic energy to have any effect on the probability of product formation in this part of the reaction dynamics, provided $E \ll \Delta D_o$. The elastic scattering measurements of Harris and Wilson (17) confirm that the situation (a) applies for $K + SnCl_4$ in the energy range $E = 1 - 5$ kcal mole^{-1}. Thus, the decrease in reaction cross section for the reactions with large cross sections Br_2, $SnCl_4$ and perhaps BrCN, can be ascribed to the decrease in orbiting impact parameter. However, the measurement of the energy dependence of the reaction cross section for $K + CH_3I$ by Gersch and Bernstein (14) reveals an energy dependence more complicated than situation (a) would indicate. Indeed the decrease in reaction cross section for $E > 4$ kcal mole^{-1} correlates with the opening up of $K + CH_3I$ inelastic scattering channels,* which is suggestive of effect (b).

A more sensitive probe of the reaction dynamics is provided by the energy dependence of the differential reaction cross section. In the $K + Br_2$, BrCN, CCl_4 reactions where comparison with thermal energy differential cross sections is possible, there is an increase

---

* The cross section for inelastic scattering may be judged qualitatively by the discrepancy between the directly measured reaction cross section and estimates from optical model analysis of the K atom scattering, as shown in the figure of (14).

in forward scattering for the higher initial kinetic energy. For $K + Br_2$, BrCN stripping reactions, this consists of a sharpening of the forward peak to a width of $\Theta \simeq 30^\circ$ at half height and a diminution by a factor ~ 3 in the intensity scattered in the backward hemisphere. It has been suggested by Polanyi (32) that these 'stripping' reactions should approach the limit of 'spectator stripping' (5, 32) at high energies. Certainly the increased peaking in the forward direction is compatible with this point of view. However, a more discriminating test may be applied by examining the product kinetic energy E' which, for spectator stripping (32) is given by

$$E' = E \cos^2 \beta + W \sin^2 \beta \qquad (3a)$$

$$\cos^2 \beta = M_K M_Y / M_{KX} M_{XY} \qquad (3b)$$

where XY denotes the halogen molecule and W its internal energy. Equation (3) predicts E' = 1.3 and 2.4 $kcal.mole^{-1}$ for $K + Br_2$, BrCN which are to be compared with experimental estimates E' = 4.3 and 2.9 $kcal.mole^{-1}$. Even allowing for the approximate nature of the FV method (11), which because of the effect of Jacobian factors tends to underestimate the kinetic energy but is usually qualitatively accurate for forward scattering, the recoil energy of $K + Br_2$ is not compatible with spectator stripping. However, the recoil energy for K + BrCN is indeed consistent with spectator stripping, or a relatively close approach to it.

For $K + CCl_4$ the increase in forward scattering with initial kinetic energy is relatively modest; the sideways peak moves forward by $\sim 20^\circ$. In the $K + CH_3I$ reaction indeed there is no appreciable change in the differential cross section shape with kinetic energy, to within experimental error. However, in collisions

at small impact parameters with repulsive interactions the products cannot pass through one another and so (32) they must rebound into the backward hemisphere even at high energies. Hence for $K + CH_3I$ with the smallest total reaction cross section reactive collisions are observed only from small impact parameters which are insensitive to initial kinetic energy. Again for $K + CCl_4$ with a rather small total reaction cross section, sensitivity to initial kinetic energy would be anticipated only for the largest impact parameters which can react and this appears as a forward shift in the position of the sideways peak.

It is interesting to note, in these experiments, an increased tendency to forward peaking for reaction at larger impact parameters with increased kinetic energy and a simultaneous decrease in total reaction cross section. Now it is well known that increasing reaction cross section for these reactions (17) fosters forward scattering due to the enhancement of large impact parameters contributing to the reaction. Thus to the extent that the decrease in reactive total cross section with increased kinetic energy arises from a decrease in the maximum impact parameter for reaction, we would expect this to create a tendency towards backward scattering. The fact that we observe a tendency towards forward scattering with increasing initial kinetic energy despite the decreased reactive total cross section, indicates that the energy effect for large impact parameter collision dynamics may be greater than is superficially apparent. It may be that the increasing forward scattering arises from collisions of decreasing impact parameter with increasing initial kinetic energy. The maximum initial orbital angular momentum for reaction is however increased slightly, by a factor of ~ 1.4 for

$K + Br_2$ for instance.

For $K + SnCl_4$, the stochastic analysis suggests that there are two contributions to the centre of mass reactive scattering: (a) a high velocity component consisting of a sharp forward peak and comparable peaking in the backward hemisphere, perhaps a complex distribution with equal forward and backward intensity, and (b) a low velocity component with intensity constrained close to the centre of mass. The reaction exoergicity as indicated in table 1, $\Delta D_o = 25 \pm 10$ kcal.mole^{-1}, for the reaction

$$K + SnCl_4 \longrightarrow KCl + SnCl_3 \quad (4)$$

is quite high, so that the product recoil kinetic energy should be at least comparable with the initial kinetic energy. Thus one may tentatively identify the 'high velocity' component of the scattering with this reaction path. However, an alternative reaction path may be

$$K + SnCl_4 \longrightarrow KCl + SnCl_2 + Cl \quad (5)$$

in view of the well known stability of $SnCl_2$. Using the heats of formation of $SnCl_2$, $SnCl_4$ at 298K (34), gives a reaction exoergicity of $\Delta D_o \sim -4 \pm 10$ kcal.mole^{-1}. Thus the reaction path is slightly endoergic; much of the initial kinetic energy is required for the products to follow this exit valley of the potential surface, leaving little energy for disposal into product kinetic energy. It is tempting to attribute the 'low velocity' component of the centre of mass intensity to this reaction path. However, such an explanation of the reaction dynamics requires that all of the reaction energy be available to the $SnCl_3$ fragment in order to permit its dissociation. This, taken with the highly attractive $K^+ - SnCl_4^-$ potential and endoergic exit channel, suggests that the dynamics leading to the

reaction path of equation (5) would involve a long lived (29) collision complex. This is sufficient to preclude the reaction path of equation (5) since the reaction complex would then dissociate overwhelmingly by the exoergic reaction path of equation (4). However, these considerations do suggest a reaction path which may more adequately explain the low velocity component

$$K + SnCl_4 \longrightarrow K^+SnCl_3^- + Cl \qquad (6)$$

There are no means of estimating the exoergicity of this path, but the $SnCl_3^-$ ion is known (35) to be stable in solution, so the exoergicity may be comparable to that of equation (4). The high mass of $KSnCl_3$ would necessarily confine it close to the centre of mass compared with the KCl from equation (4) when comparable energy appears in product translation for both reaction paths. The kinematic analysis suggests that a long-lived complex distribution for the high velocity component would be compatible with the data. Hence it is plausible that the dynamics of the $K + SnCl_4$ reaction consist of a long-lived complex $K^+SnCl_4^-$ which can dissociate by equations (4) and (6). In view of the highly attractive potential of $K^+SnCl_4^-$ and its large number of degrees of freedom the mechanism is perhaps not surprising.* The geometry of a $K^+SnCl_4^-$ complex presents some interesting features. While calculation with 'reasonable' bond lengths indicates a prolate symmetric top, the ratio of the moments of inertia ($I_\perp/I_\parallel \gtrsim 2$ for equation (4), $\lesssim 2$ for equation (6)), is much smaller than previous (29) reactions. Since $K^+SnCl_4^-$ must dissociate through a range of configurations, some may correspond to a spherical top or even an oblate symmetric top,

---

* Reference (17) mentions measurements by J. S. Riley which also indicate a long-lived complex for $M + SnCl_4$.

thus contributing intensity at wide angles $\theta \sim 90^{\circ}$, and altering the form of the product velocity distribution (36). Needless to say, kinematic analysis of merely a simple angular distribution for this seemingly complicated reaction permits only an outline of the possible reaction dynamics. It must fall to velocity analysis measurements to provide a more discriminating analysis.

References

(1) D. R. Herschbach, Adv.Chem.Phys. 10, 319 (1966).

(2) J. H. Birely, R. R. Herm, K. R. Wilson and D. R. Herschbach, J.Chem.Phys. 47, 993 (1967).

(3) R. Grice and P. B. Empedocles, J.Chem.Phys.48, 5352 (1968).

(4) G. H. Kwei and D. R. Herschbach, J.Chem.Phys. 51, 1742 (1969).

(5) R. E. Minturn, S. Datz and R. L. Becker, J.Chem.Phys.44, 1149 (1966).

(6) R. Grice, M. R. Cosandey and D. R. Herschbach, Ber.Bunsenges. phys.Chem. 72, 975 (1968).

(7) K. R. Wilson and D. R. Herschbach, J.Chem.Phys. 49, 2676 (1968).

(8) G. H. Kwei, J. A. Norris and D. R. Herschbach, J.Chem.Phys. 52, 1317 (1970).

(9) K. T. Gillen, A. M. Rulis and R. B. Bernstein, J.Chem.Phys. 54, 2831 (1971)

(10) R. B. Bernstein, M. E. Gersch and A. M. Rulis, Electronic and Atomic Collisions, edited by L. M. Branscomb et al., VII ICPEAC (North Holland), 34 (1971).

(11) E. A. Entemann and D. R. Herschbach, Disc.Farad.Soc. 44, 289 (1967).

(12) R. Grice, Ch. Ottinger and D. R. Herschbach (to be published).

(13) Ch. Ottinger, P. M. Strudler and D. R. Herschbach (to be published).

(14) M. E. Gersch and R. B. Bernstein, J.Chem.Phys. 55, 4661 (1971).
M. E. Gersch and R. B. Bernstein, J.Chem.Phys. 56, 6131 (1972).

(15) R. W. Anderson, Ph.D. Thesis (Harvard University, 1968).

(16) R. Grice, Ph.D. Thesis (Harvard University, 1967).

(17) R. M. Harris and J. F. Wilson, J.Chem.Phys. 54, 2088 (1971).

(18) R. Grice and D. R. Hardin, Mol.Phys. 21, 805 (1971).

(19) G. M. Kendall, P. B. Foreman and R. Grice, Electronic and Atomic Collisions, edited by L. M. Branscomb et al., VII ICPEAC (North Holland), 23 (1971).

(20) P. B. Foreman, G. M. Kendall and R. Grice, Mol.Phys. 23, 117 (1972).

(21) P. B. Foreman, G. M. Kendall and R. Grice, Mol.Phys. 23, 127 (1972).

(22) Chapter 2.

(23) R. J. Gordon, R. R. Herm and D. R. Herschbach, J.Chem.Phys. 49, 2684 (1968).

(24) J. R. Airey, F. E. Greene, G. P. Reck and J. Ross, J.Chem. Phys. 46, 3295 (1967).

(25) E. F. Greene, L. F. Hoffmann, M. W. Lee, J. Ross and C. E. Young, J.Chem.Phys. 50, 3450 (1969).

(26) K. T. Gillen and R. B. Bernstein, Chem.Phys.Letters 5, 275 (1970).

(27) E. A. Entemann, Ph.D. Thesis (Harvard University, 1967).

(28) T. T. Warnock, R. B. Bernstein and A. E. Grosser, J.Chem.Phys. 46 1685 (1967).

(29) W. B. Miller, S. A. Safron and D. R. Herschbach, Disc. Farad.Soc. 44, 108 (1967).

(30) H. Pauly and J. P. Toennies, Adv.atom.molec.Phys. 1, 195 (1965).

(31) L. D. Landau and E. M. Lifshitz, Quantum Mechanics, 2nd edition (Pergamon Press, 1965).

(32) J. C. Polanyi, Disc.Farad.Soc. 44, 293 (1967).

(33) D. R. Herschbach, Applied Optics (Suppl. 2), 128 (1965).

(34) F. D. Rossini et al., Selected Values of Chemical Thermodynamic Properties, National Bureau of Standards (Washington, D.C., 1952).

(35) F. A. Cotton and G. Wilkinson, Advanced Inorganic Chemistry, 2nd edition (Wiley, Interscience, 1966).

(36) S. A. Safron, N. D. Weinstein, D. R. Herschbach and J. C. Tully, Chem.Phys.Lett. 12 564 (1972).

CHAPTER II

REACTIVE SCATTERING OF ALKALI DIMERS: DETERMINATION OF TWO PRODUCT DISTRIBUTIONS FOR $K_2 + Br_2$, BrCN, IBr and $SnCl_4$

Introduction

The reactive scattering of potassium dimers with a variety of halogen-containing molecules has recently been studied (1-3) and the angular distributions of alkali halide product measured. The reactions $K_2 + Br_2$, BrCN and IBr have large reactive cross sections (140, 85, 210 $\overset{o}{A}^2$, respectively). The centre of mass differential cross sections for the halide (or cyanide) product peak in the forward direction and show pronounced asymmetry. If the reaction of, say, $K_2 + Br_2$ produced two KBr molecules, conservation of linear momentum would require the centre of mass differential cross section to be symmetrical about $\Theta = 90^o$. Thus it appears that the reaction mechanism is of the form

$$K_2 + XY \longrightarrow KX + K + Y . \quad (1)$$

However examination of the alkali halide distributions alone does not rule out the possibility of the products KX, KY being formed with one halide vibrationally excited near to its dissociation limit, as a methanated Pt/W filament, whilst normally being insensitive to alkali halides, does partially detect highly vibrationally excited halides (4). The mechanism postulated (1-3) to explain the dynamics of the reaction $K_2 + XY$ is that the entrance valley of the potential energy surface will be governed by an electron jump mechanism as is the surface for the corresponding K + XY reaction (5-7). The electron jump occurs at the crossing distance r_c between the covalent $K_2 + XY$ surface and the ionic $K_2^+ + XY^-$ surface. This crossing radius r_c is given by

$$r_c = e^2/[I_v(K_2) - E_v(XY)] \qquad (2)$$

where $E_v(XY)$ is the vertical electron affinity of XY and $I_v(K_2)$ is the ionisation potential of K_2. The first stage of the mechanism is thus

$$K_2 + XY \longrightarrow K_2^+ + (XY)^- \quad . \qquad (3)$$

It is then suggested that the $(XY)^-$ ion dissociates more rapidly than does the K_2^+ ion, forming a $K_2^+X^-$ intermediate which then dissociates to KX and K:

$$K_2 + XY \longrightarrow K_2^+ + (XY)^- \longrightarrow K_2^+ \ldots . X^- + Y \longrightarrow KX + K + Y. \qquad (4)$$

The centre of mass distributions of non-reactive scattering (i.e. the signal on the Pt/W filament transformed to the centre of mass frame by the fixed velocity (FV) approximation using the elastic K_2 velocity) for $K_2 + Br_2$, IBr are very similar in shape, having considerable intensity at wide angles; that for K_2 + BrCN falling more rapidly. These differences are not readily explained in terms of K_2 elastic scattering and are not found in the corresponding K atom scattering (5-8). However, the reactive K atom product of Eq.4 would be detected by the Pt/W filament and wrongly included in the K_2 elastic scattering distribution. Chemiluminescence of electronically excited K atoms has been observed (9) from the reaction K_2 + Cl_2, which would suggest a reaction path of the form of Eq.4.

For the reaction $K_2 + SnCl_4$ (2, 3) the reactive cross section is large ($\sim 160 \mathring{A}^2$) and the centre of mass reactive scattering distribution is peaked in a forward direction. The non-reactive scattering falls off very rapidly at wide angles (much more so than K_2 + BrCN). It is not possible from examination of the alkali halide distribution alone to deduce what the products of the reaction are; although the large cross section and the forward peaking

suggest that an electron jump dominates the entrance valley of the potential-energy surface.

Method and Results

For all the reactions studied, the dominant feature of the entrance valley of the potential energy surface is thought to be an electron jump occurring at a separation r_c, large enough to remove scattering from the repulsive core. Studies of the comparable reactions with alkali atoms (5, 7, 10) at thermal energies, similarly governed by an electron jump mechanism, have shown the dynamics of the scattering to be very insensitive to the identity of the alkali atom. This is most marked (11) for the elastic scattering distributions in which the wide angle scattering comes mainly from collisions at wide impact parameters ($b \geq r_c$) which involve "orbiting" outside a centrifugal barrier, rather than from collisions at smaller impact parameters which fail to give reaction. The exponential fall-off in the wide angle scattering suggests that orbiting is involved. As the ionisation potential of K_2 is similar to those of the alkali atoms and the dimer reactions are also dominated by an electron jump mechanism, it would be reasonable to anticipate that the K_2 dimer elastic scattering from a given halogen molecule should be similar to the K atom elastic scattering from the same halogen molecule, measured under comparable conditions.

The reactive scattering apparatus (2, 3, 12) used in the potassium dimer studies, gives a mixed beam of potassium atoms and dimers, both of which have almost exactly the same velocity distribution. In the dimer experiments an inhomogeneous magnetic field deflected out the atom component of the beam. If the magnet

energizing current is switched off, then atoms are undeflected and a mixed beam of atoms and dimers enters the scattering chamber. At a given scattering angle, measurements are made with the magnet on and off, the scattering due to the atoms being obtained by subtraction. This technique is described in the previous chapter where it was used to obtain reactive and elastic scattering of atoms with a variety of halogen-containing molecules. This chapter is concerned with comparisons of the elastic scattering of atoms and dimers.

Figure 1 compares the relative intensities of K_2 + Br_2, BrCN (open symbols) and supersonic K + Br_2, BrCN (closed symbols) as measured on a methanated Pt/W filament plotted logarithmically against laboratory scattering angle (H). Figure 2 is a similar plot for K_2 + IBr, $SnCl_4$ (open symbols) compared with supersonic K + IBr, $SnCl_4$ (closed symbols). Even in the laboratory frame, it is apparent that the atom data falls more rapidly at wide angles than does the dimer data, except in the case of $SnCl_4$ where atom and dimer data are virtually superimposable.

The raw data is transformed to centre of mass coordinates using the FV approximation with the velocity appropriate to elastic scattering. The atom elastic scattering is then normalised to the dimer elastic scattering at small angles, where the distributions are negligibly perturbed by reactive scattering; the two branches of the centre of mass elastic scattering that arise from positive and negative lab. angles are treated separately. Figure 3 shows the relative intensity of elastic scattering (weighted by sin Θ to remove the solid angle factor introduced by the symmetry of scattering about the initial relative velocity vector) plotted logarithmically against

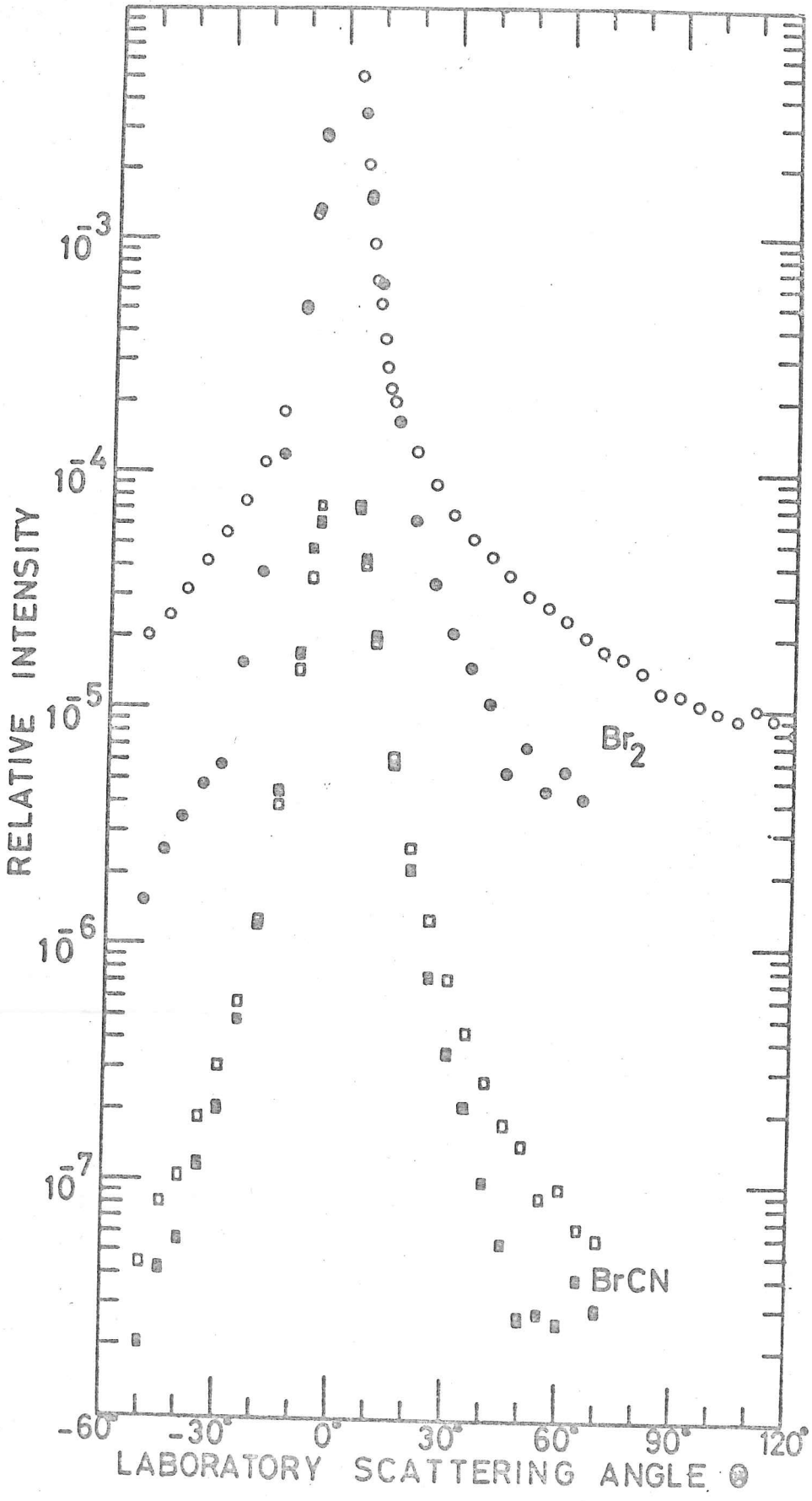

Figure 1: Lab. angular distributions measured on Pt/W filament for scattering of K_2 + Br_2, BrCN (open symbols) and supersonic K + Br_2, BrCN (closed symbols). The curves for BrCN are shifted down by two decades for clarity.

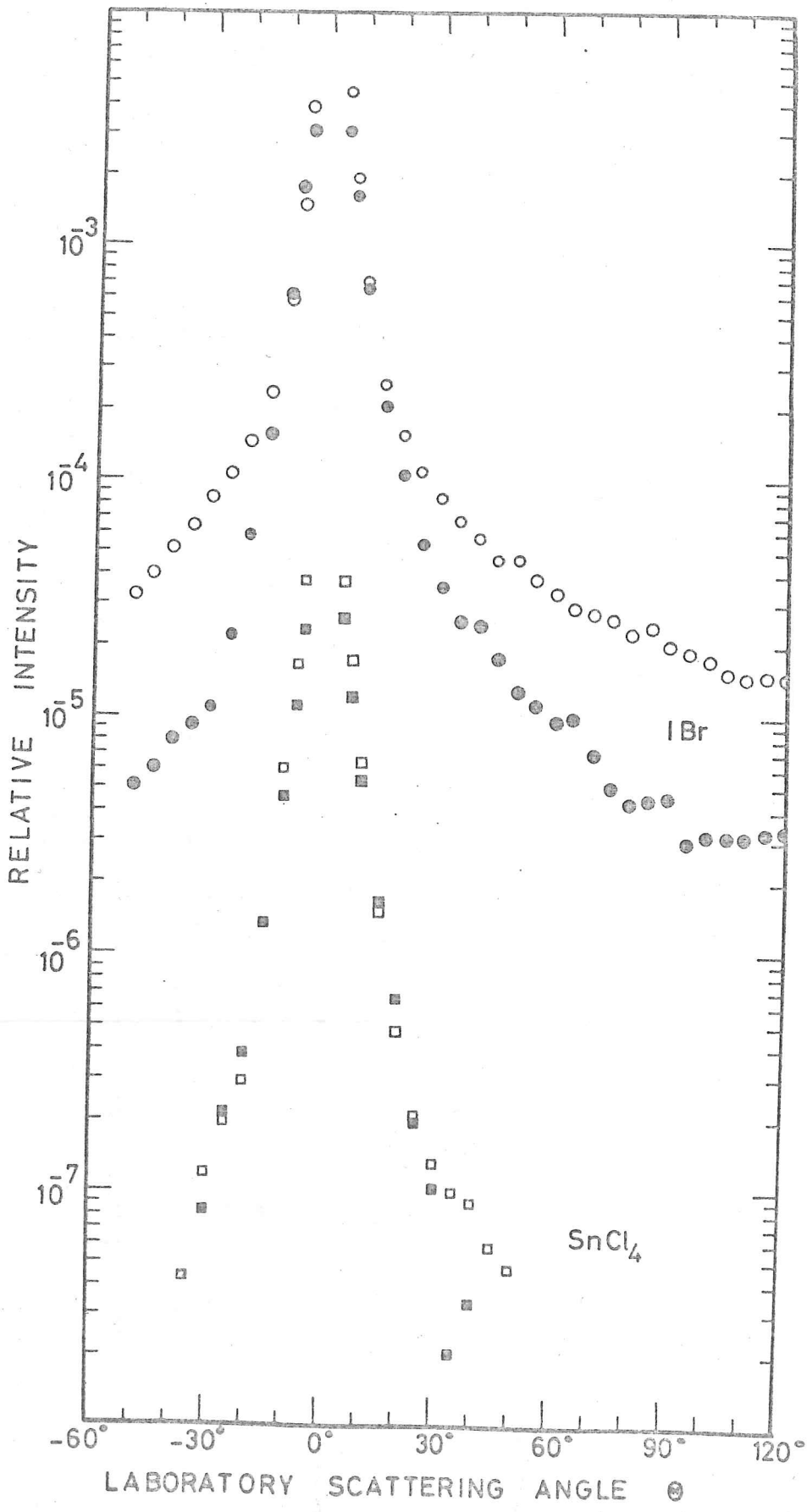

Figure 2: Lab. angular distributions measured on Pt/W filament for scattering of K_2 + IBr, $SnCl_4$ (open symbols) and supersonic K + IBr, $SnCl_4$ (closed symbols). The curves for $SnCl_4$ are shifted down by two decades for clarity.

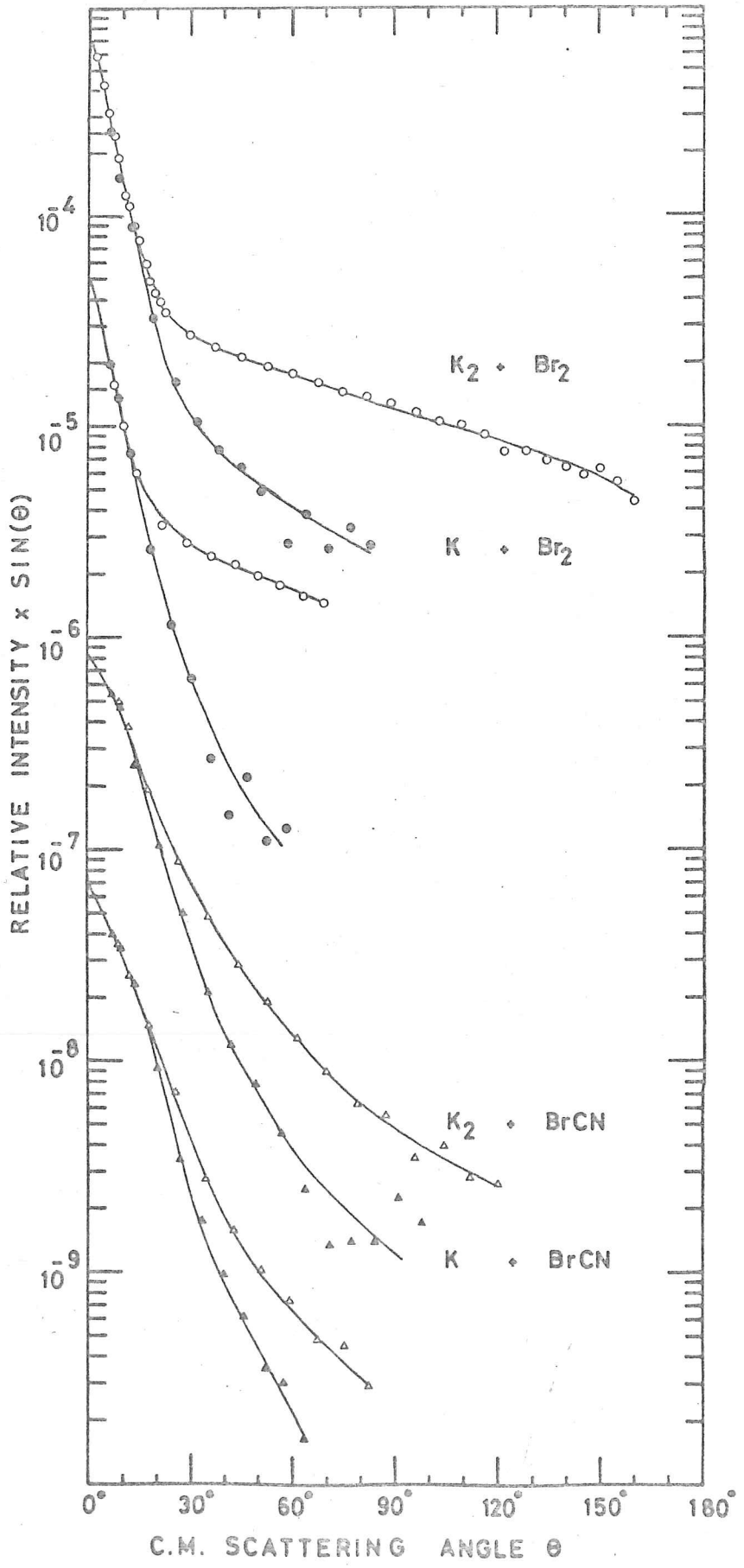

Figure 3: Angular distributions in centre of mass coordinates by transformation of Pt/W data for K_2 + Br_2 BrCN (open symbols) and supersonic K + Br_2, BrCN (closed symbols). The negative branches are shifted down by one decade from the positive branches for clarity and the positive branch of BrCN is shifted down three decades from the positive branch of Br_2.

centre of mass scattering angle Θ for the positive and negative branches of K_2 + Br_2, BrCN elastic scattering (open symbols) compared with the elastic scattering of K + Br_2, BrCN (closed symbols). Figure 4 shows the comparison for K_2 + IBr, $SnCl_4$ (open symbols) and K + IBr, $SnCl_4$ (closed symbols).

For Br_2, BrCN and IBr the atom elastic scattering falls more rapidly than does the dimer elastic scattering. As stated above, it is expected that K_2 will behave in many ways as an alkali atom and in particular that the elastic scattering of K_2 with a given halogen should be superimposable on that for K with the same halogen. That this is not so, would seem to indicate that the signal measured on the Pt/W filament for dimers is not solely due to the elastic scattering of K_2. The only other relevant substances to which a methanated Pt/W filament is sensitive are K atoms or highly vibrationally excited halides KX. The difference between the atom and dimer "elastic" scattering is then transformed back to the laboratory system using the Jacobian factors appropriate to the dimer scattering, as the difference has been wrongly included in the dimer elastic scattering.

For $SnCl_4$ the atom and dimer elastic scattering are identical, supporting the view that K_2 behaves as an alkali atom and that in the reaction of K_2 + $SnCl_4$ there is no K atom or highly vibrationally excited KCl produced.

Figures 5, 6 and 7 show the lab. distributions of KBr (or KCN) and the transformed differences in elastic scattering (dashed curves) for K_2 + Br_2, BrCN, IBr respectively. The vector diagrams for the most probable velocities of the beams are also shown: the circles represent accessible regions for various product recoil energies, the

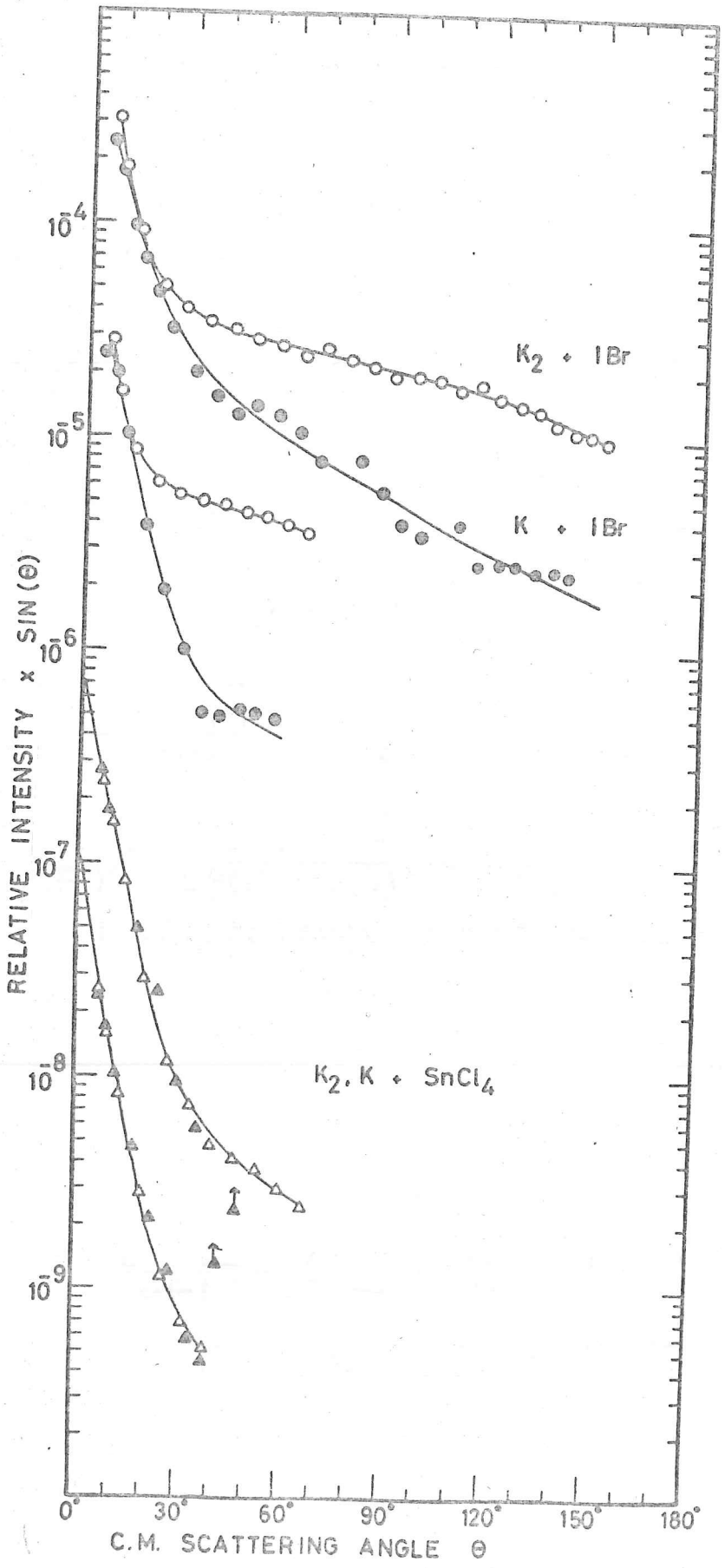

Figure 4: Angular distributions in centre of mass coordinates by transformation of Pt/W data for K_2 + IBr, $SnCl_4$ (open symbols) and supersonic K + IBr, $SnCl_4$ (closed symbols). The negative branches are shifted down by one decade from the positive branches for clarity and the positive branch of $SnCl_4$ is shifted down three decades from the positive branch of IBr.

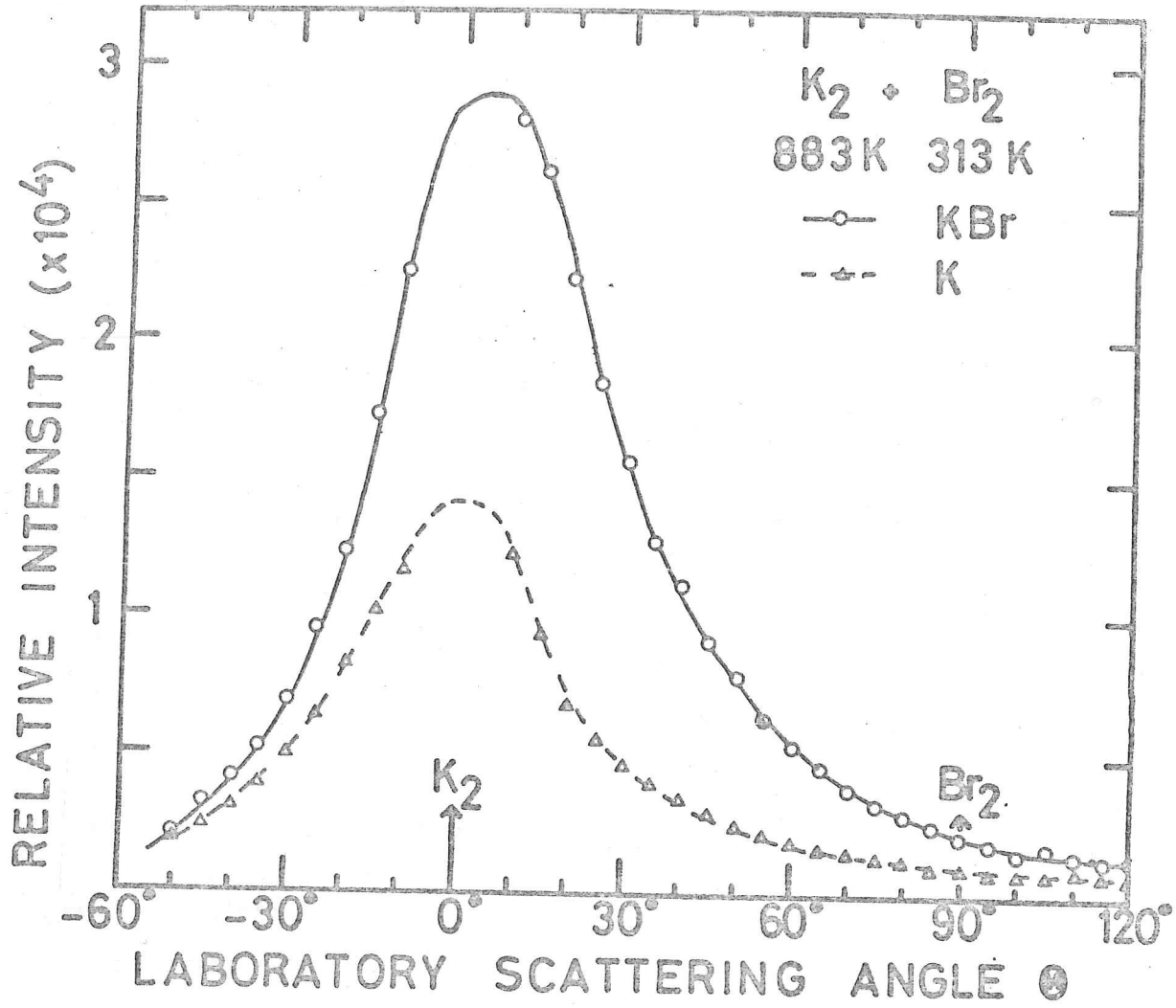

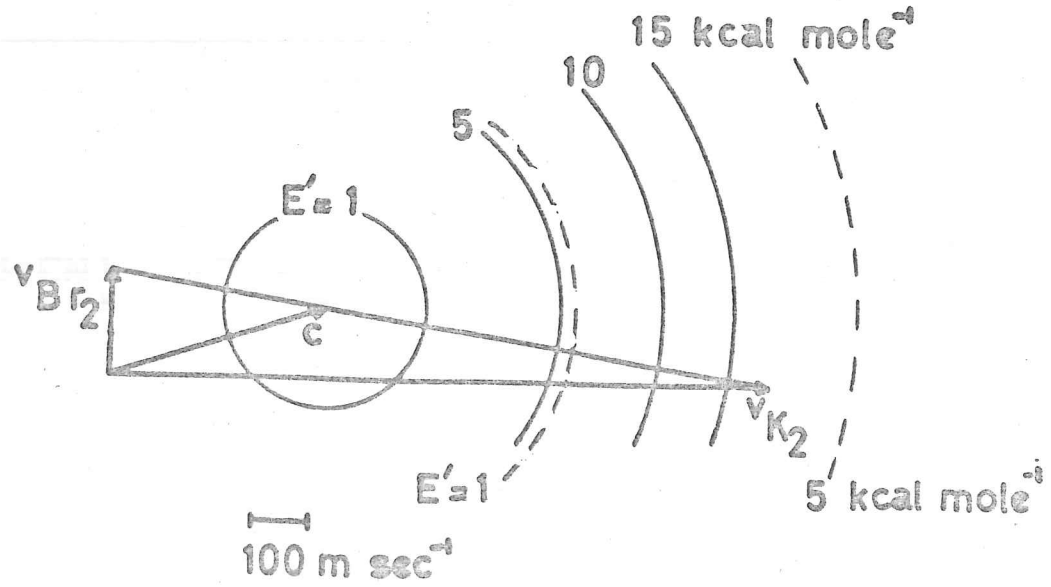

Figure 5: Lab. angular distributions of K (triangles and dashed curve) and KBr (circles and solid curve) for K_2 + Br_2. The Newton diagram is also shown, dashed circles denote K recoil velocities, solid circles KBr recoil velocities.

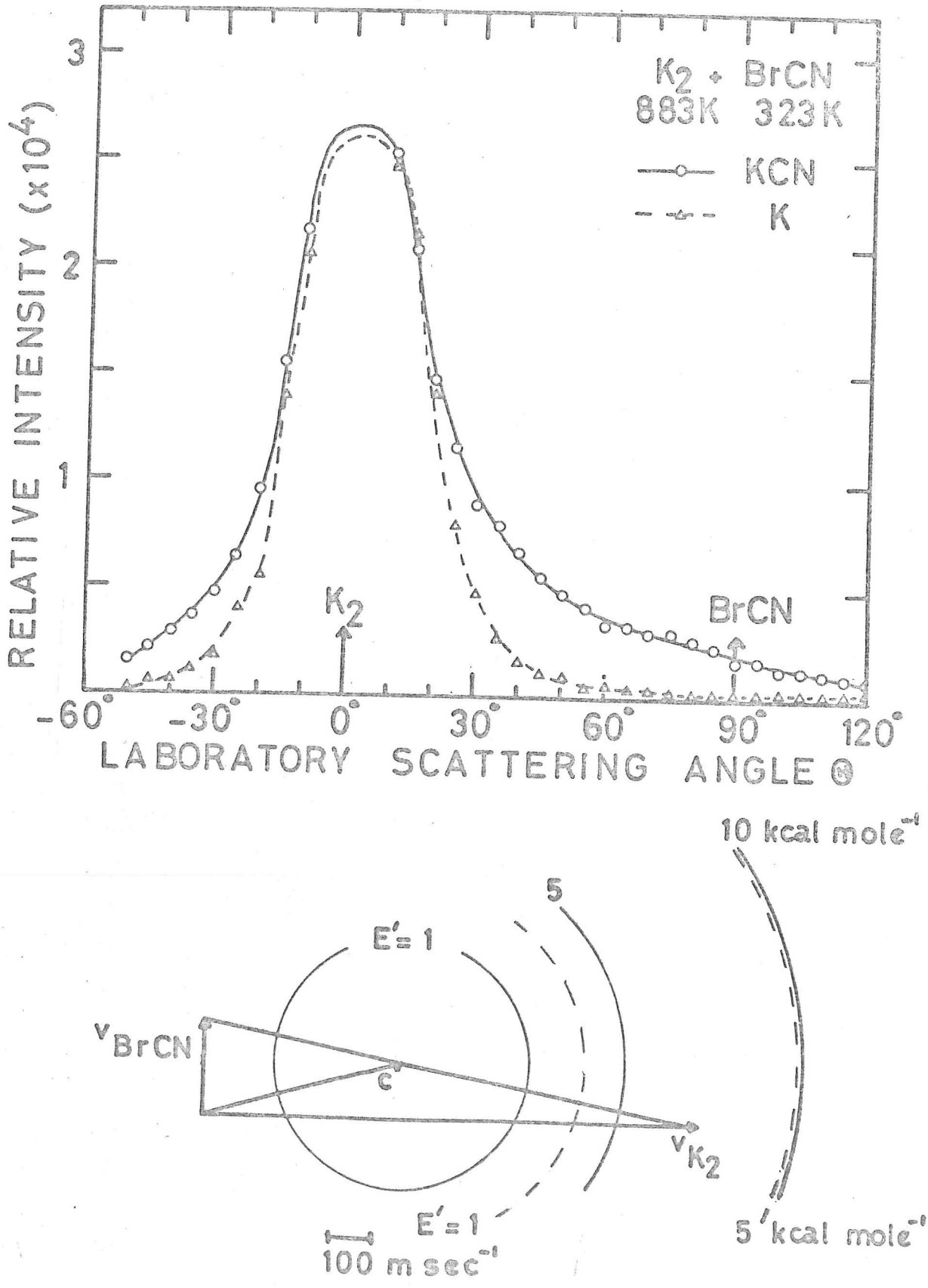

Figure 6: Lab. angular distributions of K (triangles and dashed curve) and KCN (circles and solid curve) for K_2 + BrCN. The Newton diagram is also shown, dashed circles denote K recoil velocities, solid circles KCN recoil velocities.

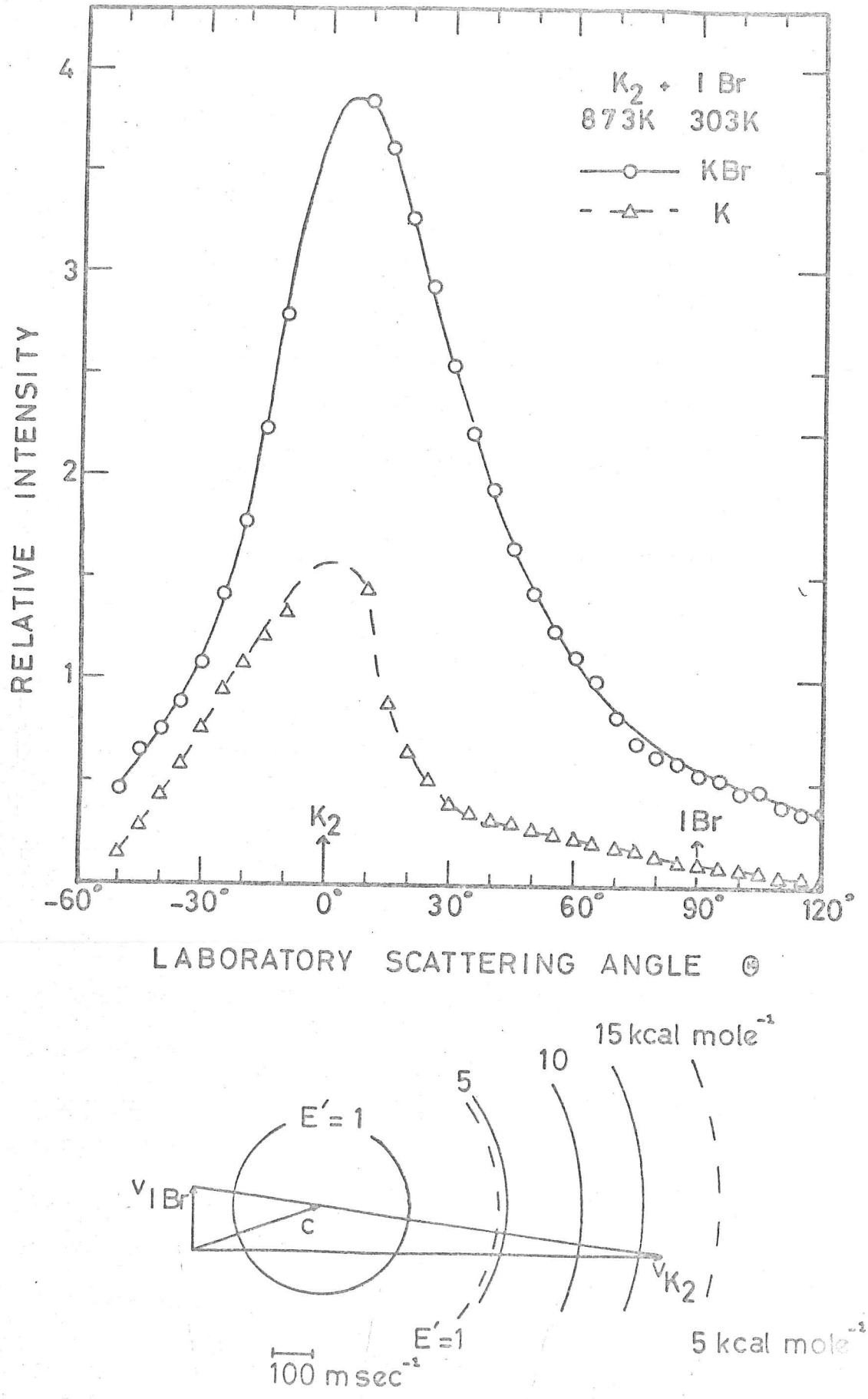

Figure 7: Lab. angular distributions of K (triangles and dashed curve) and KBr (circles and solid curve) for K_2 + IBr. The Newton diagram is also shown, dashed circles denote K recoil velocities, solid circles KBr recoil velocities.

solid curves for KX product and the dashed curves for K product. The K atom distributions all show a peak at small angles near to the K_2 beam; those for Br_2 and IBr being lower in intensity and shifted more to negative angles than the KBr distributions. In all cases the intensity of K atoms is, at wide angles, less than that of KX; this being most pronounced in the case of BrCN.

These laboratory distributions are then transformed to centre of mass coordinates using the FV approximation (13). Figures 8, 9 and 10 show the centre of mass differential cross sections of halide (or cyanide) and K atom for Br_2, BrCN and IBr respectively. The recoil velocity of the product is adjusted until the redundant branches of the centre of mass distribution are brought into agreement. For the K atom distribution from K_2 + IBr, no satisfactory matching was obtained and Figure 10 shows the centre of mass differential cross section obtained using the same velocity as was used for the K atom distribution from K_2 + Br_2.

In all cases, the K atom distribution peaks in a forward direction with about the same intensity as the KX distribution. The forward peaking rules out highly vibrationally excited KX as causing the difference in the elastic scattering of dimers and atoms, since conservation of linear momentum requires this product to recoil into the backward hemisphere. The atom distributions fall more rapidly at wide angles than do the halide (or cyanide) distributions; that for K_2 + Br_2 falling to about half that of the halide, whereas the K atom distribution from K_2 + BrCN is only 10% of the cyanide at wide angles ($\theta > 90^\circ$), IBr being intermediate between these two.

As a check on the FV transformation, a procedure due to Entemann (13) was used. This method takes an assumed centre of mass

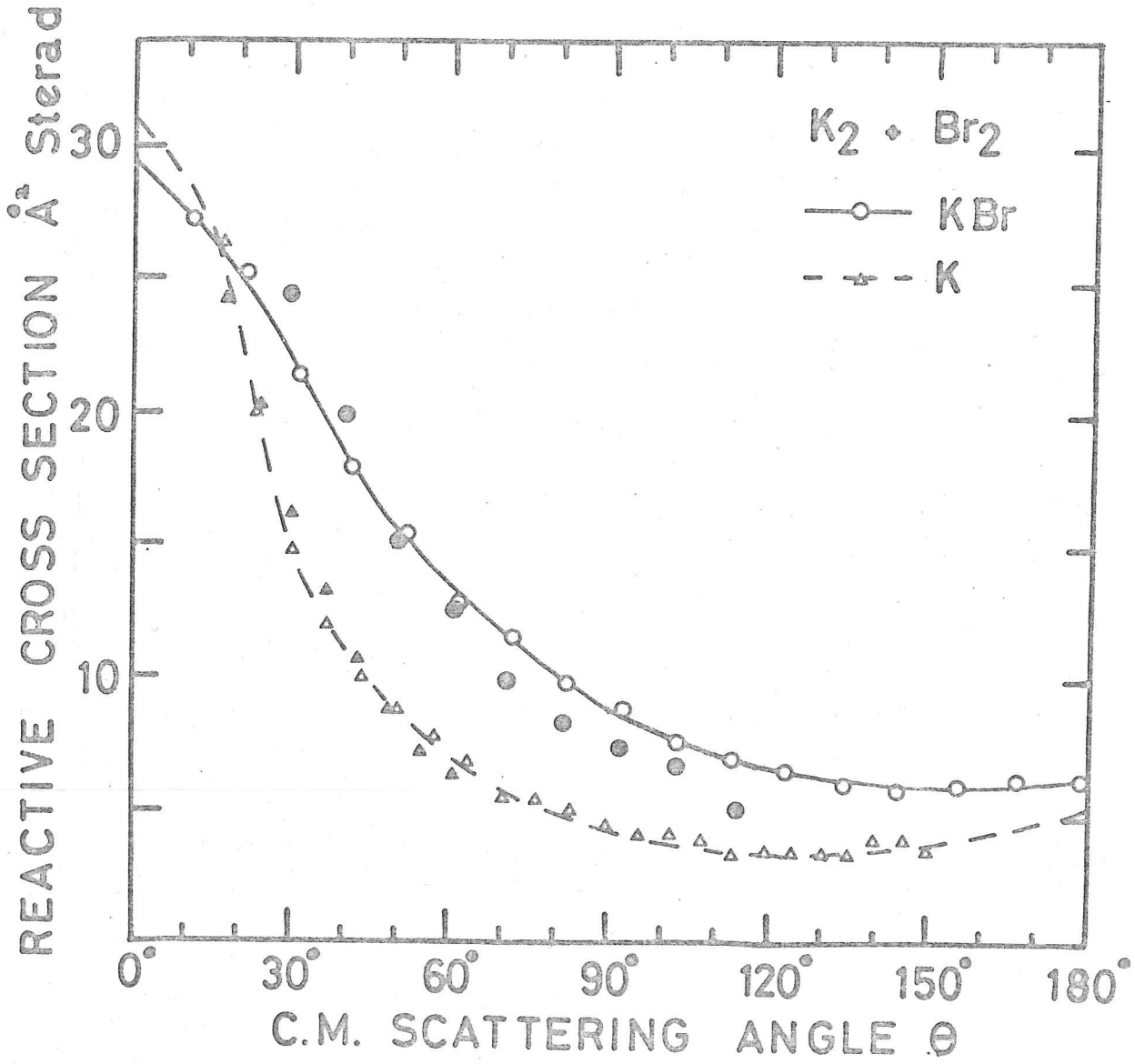

Figure 8: Differential cross section of reactively scattered K (triangles and dashed curve) and KBr (circles and solid curve), centre of mass system, calculated using FV approximation for $K_2 + Br_2$. Open symbols denote positive branch, closed symbols negative branch.

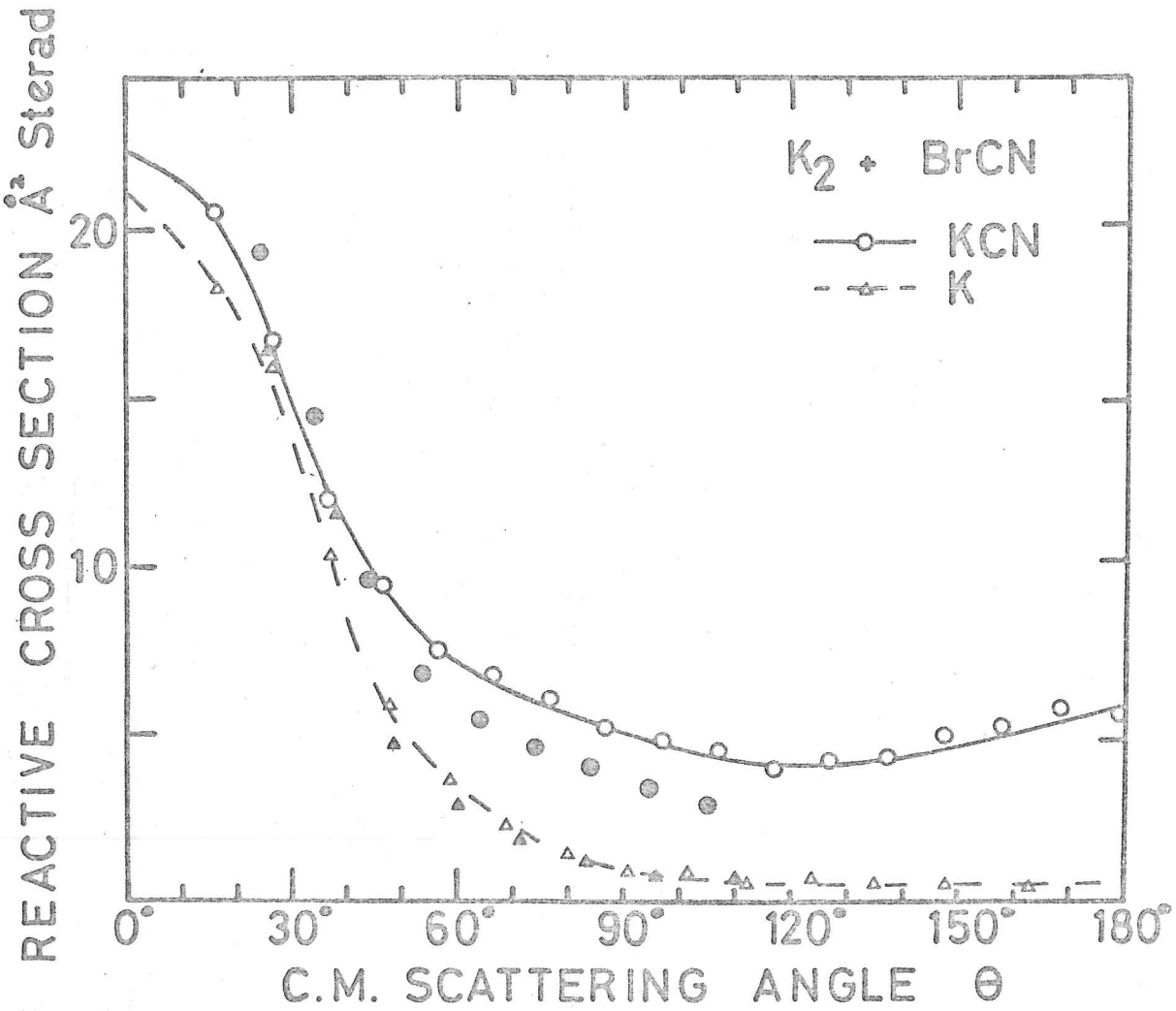

Figure 9: Differential cross section of reactively scattered K (triangles and dashed curve) and KCN (circles and solid curve), centre of mass system, calculated using FV approximation for K_2 + BrCN. Open symbols denote positive branch, closed symbols negative branch.

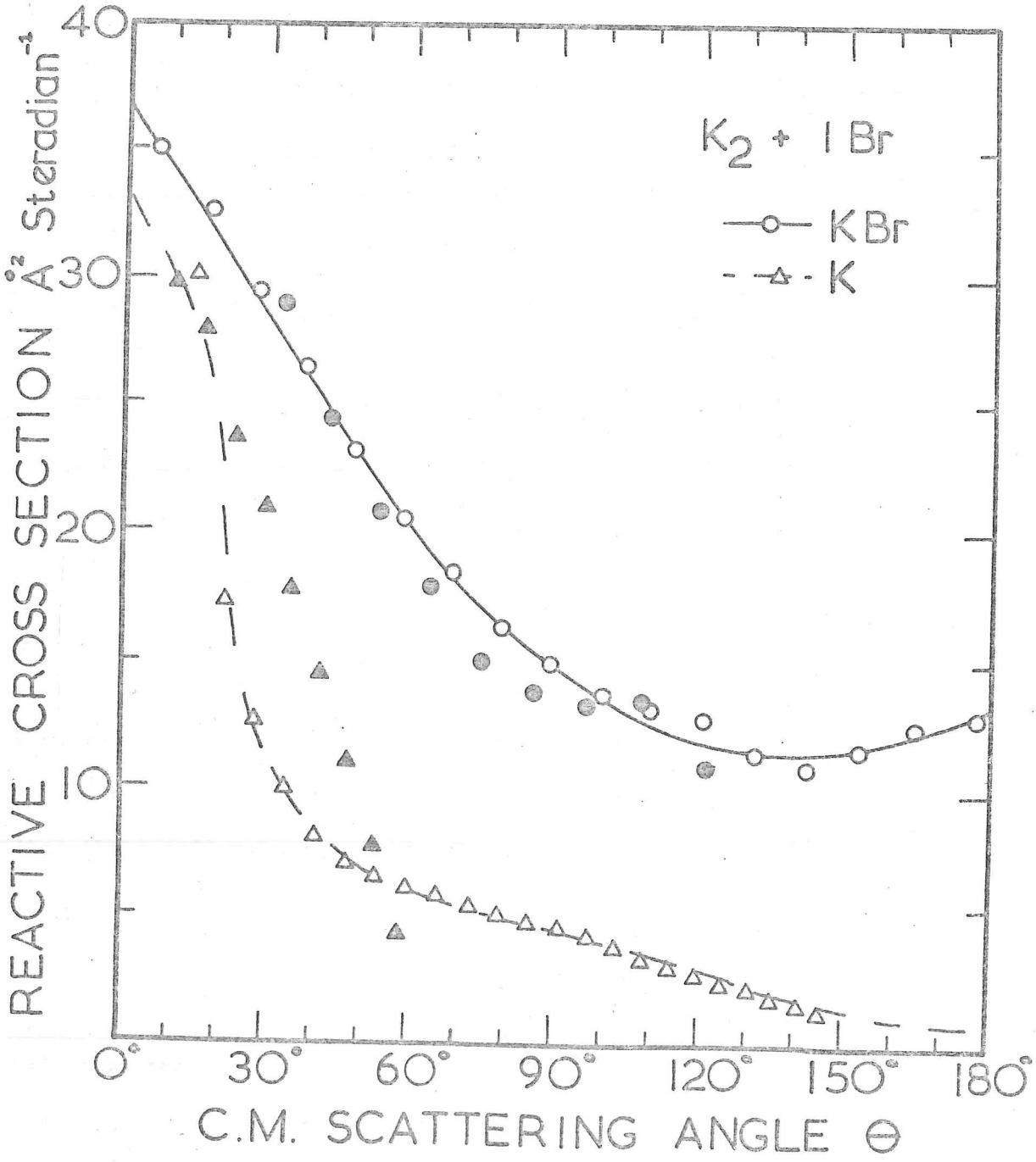

Figure 10: Differential cross section of reactively scattered K (triangles and dashed curve) and KBr (circles and solid curve), centre of mass system, calculated using FV approximation for K_2 + IBr. Open symbols denote positive branch, closed symbols negative branch.

differential cross-section, which is then transformed to laboratory coordinates averaging over a spread in the velocities of the product and reactant beams and the angle of intersection of the beams. The c.m. distributions which best reproduced the lab. distributions of KX and K for K_2 + Br_2, BrCN are shown in Figure 11. The poor matching in the case of IBr makes a similar treatment impossible.

Table 1 lists the centre of mass recoil velocities obtained from the FV and c.m. to lab. transformations, the elastic K_2 velocities, the reaction exoergicities and the ratio of the total reactive cross sections for K and KX products. The determination of the absolute values of the total reactive cross sections is only approximate, however the ratio of the values is likely to be more meaningful. For K_2 + BrCN, both atom and cyanide product have approximately the same c.m. recoil velocity, whereas for K_2 + Br_2, the K atom product has a recoil velocity in excess of the K_2 elastic velocity and much greater than the recoil velocity of the KBr product.

Discussion

K_2 + Br_2, BrCN, IBr Two main points arise from the results:

(a) that the centre of mass distributions of the K and KX products peak in the forward direction with about the same intensity, but the K atom distributions fall more rapidly than do the KX distributions at wide angles.

(b) that the centre of mass recoil velocity of K is greater than that of KX for the reaction K_2 + Br_2, but these velocities are about the same for the reaction K_2 + BrCN.

The large total reaction cross sections for these reactions indicate that the initial electron jump occurs at large internuclear distances

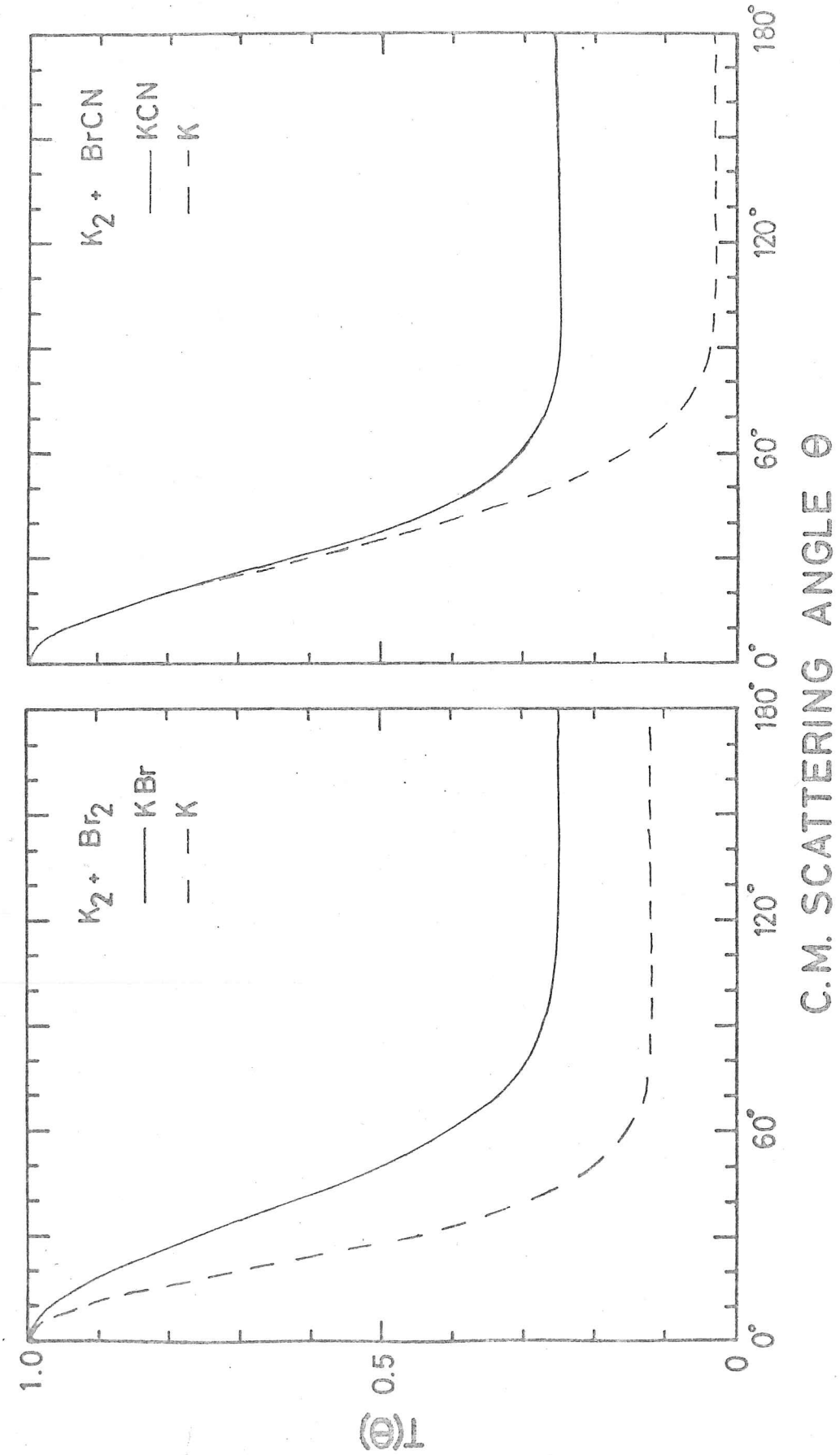

Figure 11: Angular distribution in centre of mass system, $T(\theta)$, for reactively scattered K and KBr from K_2 + Br_2, BrCN by stochastic analysis.

Table 1

	Br_2	BrCN	IBr
Elastic K_2 velocity	771	664	826
KX velocity (FV)	385	500	320
K velocity (FV)	1100	450	(1100)
KX velocity (cm-lab)	700	800	600
K velocity (cm-lab)	1400	600	-
ΔD_o	33	7	36
Q_K/Q_{KX}	0.60	0.47	-

Notes: a) All velocities in $m.sec^{-1}$.

b) ΔD_o in $kcal.mole^{-1}$, for products KX + K + Y.

($r_c \sim 5 - 8\mathring{A}$). Thus most reactive collisions will occur at large impact parameters ($b \sim r_c$), outside the range of hard sphere repulsive interactions. The observation (a) of equal forward intensities for both products suggests that at large impact parameters the dynamics of the reaction procede via the steps of Eq.4 to give K + KX as products. Using the centre of mass recoil velocities derived from the FV approximation (table 1), it is possible to determine a recoil kinetic energy (E') for the encounter $K_2 + X_2 \longrightarrow KX + K + X$. These values, together with the initial relative translational energies are listed in table 2 for $K_2 + Br_2$, BrCN. They indicate that, for $K_2 + Br_2$, $\sim$ 50% of the available energy (initial relative kinetic energy and reaction exoergicity) appears as relative translational energy of the products; for K_2 + BrCN $\sim$ 45% of the initial energy appears as product kinetic energy. These figures are much larger than the corresponding values for the atom reaction $K + X_2$; for thermal reactions (5, 6) the values are 3% and 9% for $K + Br_2$, BrCN respectively and for supersonic reactions (8) the values are 9% and 12%. However, the approximate nature of the recoil velocities derived from the FV transformation should be borne in mind. It is possible to regard the reaction mechanism as two successive dissociations: firstly the dissociation to give K_2X and X and then the dissociation of K_2X to give KX + K. The FV velocities of table 1 may be used to estimate the relative translational energies of the two dissociations for $K_2 + Br_2$, BrCN. These values are shown in table 2. It is apparent that the recoil kinetic energy for the first dissociation ($E'_{K_2X,X}$) accounts for almost all the total recoil energy (E'); this contribution depends on the relative velocity and reduced mass of the K_2X and X products, which are much larger than those for the

Table 2

	Br_2	BrCN
E	8.3	7.2
E'	20.2	6.5
$E'_{K_2X,X}$	18.4	6.5
$E'_{KX,K}$	1.8	0.01

Note: a) Energies in $kcal.mole^{-1}$.

KX, K dissociation. Consideration of the total angular momentum for the thermal reaction M + Br_2 (14) shows that about half of the initial angular momentum (which is almost all orbital angular momentum, $\underline{L}$) appears as internal angular momentum of the products, $\underline{J}'$. Assuming that K_2 behaves as an alkali atom, about half of the initial angular momentum (L_m (K_2+Br_2) ~ 650$\hbar$) should appear as internal angular momentum of the fragment $K_2^+Br^-$ (J'_m(K_2Br)~ 300$\hbar$) which will recoil forwards in the direction of the initial K_2. If the internal angular momentum $\underline{J}'$ of $K_2^+Br^-$ is parallel to the initial angular momentum vector $\underline{L}$, the subsequent dissociation of the $K_2^+Br^-$ will give K going forward and KBr backwards with respect to the centre of mass of the $K_2^+Br^-$. As the relative velocity of the KBr,K is much smaller than the K_2Br,Br relative velocity both KBr and K will recoil forwards with respect to the original centre of mass, as is observed. This model requires that the internal angular momentum vector be polarised perpendicular to the initial relative velocity vector (i.e. parallel to the initial orbital angular momentum vector $\underline{L}$). Recent studies (15) have shown that such polarisation is not observed for the reaction of thermal Cs + Br_2. However for K_2 + Br_2 the initial orbital angular momentum is higher (~650$\hbar$ for K_2 + Br_2, compared with ~300$\hbar$ for Cs + Br_2) and the initial relative kinetic energy is higher (8.3 kcal $mole^{-1}$ for K_2 + Br_2, compared with 0.9 kcal $mole^{-1}$ for Cs + Br_2). As the initial kinetic energy increases, it has been suggested that the dynamics of the reaction are likely to approach the limit of spectator stripping (16, 17), in which case polarisation of $\underline{J}$ is likely to occur.

Calculations (18) of the potential energy surface for the KNaCl system have shown a well in the surface corresponding to a triangular

KNaCl complex being ~ 15 kcal mole^{-1} more stable than K + NaCl. Molecular beam studies (19) for similar exchange reactions M + M'X show that the reactions proceed via a long-lived complex. The $K_2^+Br^-$ formed in the reaction K_2 + Br_2 is overenergised by about 30 kcal mole^{-1} leading to a shorter lifetime and less randomisation of energy disposal. Monte Carlo trajectory studies (20) on reactions forming ionic bonds show that for a potential energy surface (2M) where there is 0.5 kcal mole^{-1} repulsive energy release in the diatomic bond and charge migration in the diatomic molecule is permitted, there is forward peaking in the angular distribution and that 13% of the total energy appears as product translational energy. The encounters involve secondary interactions ("clutching") before separation of the products and result in collision lifetimes ~ 7 - 17 x 10^{-13} sec. This is to be compared with the time (3) of ~ 2 x 10^{-13} sec for K_2^+ + Br_2^- to approach under the influence of the Coulomb attraction. The dissociation of the K_2Br will follow rather quickly on the separation of the K_2Br, Br, so Eq.4 should be regarded as a concerted mechanism, rather than identifiable steps, and the dissociation of the K_2Br is unlikely to dispose the internal energy of the K_2Br into translation as is indicated by the low value of $E'_{KX,K}$ in table 2. For K_2 + BrCN, the K_2CN fragment formed in large impact collisions only has an excess energy of ~ 7 kcal mole^{-1}. Thus the K_2CN intermediate is likely to be long-lived dissociating with a greater degree of energy redistribution. The similarity in recoil velocities for K,KCN would support this view. The mechanism of Eq.4 would consist of well defined steps.

The equal forward intensities of both K and KX products would suggest that at large impact parameters the dynamics of the reaction

are entirely governed by the mechanism of Eq.4. However, the reduced intensity of K scattering compared with KX at wide angles suggests that this mechanism does not apply at small impact parameters. It has been proposed (1-3) that at small impact parameters more complicated four-centre dynamics are appropriate, involving the quadrupolar K_2XY intermediate (K_2Br_2 is stable with respect to 2KBr by 40 kcal $mole^{-1}$) giving rise to KX, KY products. Examination of figures 8 - 10 would suggest that this mechanism predominates at small impact parameters more in the case of K_2 + BrCN, IBr than for K_2 + Br_2 where the proportion of K atom scattering is higher for $\Theta > 90^\circ$. However the ratios of total reactive cross sections Q_K/Q_{KX} (table 1) indicate that 75% of the total scattering for K_2 + Br_2 and 65% for K_2 + BrCN gives K + KX reaction products rather than KX and KY.

The poor FV matching in the case of the K atom distribution from K_2 + IBr appears to be due to the reduced laboratory intensity of K for positive angles ($10^\circ < \Theta < 35^\circ$), which is not noticed for K_2 + Br_2. As the elastic scattering distributions for K_2 + IBr and K_2 + Br_2 have the same shape, this discrepancy has its origin in the slower fall-off of the supersonic K + IBr elastic scattering compared with the supersonic K + Br_2 elastic scattering. This is not observed (7) for the thermal K + IBr, Br_2 elastic scattering distributions. A possible explanation is that the increased relative translational energy in the supersonic K + IBr gives rise to highly vibrationally excited KI product scattering in the direction of the centre of mass vector which is partially detected by the Pt/W filament (4). This might explain why the positive and negative branches of the elastic scattering of supersonic K + IBr do not superimpose; although this effect is also noticed for supersonic K + Br_2.

$K_2 + SnCl_4$ In this case, the similarity in shape of the elastic scattering distributions for atoms and dimers indicates fairly certainly that there is no K atom product. This would suggest (2, 3) a reaction path of the form

$$K_2 + SnCl_4 \longrightarrow 2KCl + SnCl_2 \qquad (5)$$

possibly proceeding via a K_2SnCl_4 intermediate dissociating to $(KCl)_2$ (bound by 40-50 kcal $mole^{-1}$). Such an explanation is likely as the reaction $K + SnCl_4$ is found (8) to proceed via a long-lived intermediate.

References

(1) P. B. Foreman, G. M. Kendall and R. Grice, Mol.Phys. 23, 127 (1972).

(2) P. B. Foreman, Ph.D. Thesis (Cambridge University, 1971).

(3) G. M. Kendall, Ph.D. Thesis (Cambridge University, 1972).

(4) K. T. Gillen and R. B. Bernstein, Chem.Phys.Letters 5, 275 (1970).

(5) J. H. Birely, R. R. Herm, K. R. Wilson and D. R. Herschbach, J.Chem.Phys. 47, 993 (1967).

(6) R. Grice, M. R. Cossandey and D. R. Herschbach, Ber.Bunsenges.phys.Chem. 72, 975 (1968).

(7) G. H. Kwei and D. R. Herschbach, J.Chem.Phys. 51, 1742 (1969).

(8) Chapter I.

(9) W. S. Struve, T. Kitagawa and D. R. Herschbach, J.Chem.Phys. 54, 2759 (1971).

(10) R. Grice, Ph.D. Thesis (Harvard University, 1967).

(11) D. R. Herschbach, Adv.Chem.Phys. 10, 319 (1966).

(12) P. B. Foreman, G. M. Kendall and R. Grice, Mol.Phys. 23, 117 (1972).

(13) E. A. Entemann, Ph.D. Thesis (Harvard University, 1967).

(14) C. Maltz and D. R. Herschbach, Disc.Farad.Soc. 44, 176 (1967).

(15) C. Maltz, N. D. Weinstein and D. R. Herschbach, Mol.Phys. 24, 133 (1972).

(16) R. E. Minturn, S. Datz and R. L. Becker, J.Chem.Phys. 44, 1149 (1966).

(17) J. C. Polanyi, Disc.Farad.Soc. 44, 293 (1967).

(18) A. C. Roach and M. S. Child, Mol.Phys. 14, 1 (1968)

(19) W. B. Miller, S. A. Safron and D. R. Herschbach, Disc.Farad. Soc. 44, 108 (1972).

(20) P. J. Kuntz, M. H. Mok and J. C. Polanyi, J.Chem.Phys. 50, 4623 (1969).

CHAPTER III

SEMIEMPIRICAL POTENTIAL-ENERGY SURFACES FOR ALKALI-METAL EXCHANGE REACTIONS $M + M_2' \longrightarrow MM' + M'$

Introduction

One of the simplest reactive systems for chemists to study is that of bimolecular exchange reactions and in order to discuss the reaction rates and dynamics observed, there is needed a knowledge of the potential-energy surfaces for these reactions. Recently, a range of alkali-metal exchange reactions has been studied using molecular beam techniques (1). Clusters of three or more alkali-metal atoms are known (2) to be produced in nozzle expansions of alkali-metal vapours. The stability of a three-body intermediate in an exchange reaction affects the dynamics of the reaction. A large well in the potential-energy surface may, at normal collision energies, give rise to long-lived complexes (3). If the well becomes shallower or the collision energy is increased the reaction dynamics become direct. Alternatively, if there is a saddle-point on the surface, its location in either the entrance or exit valley of the surface has consequences both for the product energy and angular distributions (4).

Potential energy surfaces for the thermo-neutral exchange reactions $Li + Li_2 \longrightarrow Li_2 + Li$ and $Na + Na_2 \longrightarrow Na_2 + Na$, the endoergic reaction $Na + Li_2 \longrightarrow NaLi + Li$ and the exoergic reaction $Li + Na_2 \longrightarrow NaLi + Na$ have been calculated using methods based on the London equation and also the theory of "diatomics-in-molecules" (5). Both these methods seek to construct three-body potentials from diatomic functions. Companion (6) has applied the "diatomics-in-molecules" technique to $Li + Li_2$. The only ab initio calculation on the Li_3 system is by Kahn and Goddard (7) who used effective potentials to represent the core

electrons and considered only one configuration of the Li_3 molecule. Pickup and Byers Brown (8) have used a psuedo-hamiltonian model to calculate the properties of Na_3 and K_3.

In addition, surfaces are presented for two exchange reactions of alkali atoms and heteronuclear alkali diatomic molecules: Li + NaLi and Na + LiNa.

Method

Heitler and London described the binding energy of H_2 by the expression

$$E_{\mp} = \frac{Q \mp J}{1 \mp S^2} \qquad (1)$$

where Q, J and S are the coulombic, exchange and overlap integrals. London extended this method to a three body system, H_3, by considering two independent, canonical valence-bond structures.

$$\phi_I = (H_1 - H_2, H_3) \text{ and } \phi_{II} = (H_1, H_2 - H_3) \qquad (2)$$

where in I atoms 1 and 2 are bonded, whereas in II 2 and 3 are bonded. The basis set for the system consists of a 1s orbital on each of the three H atoms. If it is assumed that the basis set is composed of orthogonal orbitals, then the London equation (9) results

$$E_{\pm} = Q_{12} + Q_{23} + Q_{13} \pm 2^{-\frac{1}{2}} \left[(J_{12}-J_{23})^2 + (J_{23}-J_{13})^2 + (J_{13}-J_{12})^2\right]^{\frac{1}{2}} \qquad (3)$$

This only involves the diatomic integrals of equation 1 evaluated at three internuclear distances r_{12}, r_{23} and r_{13}. In equations 1 and 3, the zero of energy refers to separated atoms and the lower sign corresponds to the state of lowest energy.

The first application of London's equation to calculating potential-energy surfaces for systems other than H_3 was by Eyring and Polanyi (10) [London-Eyring-Polanyi (LEP) surfaces]. They used equation 1 to obtain coulombic and exchange integrals by assuming

electrons and considered only one configuration of the Li_3 molecule. Pickup and Byers Brown (8) have used a psuedo-hamiltonian model to calculate the properties of Na_3 and K_3.

In addition, surfaces are presented for two exchange reactions of alkali atoms and heteronuclear alkali diatomic molecules: Li + NaLi and Na + LiNa.

Method

Heitler and London described the binding energy of H_2 by the expression

$$E_{\mp} = \frac{Q \mp J}{1 \mp S^2} \qquad (1)$$

where Q, J and S are the coulombic, exchange and overlap integrals. London extended this method to a three body system, H_3, by considering two independent, canonical valence-bond structures.

$$\phi_I = (H_1 - H_2, H_3) \text{ and } \phi_{II} = (H_1, H_2 - H_3) \qquad (2)$$

where in I atoms 1 and 2 are bonded, whereas in II 2 and 3 are bonded. The basis set for the system consists of a 1s orbital on each of the three H atoms. If it is assumed that the basis set is composed of orthogonal orbitals, then the London equation (9) results

$$E_{\pm} = Q_{12} + Q_{23} + Q_{13} \pm 2^{-\frac{1}{2}} \left[(J_{12}-J_{23})^2 + (J_{23}-J_{13})^2 + (J_{13}-J_{12})^2\right]^{\frac{1}{2}} \qquad (3)$$

This only involves the diatomic integrals of equation 1 evaluated at three internuclear distances r_{12}, r_{23} and r_{13}. In equations 1 and 3, the zero of energy refers to separated atoms and the lower sign corresponds to the state of lowest energy.

The first application of London's equation to calculating potential-energy surfaces for systems other than H_3 was by Eyring and Polanyi (10) [London-Eyring-Polanyi (LEP) surfaces]. They used equation 1 to obtain coulombic and exchange integrals by assuming

that the integrals are constant fractions of the singlet energy

$$Q = \rho \cdot E \quad \text{and} \quad J = (1 - \rho)\, E \qquad (4)$$

where ρ , independent of internuclear separation, is in the range 0.1 to 0.2 (commonly 0.14). A Morse potential function was used to represent the diatomic energy, E of Eq.4.

In a more recent modification, Sato (11) suggested that ρ be allowed to vary and an adjustable constant k be introduced. For a given k, the coulomb and exchange integrals may be obtained from the diatomic singlet and triplet functions

$$Q + J = (1 + k)\, {}^1\Sigma \qquad (5a)$$

$$Q - J = (1 - k)\, {}^3\Sigma \qquad (5b)$$

where ${}^1\Sigma$ (i.e. E_+ in Eq.1) is a Morse potential and ${}^3\Sigma$ (i.e. E_-) is an anti-Morse function defined by

$${}^3\Sigma(r) = \tfrac{1}{2} D_e \left\{ \exp\left[-2\beta(r - r_e)\right] + 2 \exp\left[-\beta (r - r_e)\right] \right\} \qquad (6)$$

where D_e, β and r_e are the usual Morse parameters. Surfaces obtained in this way are commonly used in trajectory studies and are designated London-Eyring-Polanyi-Sato (LEPS) potential-energy surfaces.

In a study on H_3, Cashion and Herschbach (12) used spectroscopic Rydberg-Klein-Rees (RKR) data for the ${}^1\Sigma g^+$ state of H_2 and theoretical data for the ${}^3\Sigma u^+$ state. Assuming that the overlap integral is zero, the coulomb and exchange integrals are obtained from the sum and difference of the singlet and triplet curves

$$Q = \tfrac{1}{2} ({}^1\Sigma + {}^3\Sigma) \quad \text{and} \quad J = \tfrac{1}{2} ({}^1\Sigma - {}^3\Sigma). \qquad (7)$$

The use of an accurate triplet function rather than an anti-Morse function gives better results than Sato's method.

In a more accurate treatment of H_3, Salomon (13) introduced an analytic expression for the 1s - 1s overlap integral (S), which is a function strongly dependent on internuclear separation. The

coulomb and exchange integrals are obtained from the simultaneous equations

$$Q + J = (1 + S^2)\ {}^1\Sigma \qquad (8a)$$

$$Q - J = (1 - S^2)\ {}^3\Sigma \qquad (8b)$$

This is analogous to equation 5 except that the constant k is replaced by S^2, a function of internuclear distance. Salomon brings his surfaces into agreement with experiment by varying a screening factor occurring in the expression for the overlap. These surfaces are in good agreement with those of Porter and Karplus (14) who started from the same assumptions as London, but did not use orthogonal orbitals in the basis set. This gives rise to the inclusion of three-centre exchange and overlap integrals in their expression for the three-body energy. Their surface for H_3 is probably the most accurate semi-empirical potential-energy surface.

In the diatomics-in-molecules method of Ellison (5), if the wave function for a molecular system is approximated as a limited set of canonical valence-bond structures, then all the energy matrix elements H_{nm} may be expressed in terms of overlap integrals S_{nm} and experimental or theoretical ground- and excited-state energies of the diatomic and atomic components of the molecule. The inclusion of the overlap integrals S_{nm} have relatively little influence on the final results.

As in the London method, for a triatomic molecule ABC with three valence s electrons, there are two canonical valence-bond structures (A-B C and A B-C). For the special case of a symmetrical bent or linear molecule ABA and neglecting overlap, the expressions for the three-body energies are

$$E_+ = \tfrac{1}{2}\,(3\ {}^1\Sigma^{AB} + {}^3\Sigma^{AB} + 2\,{}^3\Sigma^{AA}) \qquad 9(a)$$

$$E_- = \tfrac{1}{2}\,({}^1\Sigma^{AB} + 3\ {}^3\Sigma^{AB} + 2\ {}^1\Sigma^{AA}) \qquad 9(b)$$

where $^1\sum^{PQ}$ and $^3\sum^{PQ}$ are the singlet and triplet states of the diatomic molecule PQ. If the expressions for $^1\sum$ and $^3\sum$ in equation 9 are replaced by the expressions Q + J and Q - J respectively (i.e. equation 1 with $S^2 = 0$) then for this symmetrical system the London equation (equation 3) results.

This chapter describes the application of the London equation as suggested by Cashion and Herschbach and Salomon to the colinear Li_3, $NaLi_2$, $LiNa_2$ and Na_3 systems both with and without the inclusion of orbital overlap. The method of diatomics-in-molecules is employed to give energies for bent isosceles triangular configurations of these molecules. The values of the coulomb and exchange integrals are obtained from the singlet and triplet diatomic molecule potential curves and the values of the overlap integrals from expressions for the overlap of Slater-type orbitals.

The Diatomic Functions

The accuracy of a potential-energy surface is determined by the precision with which the diatomic functions are known. Only for the singlet states of Li_2 and Na_2 are accurate experimental values known. For NaLi, the only experimental observations (15) have been of the vibrational and rotational constants, the dipole moment, the polarisibilities and the nuclear quadrupole coupling constants. Thus it is necessary to use theoretically calculated values of the singlet state of NaLi and of all three triplet states. For the singlet state of Li_2 the spectroscopically-derived Rydberg-Klein-Rees (RKR) curve of Krupenie, Mason and Vanderslice (16) is used. This is extended for large inter-nuclear distances using the scaling procedure of Jenč and Plíva (17). The triplet

curve for Li_2 is that of Mannebuck (18) as quoted by Companion (19). At the worst, these triplet values differ by no more than 1.1 kcal. $mole^{-1}$ from those calculated by Wahl (20).

For NaLi, both the singlet and triplet functions are those calculated by Bertoncini, Das and Wahl (21). With no experimental evidence available it is difficult to assess the accuracy of these calculations. As a guide an analogous calculation by Das (22) on Li_2 ground state gives a dissociation energy (D_e) of 23.29 kcal. $mole^{-1}$ compared with the experimental value of 23.75 kcal.$mole^{-1}$ (23); a difference of $\sim$ 2%.

For Na_2, the potential energy function for the singlet state is the RKR curve of Demtroder, McClintock and Zare (24), extended for large internuclear separations in the manner described for Li_2. The triplet energies are from a calculation by Bertoncini and Wahl (25).

The overlap functions are calculated from the overlap of two s-type Slater-type orbitals (STO). For Li_2 the orbital exponents used in the 2s STOs are those given by Ransil (26) for the best LCAO-MO description of Li_2 ($z = 0.6335$). The exponent values of Bertoncini et al (21) are used for NaLi ($z_{Li} = 0.672$, $z_{Na} = 0.862$). For Na_2 the exponent value is that given by Slater's rules ($z_{Na} = 0.733$).

Results

For each of the four systems Li + Li_2, Na + Li_2, Li + Na_2 and Na + Na_2 three potential-energy surfaces were calculated. Surface (a) was calculated for a colinear system using the London equation and neglecting orbital overlap; surface (b) is for a colinear system, uses the London equation and includes overlap;

surface (c) is for a symmetric, isosceles triangular configuration and uses the "diatomics-in-molecules" method. For the systems Li + NaLi and Na + LiNa, surfaces of types (a) and (b) were calculated. The properties of the triatomic molecules are given in Table 1. The method used to calculate the vibrational frequencies is described fully in Appendix A.

Figures 1 to 6 show surfaces (a) and (b) for Li + Li_2, Na + Li_2, Li + NaLi, Li + Na_2, Na + LiNa and Na + Na_2, respectively. These are the surfaces corresponding to the E_- solution of the London equation (equation 3). Sections of the potential-energy surfaces for both colinear and isosceles triangular configurations are shown in Figures 7 to 10.

All the surfaces show the same general features. There is a shallow well extending far into the entrance and exit valleys. The depth of the well decreases along the series Li + Li_2, Na + Li_2, Li + NaLi, Na + LiNa, Li + Na_2, and Na + Na_2. There is no potential energy barrier in the entrance or exit valleys of any surface. In all cases, the colinear configuration is more stable than the bent one. The effect of including orbital overlap [surfaces (b)] is to deepen the well by $\sim$ 2 kcal.mole^{-1} and to slightly decrease the internuclear separation. For the $NaLi_2$ system, the linear non-symmetric NaLiLi molecules is $\sim$ 2 kcal.mole^{-1} more stable than the linear symmetric LiNaLi molecules, in which the strong Li - Li interaction is reduced. However, for the $LiNa_2$ system the situation is reversed. The linear symmetric NaLiNa molecule is $\sim$ 1.5 kcal. mole^{-1} more stable than LiNaNa, due to the Na - Li interaction being stronger than the Na - Na interaction. Table 2 shows how the well depth varies with the nature of the three body intermediate for

Table 1

Properties of potential energy surfaces.
Energy kcal.mole^{-1}, distance Å, frequency cm^{-1}

A + BC	R_{AB}	R_{BC}	E_1 (d)	E_2 (e)	ΔD_e	W_1	W_2	W_3
Li + Li_2 (a)	2.81	2.81	-32.62	- 8.87	0	220	-	229
Li + Li_2 (b)	2.76	2.76	-34.54	-10.79	0	188	-	293
Li + Li_2 (c)	3.49	2.67	-30.90	- 7.15	0	162	301	189
Na + Li_2 (a)	3.18	2.79	-28.59	- 4.84	- 4.09	151	11	315
Na + Li_2 (b)	3.11	2.76	-30.24	- 6.49	- 4.09	130	14	300
Na + Li_2 (c)	3.74	2.67	-27.09	- 3.33	- 4.09	144	248	175
Li + NaLi(a)	3.11	3.11	-26.42	- 6.76	0	184	-	187
Li + NaLi(b)	3.00	3.00	-27.94	- 8.28	0	85	-	81
Li + Na_2 (a)	3.03	3.39	-23.90	- 6.61	+ 2.37	118	-	281
Li + Na_2 (b)	3.03	3.18	-25.54	- 8.25	+ 2.37	104	-	274
Li + Na_2 (c)	3.74	3.08	-20.63	- 3.33	+ 2.37	116	202	150
Na + LiNa(a)	3.10	3.10	-25.40	- 5.74	0	88	-	160
Na + LiNa(b)	3.03	3.03	-26.94	- 7.28	0	125	-	234
Na + Na_2 (a)	3.22	3.22	-22.13	- 4.84	0	104	-	145
Na + Na_2 (b)	3.13	3.13	-23.96	- 6.67	0	75	-	125
Na + Na_2 (c)	4.18	3.08	-20.29	- 2.29	0	61	178	116

Notes: a) Linear molecule, overlap not included.

b) Linear molecule, overlap included. 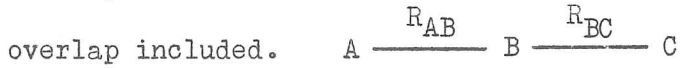

c) Isosceles molecule, overlap not included 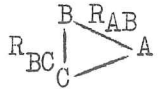

d) Energy with respect to separated atoms, zero point energy excluded.

e) Energy with respect to A + BC, zero point energy excluded.

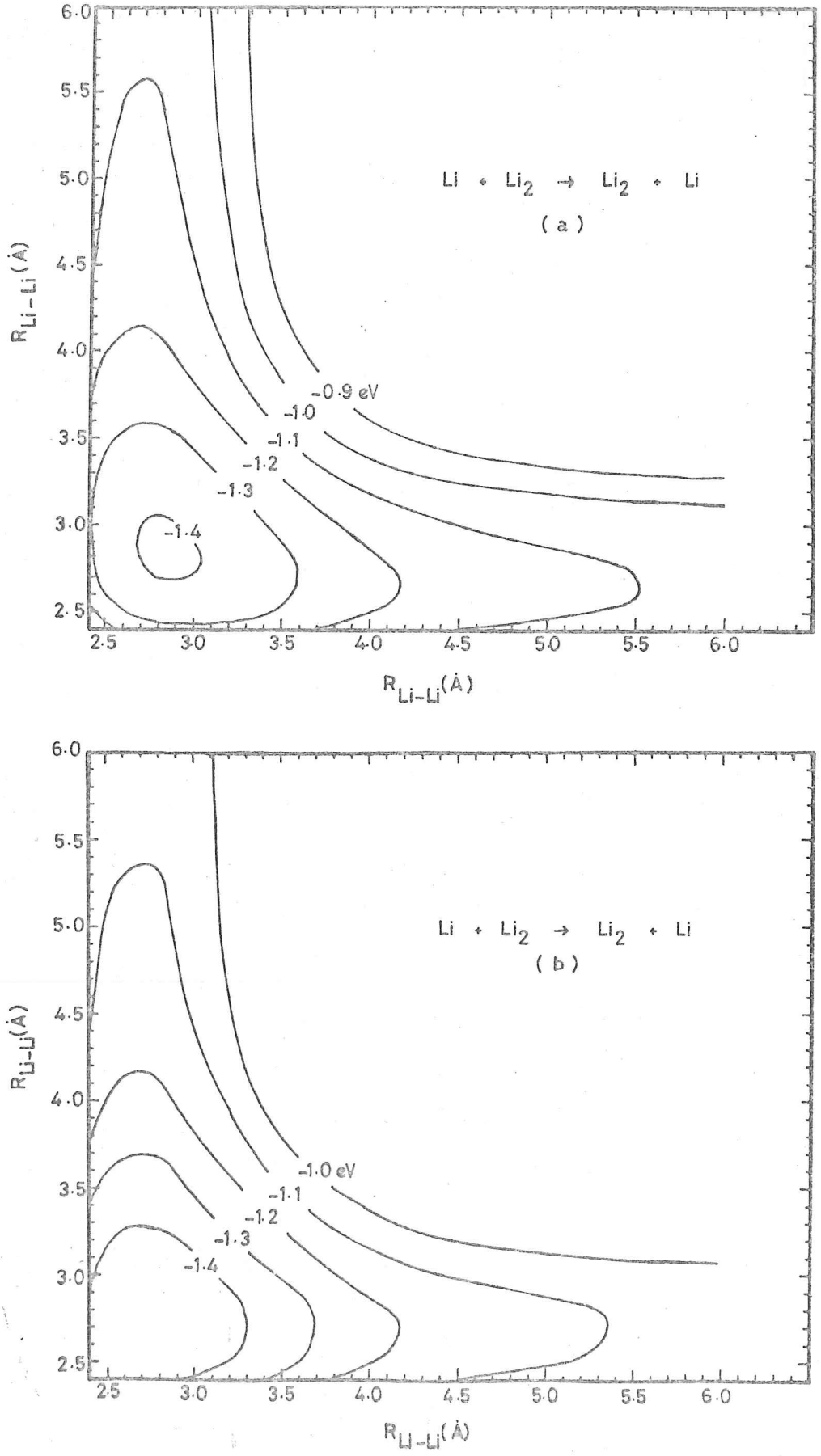

Figure 1: Potential-energy surfaces for the colinear system Li + Li_2 ⟶ Li_2 + Li. Both surfaces are calculated using the London equation: surface (a) does not include orbital overlap, surface (b) does. Contours are plotted every 0.1 eV (2.3 kcal.mole^{-1}). The zero of energy refers to separated atoms.

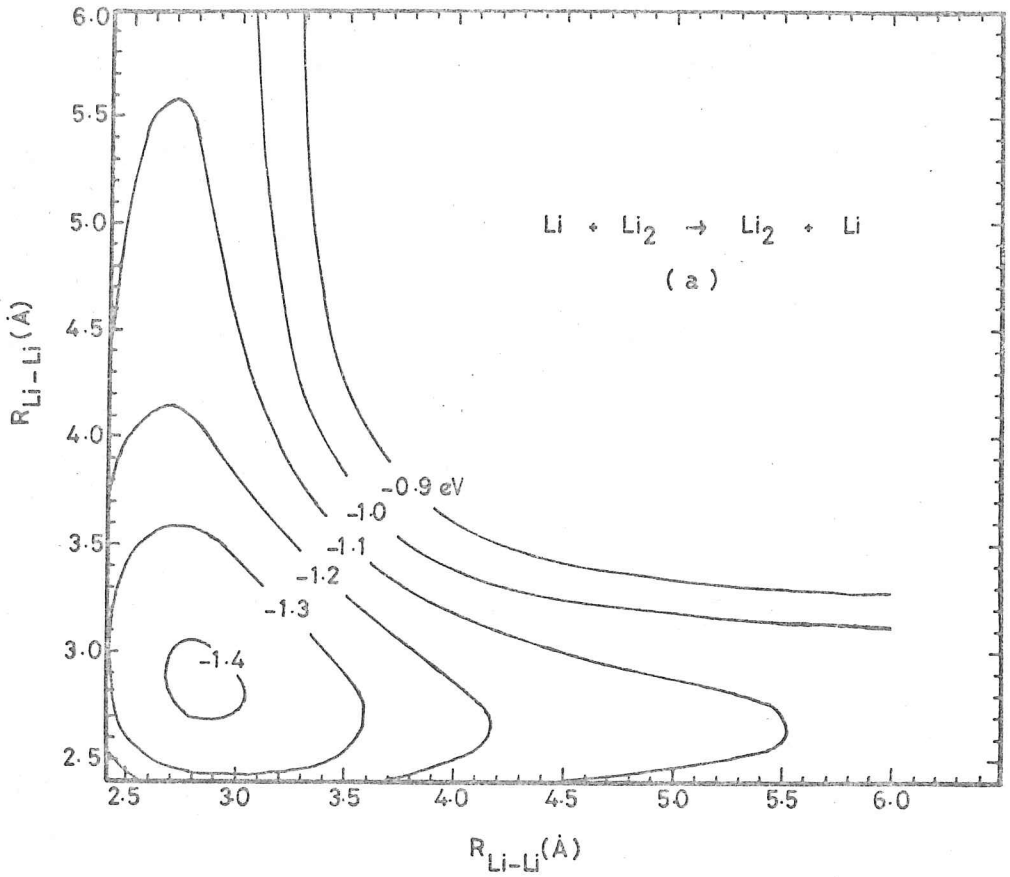

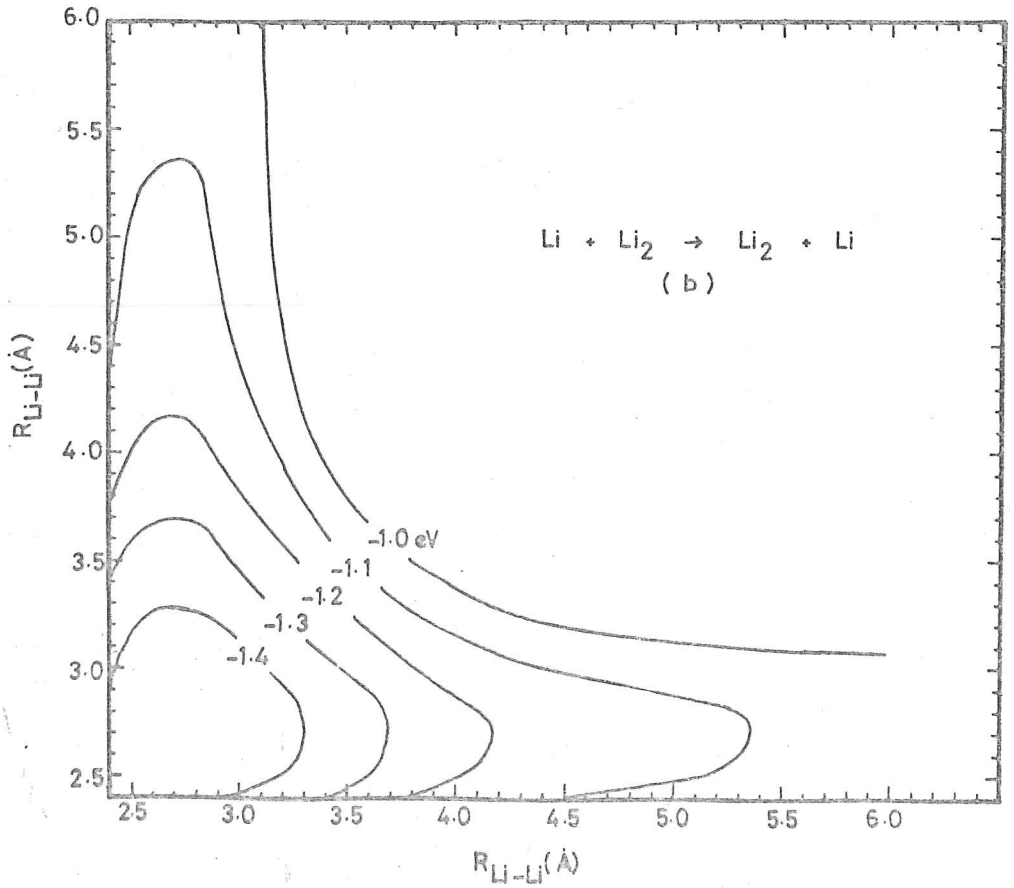

Figure 1: Potential-energy surfaces for the colinear system $Li + Li_2 \longrightarrow Li_2 + Li$. Both surfaces are calculated using the London equation: surface (a) does not include orbital overlap, surface (b) does. Contours are plotted every 0.1 eV (2.3 kcal.mole^{-1}). The zero of energy refers to separated atoms.

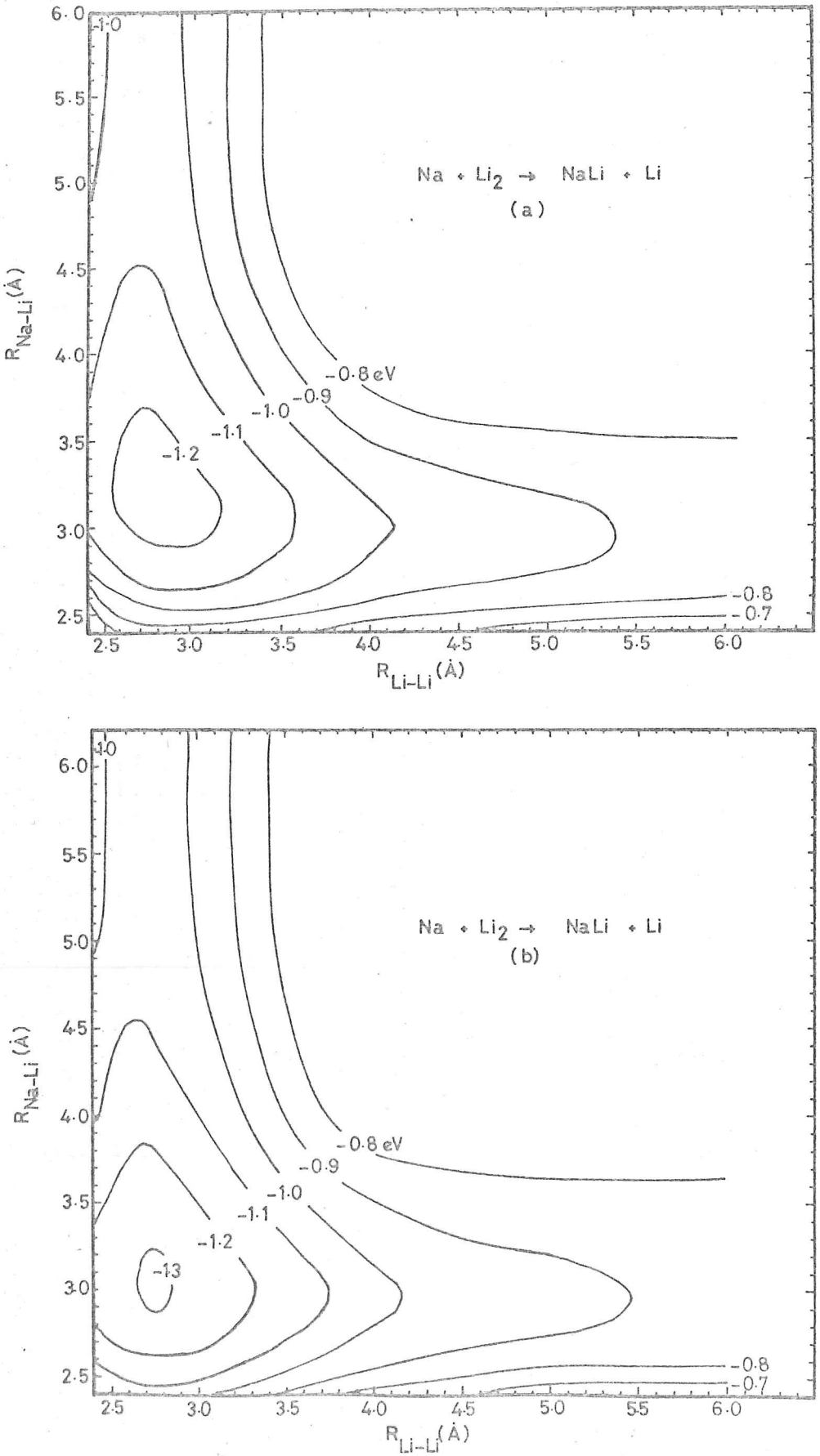

Figure 2: Potential-energy surfaces for the colinear system Na + Li_2 ⟶ NaLi + Li. Both surfaces are calculated using the London equation: surface (a) does not include orbital overlap, surface (b) does. Contours are plotted every 0.1 eV (2.3 kcal.mole^{-1}). The zero of energy refers to separated atoms.

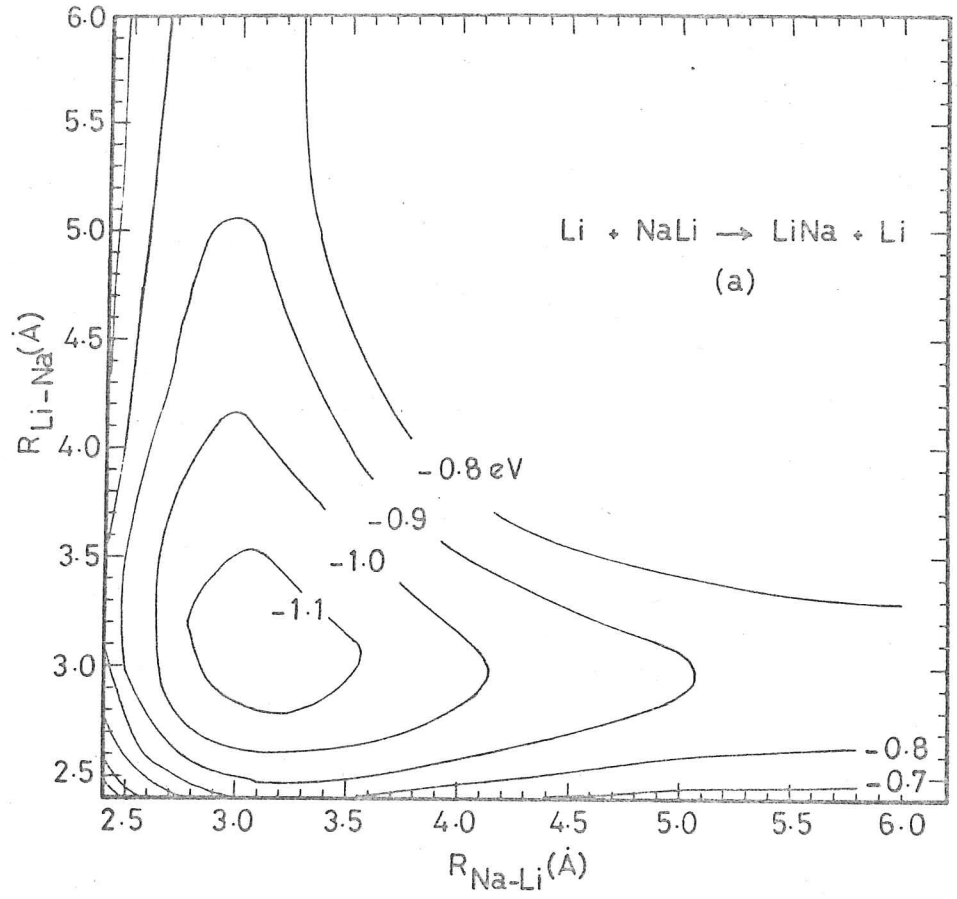

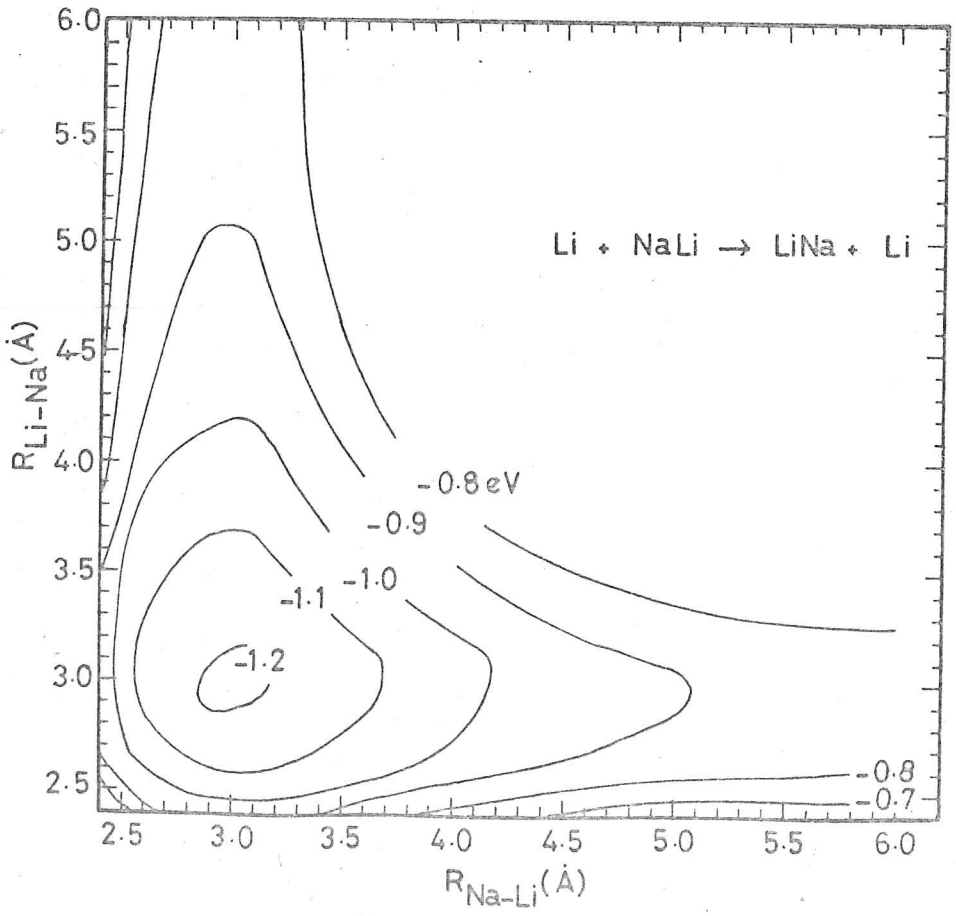

Figure 3: Potential energy surface for the colinear system Li + NaLi ⟶ LiNa + Li. Both surfaces are calculated using the London equation: surface (a) does not include orbital overlap, surface (b) does. Contours are plotted every 0.1 eV (2.3 kcal.mole^{-1}). The zero of energy refers to separated atoms.

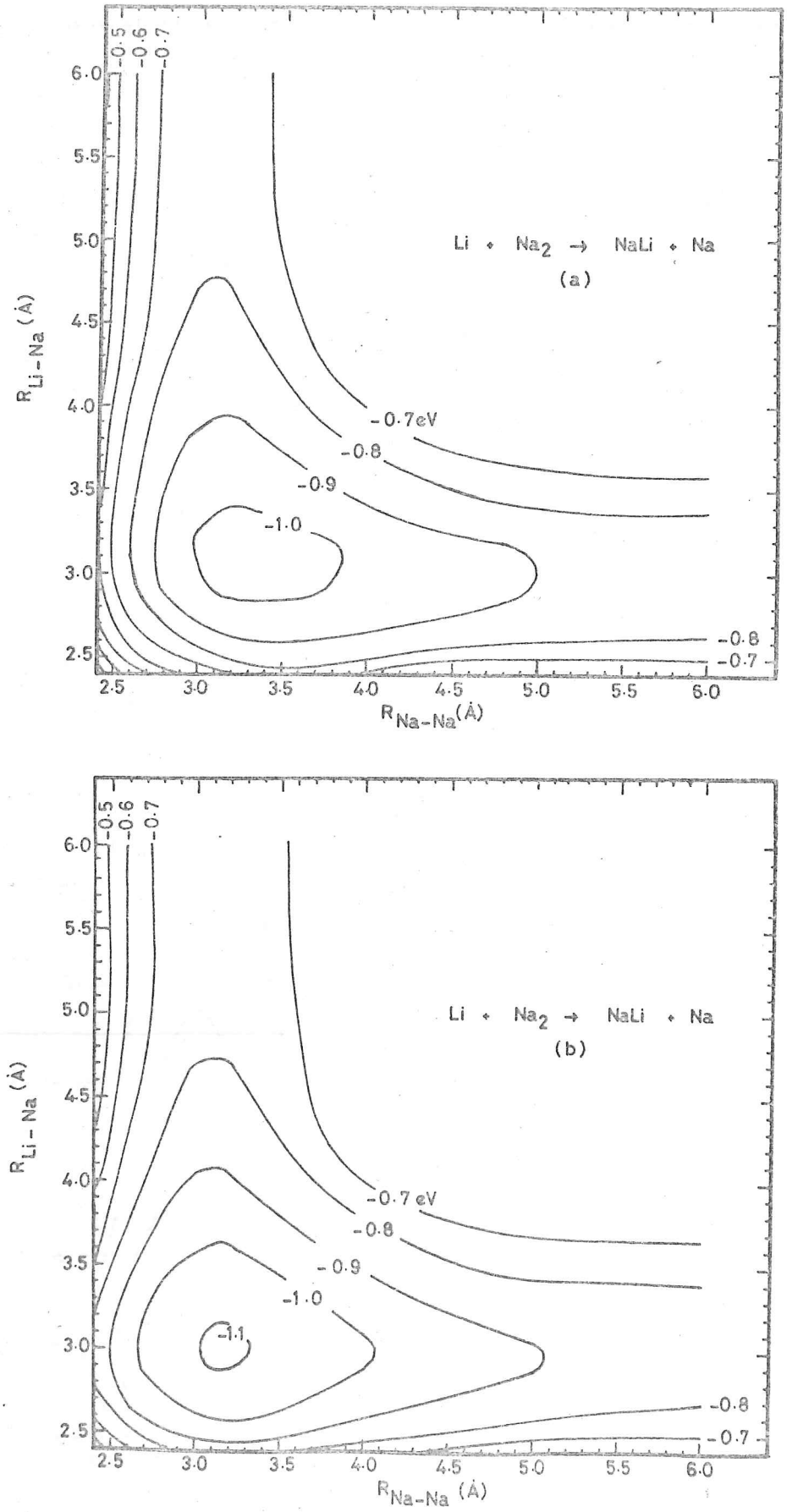

Figure 4: Potential-energy surfaces for the colinear system Li + Na_2 ⟶ NaLi + Na. Both surfaces are calculated using the London equation: surface (a) does not include orbital overlap, surface (b) does. Contours are plotted every 0.1 eV (2.3 kcal.mole^{-1}). The zero of energy refers to separated atoms.

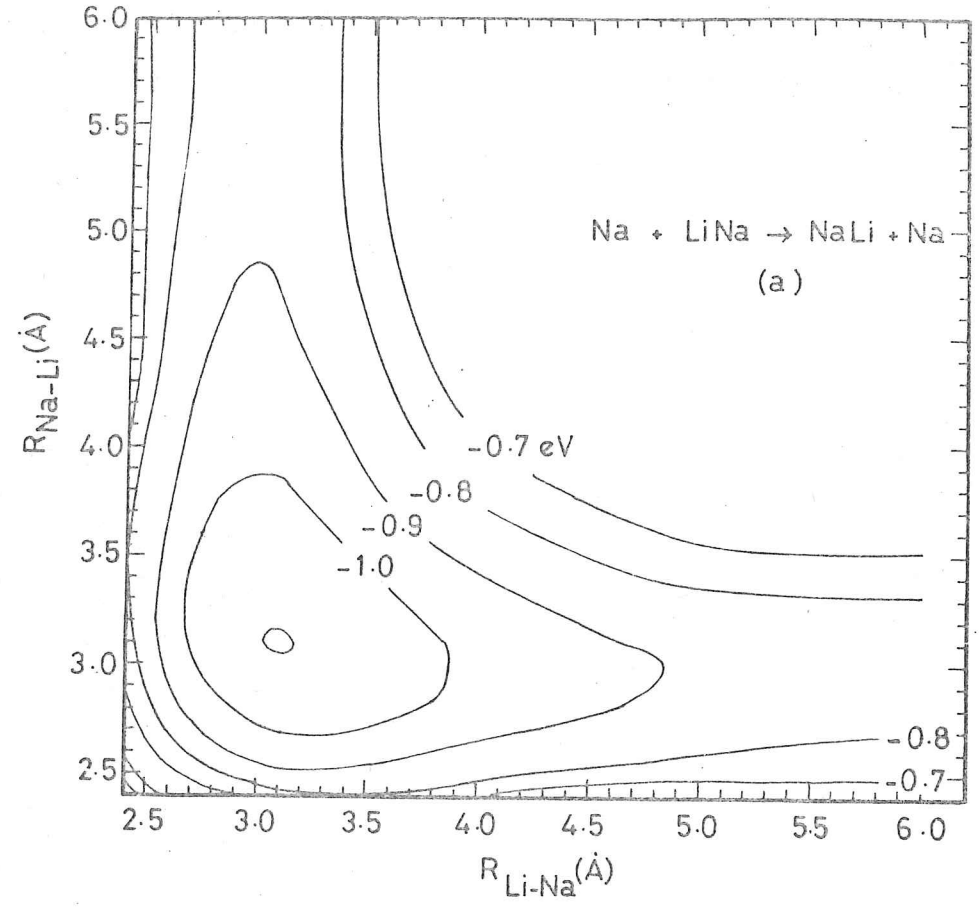

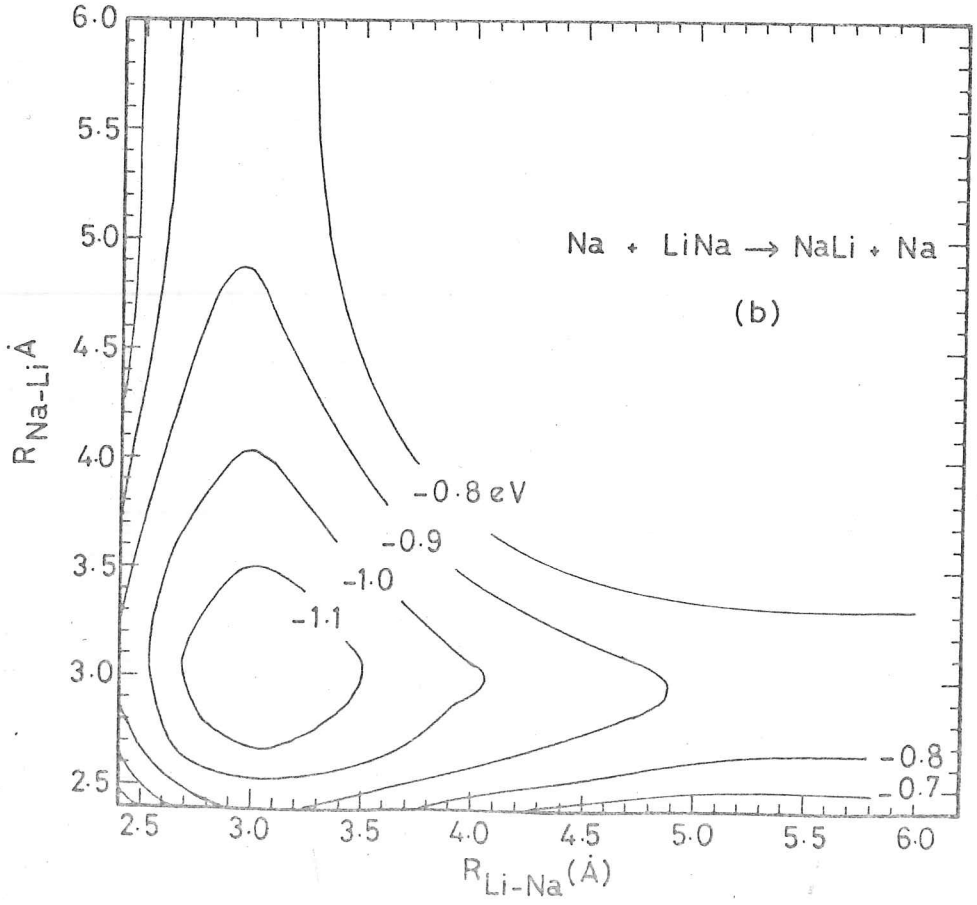

Figure 5: Potential-energy surfaces for the colinear system Na + LiNa ⟶ NaLi + Na. Both surfaces are calculated using the London equation: surface (a) does not include orbital overlap, surface (b) does. Contours are plotted every 0.1 eV (2.3 kcal.mole^{-1}). The zero of energy refers to separated atoms.

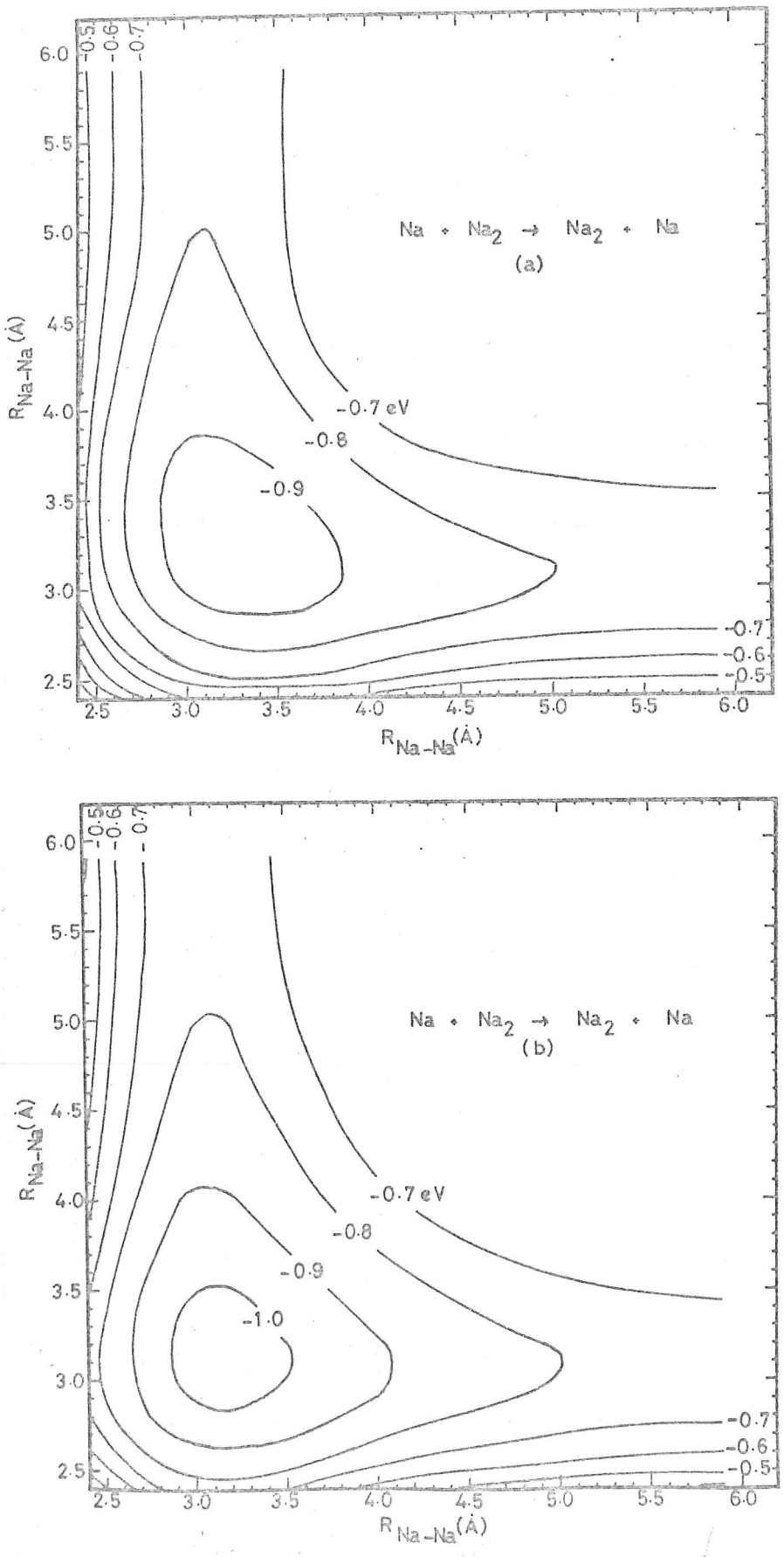

Figure 6: Potential-energy surfaces for the colinear system Na + Na_2 ⟶ Na_2 + Na. Both surfaces are calculated using the London equation: surface (a) does not include orbital overlap, surface (b) does. Contours are plotted every 0.1 eV (2.3 kcal.mole^{-1}). The zero of energy refers to separated atoms.

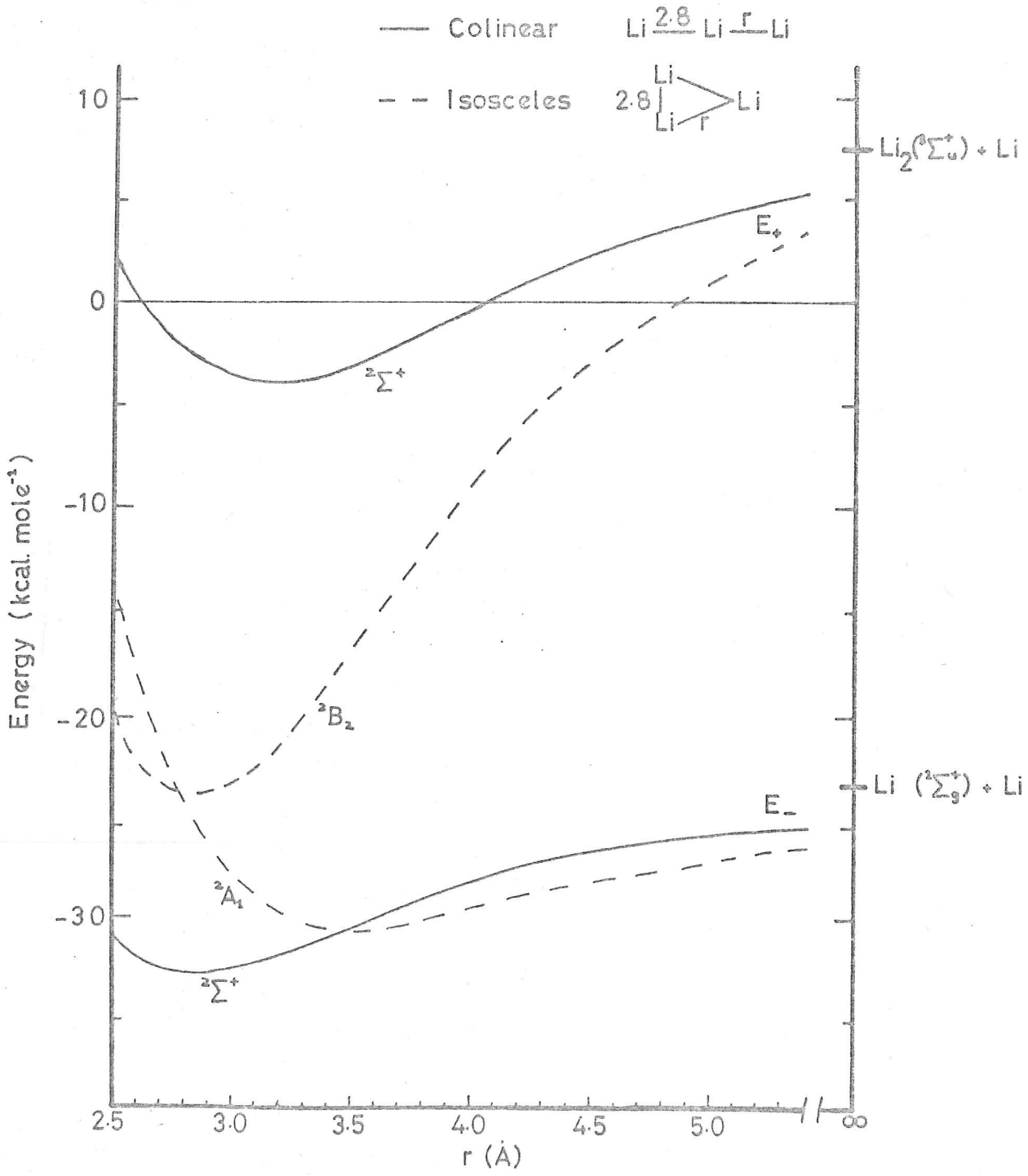

Figure 7: Sections of potential-energy surfaces for Li_3 for the approach of Li to Li_2 with Li_2 distance fixed at about the equilibrium value for colinear or isosceles orientations. The surfaces are calculated neglecting orbital overlap

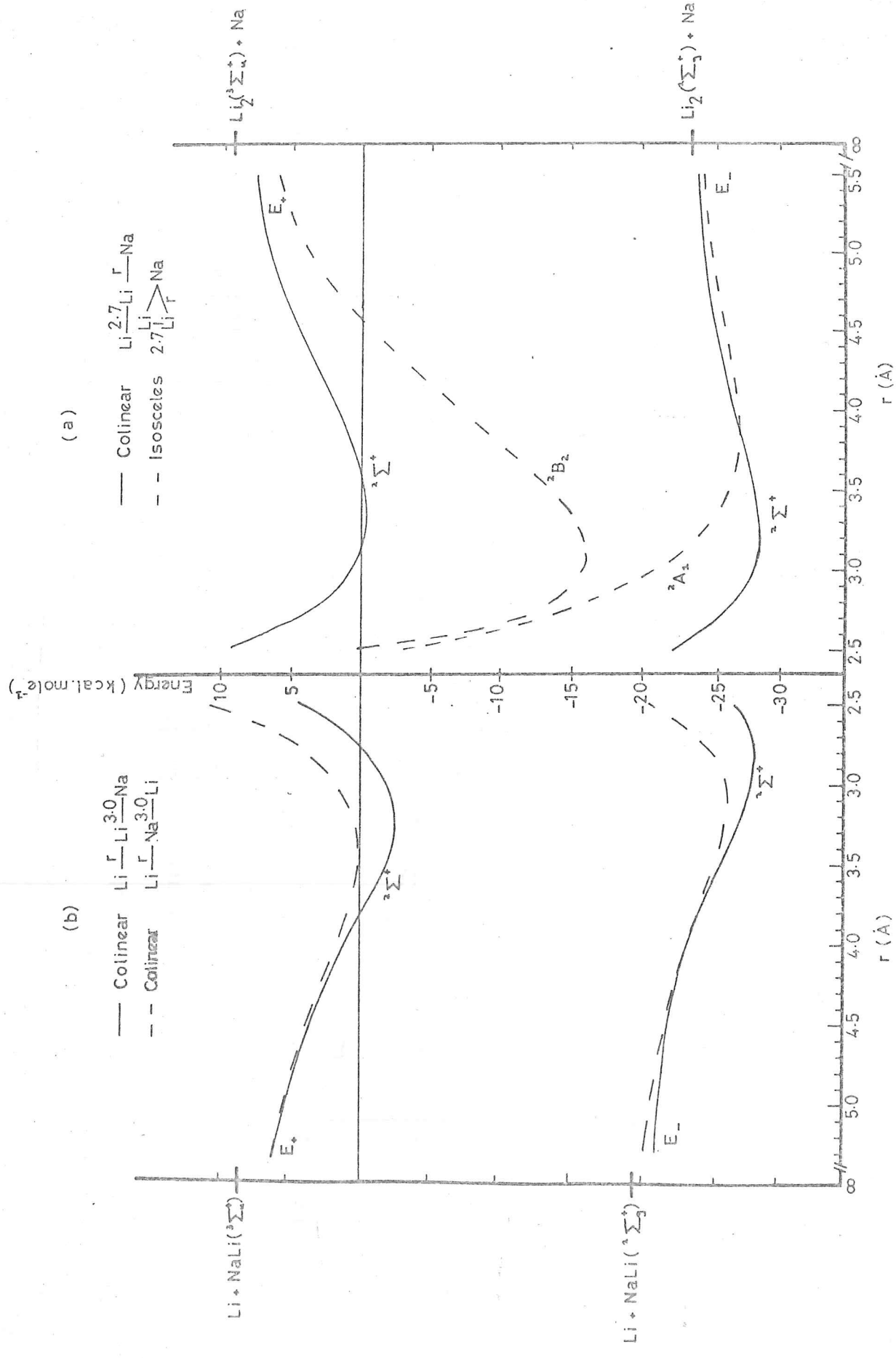

Figure 8: Sections of potential-energy surfaces for $NaLi_2$ (a) for the approach of Na to Li_2 with Li_2 distance fixed at about the equilibrium value for colinear or isosceles orientations and (b) for separation of NaLi + Li, with NaLi distance at about the equilibrium value, to either NaLi + Li or LiNa + Li. The surfaces are calculated neglecting orbital exchan

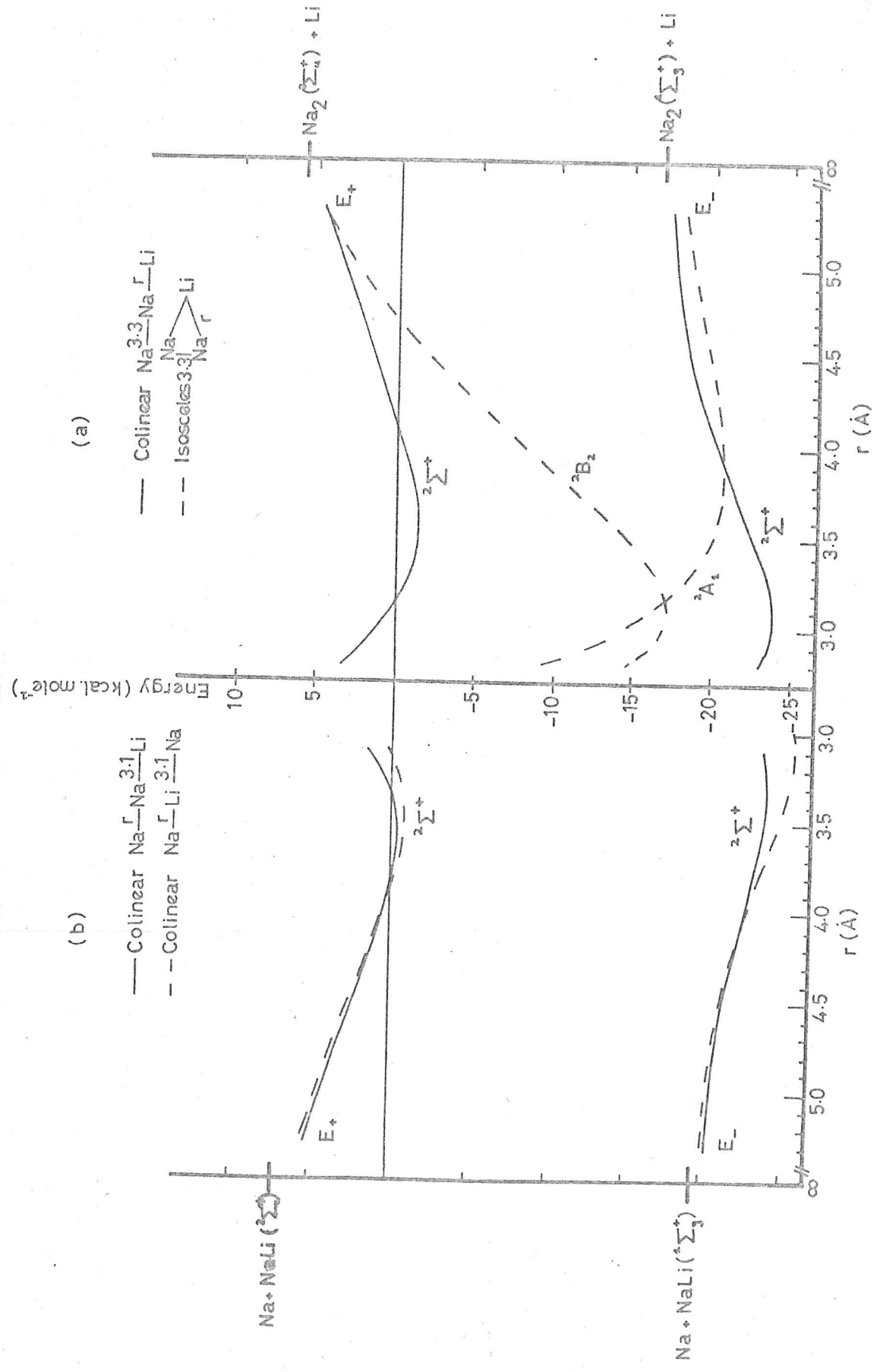

Figure 9: Sections of potential-energy surfaces for $LiNa_2$ (a) for the approach of Li to Na_2 with Na_2 distance fixed at about the equilibrium value for colinear or isosceles orientations and (b) for separation of LiNa + Na, with LiNa distance at about the equilibrium value, to either LiNa + Na or NaLi + Li. The surfaces are calculated neglecting orbital overlap.

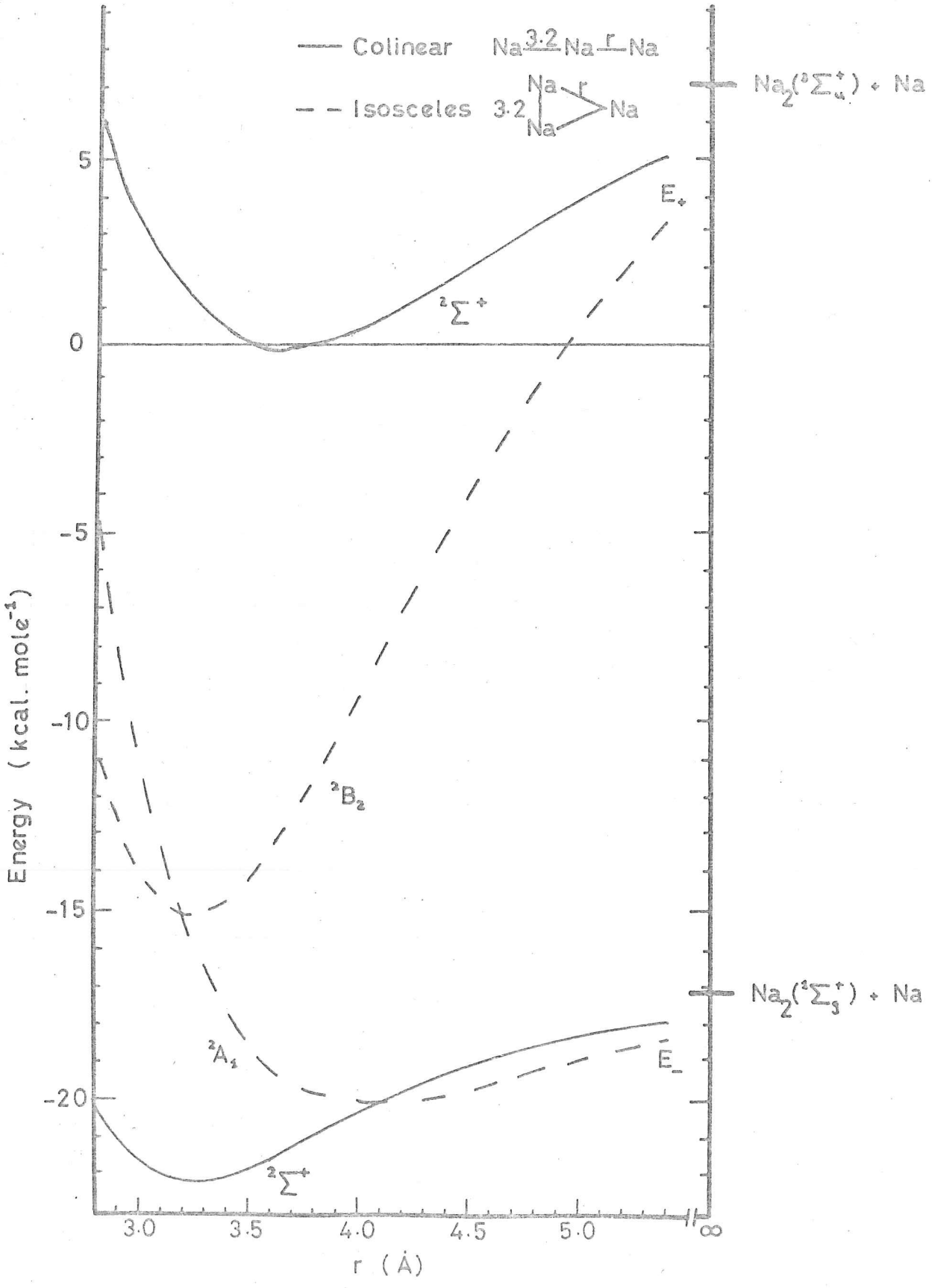

Figure 10: Sections of potential-energy surfaces for Na_3 for the approach of Na to Na_2 with Na_2 distance fixed at about the equilibrium value for colinear or isosceles orientations. The surfaces are calculated neglecting orbital overlap.

Table 2

Colinear reactive systems for different intermediates

	E_1	E_2
$Li + Li_2 \longrightarrow Li_3 \longrightarrow Li_2 + Li$	- 8.9	- 8.9
$Na + Li_2 \longrightarrow NaLi_2 \longrightarrow NaLi + Li$	- 4.8	- 8.9
$Na + Li_2 \longrightarrow LiNaLi \longrightarrow NaLi + Li$	- 2.7	- 6.8
$Li + Na_2 \longrightarrow LiNa_2 \longrightarrow LiNa + Na$	- 6.6	- 4.2
$Li + Na_2 \longrightarrow NaLiNa \longrightarrow LiNa + Na$	- 8.1	- 5.7
$Na + Na_2 \longrightarrow Na_3 \longrightarrow Na_2 + Na$	- 4.8	- 4.8

Notes: 1) Energies in kcal.mole^{-1}

2) E_1 is the energy of the well with respect to reactants; E_2 with respect to products. Zero point energies not included.

3) Overlap not included.

the colinear reactive systems Li + Li_2, Na + Li_2, Li + Na_2 and Na + Na_2.

In all cases, a triatomic molecule stable with respect to separated atom and diatomic molecule is predicted. These molecules have bond lengths greater than the corresponding parent diatomic molecules and the vibrational frequencies are generally smaller than the isolated diatomic fundamental frequencies. Due to the minimum in the Mannebuck triplet function for Li_2, the bending force constant is negative, thus the linear Li_3 molecule is predicted to be unstable with respect to bending. Companion (6) predicts that the linear molecule passes over to a slightly more stable bent form with C_{2v} symmetry and a bond angle of 137^o and a Li - Li separation of 2.84Å. As the bending force constant depends on the gradient of the diatomic triplet function at the terminal atom separation, a similar situation arises for LiNaLi. For Na_2, the minimum in the triplet state energy occurs at a distance greater than the terminal atom separation in Na_3, thus the bending force constant will be positive indicating that Na_3 will be stable with respect to bending. This is also the case for $NaLi_2$, NaLiNa and $LiNa_2$. However, the shallowness of the well near to the equilibrium position makes an accurate determination of the bending force constant impossible for $LiNa_2$, $NaLi_2$ and Na_3.

Pickup and Byers Brown (8) found that the potential energy surfaces for linear Na_3 and K_3 were not unlike that for H_3, having a saddle point corresponding to M_3. Thus they calculated that Na_3 and K_3 were stable with respect to three separated atoms by 7.7 kcal.mole^{-1} and 5.9 kcal.mole^{-1}, respectively, but were not stable with respect to separated atom and diatomic molecule. They

did not find a bent isosceles configuration that was stable even with respect to three separated atoms.

The surfaces labelled E_+ in Figures 7 to 10, which correlate with the excited triplet states of the diatomic molecules, show a strong orientation dependence. At short M - M' distances the $^2B_2$ state corresponding to an isosceles triangular configuration descends much more rapidly than does the linear $^2\Sigma^+$ state. In no case, however, does the $^2B_2$ state intersect the E_- surface corresponding to a linear MM'_2 molecule. In all cases the linear triatomic molecule ($^2\Sigma^+$) corresponding to E_- is the most stable configuration. This is not the case for the $H + M_2$ system, reported by Lee, Gordon and Herschbach (27), where the $^2B_2$ state is the one of lowest energy for small internuclear separations.

Discussion

It is interesting to examine the contributions which give rise to the stability of the triatomic alkali molecules. For a symmetric linear system, the London equation becomes

$$E_- = 2Q(r_t) + Q(2r_t) - (J(2r_t) - J(r_t)). \qquad (10)$$

Using the Heitler-London expression for the energy (E_D) of the parent diatomic at its equilibrium separation (r_e), the energy of the triatomic molecule with respect to the diatomic molecule is

$$E_- - E_D = [2Q(r_t) - Q(r_e)] + [Q(2r_t) - J(2r_t)] + [J(r_t) - J(r_e)] \qquad (11)$$

As the minimum in the Coulombic energy Q occurs at a distance greater than the diatomic equilibrium distance and $r_t > r_e$ for all the systems studied, the first term in Eq.11 always contributes to the stability of the molecule. The second term is the diatomic triplet energy at $2r_t$ which is negative for Li_2 contributing $\sim$ 1 kcals.mole^{-1} to

the stability of Li_3. For Na_3, this term is positive (~ 0.02 kcal. $mole^{-1}$) compared with ~ 6.9 kcals.$mole^{-1}$ for the first term. The third term is always positive as the magnitude of the exchange integrals (which are negative for the systems studied) decreases monatonically to zero with internuclear distance. Table 3 gives values for the terms in equation 11 for H_3, Li_3 and Na_3. The H_3

	$2Q(r_t) - Q(r_e)$	$Q(2r_t) - J(2r_e)$	$J(r_t) - J(r_e)$
H_3	- 27.14	7.53	32.49
Li_3	- 9.24	- 1.10	1.48
Na_3	- 6.85	0.024	1.14

Table 3: Terms involved in Eq.11. Energies in Kcal.$mole^{-1}$. Data for H_3 from Ref.28.

molecule is unstable by ~ 12 kcal.$mole^{-1}$ with respect to separated $H + H_2$. This arises from the very large value of the third term involving the exchange integral. For Li_3 and Na_3 the third term is much smaller than the coulombic first term giving an overall stability. This is due to the increased fraction of the diatomic binding energy that is coulombic. At the diatomic equilibrium separations, the coulombic fractions of the binding energies are -0.12, 0.28 and 0.25 for H_3, Li_3 and Na_3 respectively; and at the triatomic moleculear internuclear distances 0.07, 0.31 and 0.30 respectively. The addition of the interaction of the terminal atoms increases the instability of H_3, stabilises Li_3 and makes little difference to Na_3. The equilibrium separation in an M_3 molecule seems to be determined by a tendency to minimise the exchange terms and optimise the coulomb term. The predominant interactions appear to be those between adjacent atoms.

It is not easy to assess the quantitative accuracy of these potential-energy surfaces as the methods have several inherent possible sources of error.

The first possible error arises from the triplet curves that are used. (The singlet curves, except for NaLi, are correct to within experimental observation.) However for Li_3 a vertical displacement of $\sim$ 4.5 kcal.mole^{-1} upwards would be necessary to remove the stability with respect to separated atom and molecule. For Na_3 a displacement of $\sim$ 2.5 kcal.mole^{-1} would be required.

A second source of error is the neglect of three-centre terms in the London equation and the "diatomics-in-molecules" theory. The inadequacies of the London equation have been discussed by Coolidge and James (28), who concluded that it was only a fortuitous cancellation of three-centre terms for H_3 that made the London equation yield such good results. Companion (6) concludes that all contributions except a double exchange of 2s electrons in Li_3 effectively cancel out by analogy with H_3. This term will enhance the stability of Li_3, but is expected to be smaller for Li_3 than for H_3, by comparison with the relative magnitudes of the diatomic exchange integrals of Li_2 and H_2, as mentioned above.

Another source of error arises from the fact that these surfaces are specifically covalent and only include s electrons. At small internuclear separations there will be a crossing of the covalent $M' + M_2$ surface by the ionic $M'^- + M^+_2$ surface. The internuclear distance r_c at which the ionic surface crosses the asymptote of the covalent surface is given by the relation

$$1/r_c = I_{M_2} - E_{M'} \qquad (12)$$

where I_{M_2} is the ionisation potential of M_2 and $E_{M'}$ is the electron

affinity of M'. For Li_2, NaLi, and Na_2 the ionisation potentials (29, 21) are 4.96, 4.99 and 4.87 eV respectively; the electron affinities (30) of Li, Na are 0.62 and 0.54 eV respectively. For the Li_3, $NaLi_2$, LiNaLi, $LiNa_2$, NaLiNa and Na_3 surfaces this gives r_c values of 3.32, 3.26, 3.29, 3.39, 3.24 and 3.36 Å respectively. The actual crossing of the two surfaces will occur at a slightly smaller distance than r_c as the covalent M' + M_2 surface is at a lower energy at r_c than its asymptotic value. However, the value is still greater than the values of the internuclear separation given in Table 1. The ionic nature of the surface at small separations would tend to lower the energy of the surface so that the qualitative features of a well would still remain. The nature of the bonding is likely to become less s in character as the alkali atom gets heavier and s, p and d states become closer in energy. However, the evaluation of coulomb and exchange integrals from diatomic potential curves, rather than by integration of s-type wavefunctions in the strict Heitler-London sense, does implicitly include ionic-coupling and p, d bond character.

A semi-empirical method, such as this, can only be justified by its simplicity and accuracy. An ab initio calculation of the surfaces described in this chapter would take many hours of hard computing; the results presented here represent only a few minutes computing time. That the surfaces are qualitatively correct can be justified by the existence of alkali clusters. For systems involving the heavier alkalis K, Rb and Cs the trend in this work would seem to indicate that the stability of the triatomic alkali molecule would decrease as the alkali gets heavier. Without accurate triplet potential energy curves for

K_2, Rb_2 and Cs_2 it is not possible to say if the well is replaced by a potential barrier. Further experiments and accurate calculations are needed to gain more information about potential-energy surfaces for alkali-metal exchange reactions.

References

(1) Chapter 4.

(2) E. J. Robbins, R. E. Leckenby and P. Willis, Adv.Phys.16, 739 (1967).
P. J. Foster, R. E. Leckenby and E. J. Robbins, J.Phys.B2, 478 (1969).
P. J. Foster, Ph.D. Thesis (University of Manchester, 1970).

(3) W. B. Miller, S. A. Safron and D. R. Herschbach, Disc. Faraday Soc.44, 108 (1967).
D. O. Ham and J. L. Kinsey, J.Chem.Phys.53, 285 (1970).

(4) J. C. Polanyi and W. H. Wong, J.Chem.Phys.51, 1439 (1969).
M. H. Mok and J. C. Polanyi, J.Chem.Phys.51, 1451 (1969).
J. C. Polanyi, Acc.Chem.Research 5, 161 (1972).

(5) F. O. Ellison, J.Am.Chem.Soc.85, 3540 (1963).

(6) A. L. Companion, D. J. Steible and A. J. Starshak, J.Chem.Phys.49, 3637 (1968).

(7) L. R. Kahn and W. A. Goddard, J.Chem.Phys.56, 2685 (1972).

(8) B. T. Pickup and W. Byers Brown, Mol.Phys.23, 1189 (1972).

(9) F. London, Z.Electrochem.35, 552 (1929).

(10) H. Eyring and M. Polanyi, Z.Phys.Chem.B12, 279 (1931).

(11) S. Sato, J.Chem.Phys.23, 592, 2465 (1955).

(12) J. K. Cashion and D. R. Herschbach, J.Chem.Phys.40, 2358 (1964).

(13) M. Salomon, J.Chem.Phys.51, 2406 (1969).

(14) R. N. Porter and M. Karplus, J.Chem.Phys.40, 1105 (1964).

(15) M. M. Hessel, Phys.Rev.Letters 26, 215 (1971).
J. Graff, P. J. Dagdigian and L. Wharton, J.Chem.Phys 57, 710 (1972).

(16) P. H. Krupenie, E. A. Mason and J. T. Vanderslice, J.Chem. Phys.39, 2399 (1963).

(17) F. Jenč and J. Plíva, Collection Czechoslov.Chem.Comm.28, 1449 (1963).

(18) C. Mannebuck, Physica 29, 769 (1963).

(19) A. L. Companion, J.Chem.Phys.48, 1186 (1968).

(20) A. C. Wahl, private communication (1970).

(21) P. J. Bertoncini, G. Das and A. C. Wahl, J.Chem.Phys. 52, 5112 (1970).

(22) G. Das, J.Chem.Phys. 46, 1568 (1965).

(23) G. Herzberg, Spectra of Diatomic Molecules (D.Van Nostrand Co. Inc., Princeton, New Jersey, 1950) 2nd Ed.

(24) W. Demtröder, M. McClintock and R. N. Zare, J.Chem.Phys. 51, 5495 (1969).

(25) P. Bertoncini and A. C. Wahl, private communication (1972).

(26) B. J. Ransil, Rev.Mod.Phys. 32, 245 (1960).

(27) Y. T. Lee, R. J. Gordon and D. R. Herschbach, J.Chem.Phys. 54, 2410 (1971).

(28) W. Kolos and L. Wolniewicz, J.Chem.Phys. 43, 2429 (1965).

(29) E. W. Robbins and R. F. Barrow, Proc.Chem.Soc., 329 (1961).

(30) A. W. Weiss, Phys.Rev. 166, 70 (1968).

(31) A. S. Coolidge and H. M. James, J.Chem.Phys.2, 811 (1934).

CHAPTER IV

A MOLECULAR BEAM STUDY OF ALKALI METAL EXCHANGE REACTIONS

Introduction

A wide range of bimolecular exchange reactions of the form A + BC $\longrightarrow$ AB + C has been studied using the technique of reactive scattering from crossed molecular beams and almost as wide a range of reaction dynamics observed. Historically, the first reactions studied were those involving alkali atoms for which surface ionisation made the experiments relatively easy by providing a detection system with almost unit efficiency. More than ten years elapsed before techniques of mass spectrometric detection and ultra high vacua obtaining partial pressures $\sim 10^{-14}$ torr. were sufficiently refined to allow a study of systems not involving alkali atoms. Herschbach (1) gives a recent review of all atom-molecule encounters studied using beams techniques. The types of reactions studied range from the direct dynamics of $M + XY \longrightarrow MX + Y$ (where M = alkali atom, X,Y = halogen atoms) where the approaching M atom transfers an electron to the XY molecule at a large separation ($\sim 8\text{Å}$), the XY^- breaks up as M^+ approaches and the MX product continues in the direction of the M atom, to the long-lived complex behaviour observed in the reactions $M + XM' \longrightarrow MX + M'$(2) where the approach of M to XM' is governed by long-range dipole-induced dipole interactions and a MXM' intermediate existing for $10^{-11} - 10^{-12}$ sec (several rotational periods and many vibrational periods) is formed. The angular distribution of products in centre of mass coordinates is symmetric about $\theta = 90^\circ$ and the energy disposal into the products agrees with a statistical unimolecular decay. An intermediate type of behaviour in which a complex is formed with a lifetime comparable to the

rotational period (an "osculating-complex" model (3)) is found for the halogen atom-halogen molecule exchange reactions $X + YZ \longrightarrow XY + Z$ (4). The centre of mass angular distributions show forward and backward peaking with the intensity of the forward peak greater than that of the backward peak (in the long-lived complex model, the peaks have the same intensity). It is thought that these reactions are governed by short range interactions.

The reactions of H atoms with XY halogen molecules (5) show a marked difference in the centre-of-mass scattering distributions as the identity of the halogen molecule XY changes. There is a transition from sideways ($\theta \sim 95^{\circ}$) to backwards ($\theta \sim 180^{\circ}$) which is interpretted as being the result of preferred orientations of the H-X-Y molecule (ranging from linear to bent). Another series of reactions in which a pronounced orientation effect is observed is that of the exchange reactions $H + M_2 \longrightarrow HM + M$, where the approach of H in a direction perpendicular to the M-M bond is preferred. A spectator model in which the M_2 bond breaks and MH forms without momentum transfer to the M product and in which the orientation of M_2 with respect to the initial relative velocity vector is fixed, is proposed ("oriented spectator" model).

This chapter describes seven alkali atom-alkali dimer exchange reactions of the form $M' + M_2 \longrightarrow M'M + M$. The systems studied are $Na + K_2$, Rb_2 and Cs_2, $K + Rb_2$, Cs, $Rb + K_2$ and $Cs + Rb_2$. There is a great similarity in the dissociation energies of alkali dimers ($\sim$ 10 - 12 kcal.mole^{-1}) so the energetics of these reactions are not very different. The potential energy surface calculations of the previous chapter show $M'M_2$ molecules to be stable with respect to isolated $M' + M_2$. In addition, $M'M_2$ molecules have been observed experimentally (7).

In these experiments, the alkali metal atom beam is produced with thermal energies and the dimer beam, produced by a nozzle expansion, is

a supersonic beam and is vibrationally excited by $\sim 4 \pm 4$ kcal.mole^{-1} (8). Under these conditions two reaction paths are possible:

$$M' + M_2 \longrightarrow M'M + M \qquad (I)$$

$$M' + M_2 \longrightarrow M' + M + M \qquad (II)$$

(the production of an electronically excited state of M is energetically inaccessible in these reactions). Path I is slightly exoergic for Na + K_2, Rb_2, Cs_2 and K + Rb_2 and slightly endoergic for Cs, Rb + K_2 and Cs + Rb_2. Path II is endoergic by $\sim$ 10 - 12 kcal.mole^{-1} for all the systems studied and is only energetically accessible for Cs, Rb + K_2 and Cs + Rb_2 if vibrational excitation is included.

Experimental Conditions

These experiments were carried out using the molecular beam apparatus, Aphrodite, the design and construction of which are described fully elsewhere (8-10). Briefly, the apparatus consists of two stainless steel vacuum chambers pumped by oil diffusion pumps and an inner copper chamber cooled by liquid nitrogen. The smaller of the two chambers houses the alkali dimer oven which is mounted on a platform which can be manipulated from outside the chamber for alignment purposes. The dimer oven is a nozzle source and the resulting beam which contains a mixture of alkali dimers and atoms passes through an inhomogeneous magnetic field which deflects the atoms out of the beam; a slit is placed allowing only dimers to enter the main chamber, where they are crossed by a beam of alkali atoms produced from a cross-beam oven mounted inside the main chamber. The main chamber has a lid rotatable about the scattering centre defined by the point of intersection of the beams. Through this lid passes a quadrupole mass filter fitted with a surface ionisation detector to measure the angular distribution of products.

A plan view of the ovens, detector and cold shielding is shown in figure 1. The apparatus has only been modified by the addition of an alkali atom oven and a quadrupole mass filter detector. These pieces of equipment are described in detail below.

Alkali Atom Oven

A cross section of the oven is shown in figure 2. The oven consists of three parts; a lower rectangular vaporisation chamber with a cylindrical cavity and holes drilled crosswise for the heating wires (0.5mm tantalum wire threaded through alumina insulators), a neck and a head. All the parts were machined from non-magnetic stainless steel (En58J) and were nickel-brazed together. The neck and head are heated by thermocoax* wrapped round the outside. The temperature of the head and body were monitored continuously using chromel-alumel thermocouples. The oven lid is secured by 12 4BA bolts and sealed by two 0.25mm Ni foil washers. The lower chamber of the oven has a capacity of at least 50g. of alkali metal.

The oven is supported by three stainless pins fitting into V-grooves machined into the bottom of the oven. This provides a unique reproducible oven position. The pins are on a stainless steel platform which is supported from two thickwalled brass tubes which supply water to the water-cooled cold shield and pass through a flange on the outside of the machine. The oven, surrounded by a 0.25mm tantalum radiation shield, is enclosed in a water-cooled copper box brazed to the brass water pipes. The lid and front of the box are removable to allow access to the oven for filling. The water-cooled cold shield is

---

*Pye-Unicam Ltd., Manor Royal, Crawley, Sussex.

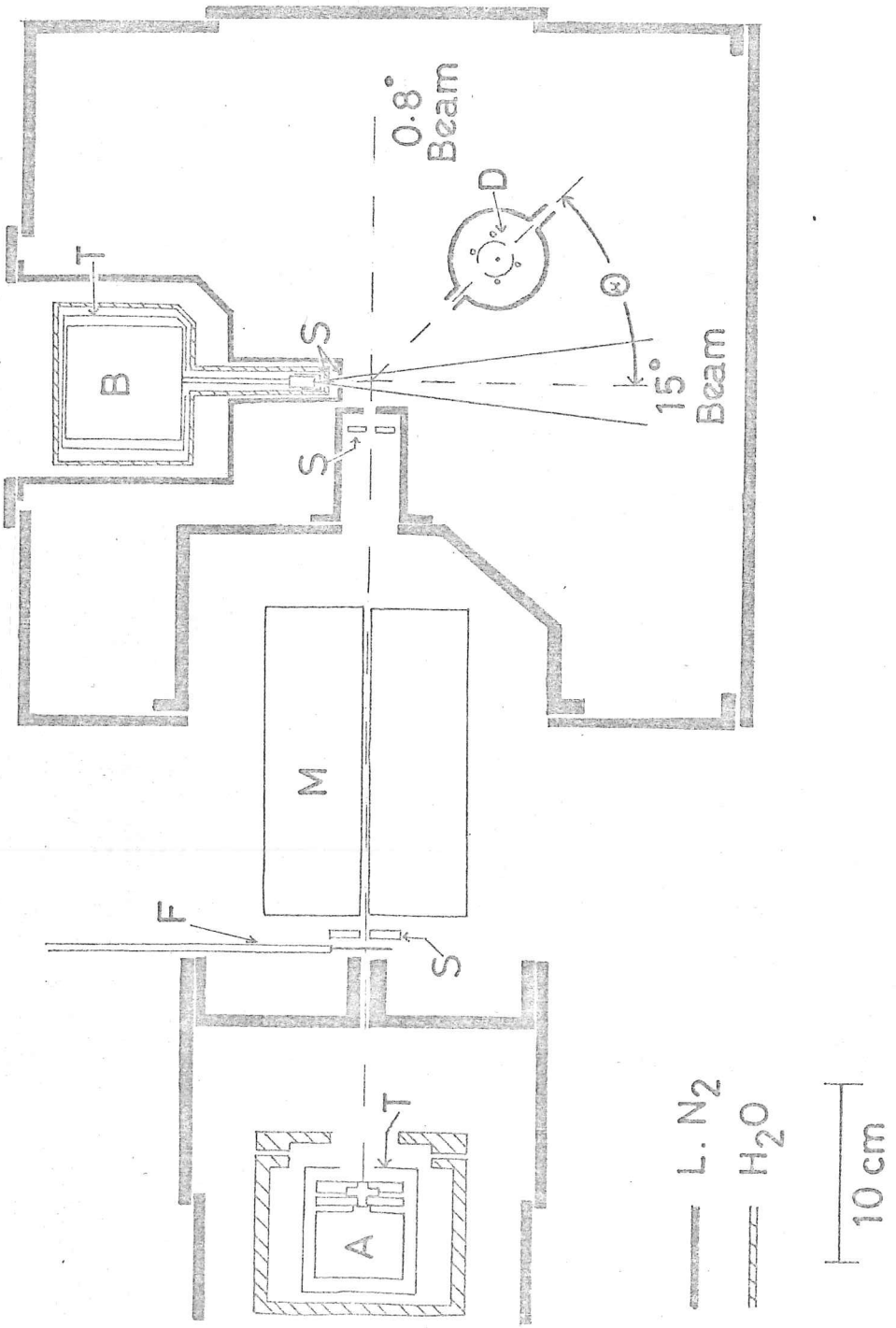

Figure 1 Plan view of apparatus, showing cold shielding.
A alkali dimer oven; B alkali atom oven; D detector;
F Beam Flag; M Magnet; S Slit; T Tantalum radiation shield.

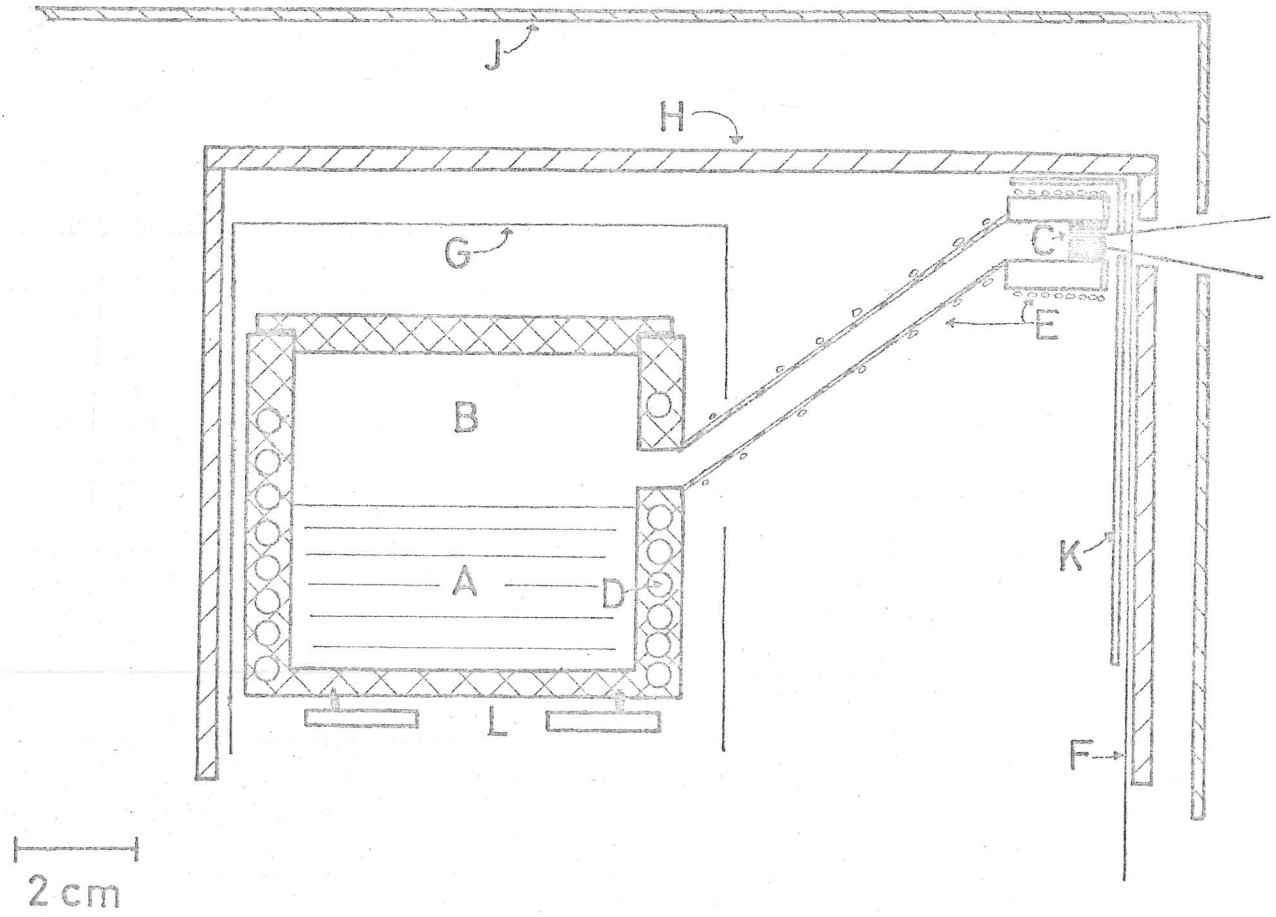

Figure 2 Alkali atom oven, vertical cross-section view. A molten alkali metal; B vaporisation region; C multi-channel "crinkle-foil"; D channels containing heater wires; E "thermocoax" heating wires; F beam flag; G tantalum radiation shield; H water-cooled copper cold shield; J liquid nitrogen-cooled copper cold shield; K heated copper collimating slit; L three pin oven mounting.

surrounded by a liquid nitrogen cooled copper cold shield which is attached to the main chamber cold shield as shown in figure 1.

The oven is filled in an atmosphere of dry nitrogen with high purity alkali metal.* The beam is initially collimated by Ni "crinkle-foil" inserted into the head to produce a multi-channel source. It then passes through a copper collimating slit heated to prevent clogging and thermally insulated from the water cold shield by P.T.F.E. and then through slits in the water and liquid nitrogen cold shields. A beam flag rotatable from outside the chamber is placed between the collimating slit and the water cold shield.

The running conditions for the alkali atom oven (and also the dimer oven) are given in table 1. The head was run ~ 100K hotter than the lower chamber to reduce the dimer concentration in the beam. Where two temperatures are quoted, data were taken for both head temperatures; in all cases these data were identical. Using the vapour pressures of alkali atoms and dimers given by Nesmeyanov (11) it is possible to estimate the dimer concentration in the beam. In all cases, even for the lowest head temperature, it is less than 0.2%.

The oven heating circuits were powered by two KTI305, 0-30V, 0-5A D.C. power supplies.† The maximum power requirements were 130 watts for the lower chamber and 80 watts for the head.

With both ovens at full working temperatures the pressure in the scattering chamber was 6×10^{-7} - 1×10^{-6} torr.

---

*Na, K. A. D. MacKay, 198 Broadway, New York 10038.
Cs, Rb. Kawecki-Billiton Ltd., Dominion Buildings, South Place, London, E.C.2.

†K.S.M. Electronics Ltd., Bradmore Green, Brookmans Park, Hatfield, Herts.

TABLE 1

Operating conditions of alkali ovens

	Dimer Oven		Atom Oven	
	T_{noz} (K)	T_{ov} (K)	T_{head} (K)	T_{body} (K)
Na	-	-	843 , 773	643
K	898	873	773 , 633	563
Rb	863	813	623	528
Cs	853	773	738 , 610	518

Detector

The detector is a surface ionisation detector followed by a quadrupole mass filter. The quadrupole mass filter type Q806* has a mass range of 0 - 150 a.m.u. and has been modified by the replacement of the electron bombardment ion source with a hot wire surface ionisation ion source. The mass filter is mounted vertically and is attached to the rotatable lid of the machine. Figure 3 shows a cross section view of the detector.

The scattered beam is ionised on a hot (1500K) 0.08mm filament of Pt - 8%W. The filament is inclined at 45° to the vertical and is mounted in a repeller cylinder which is biased positively (+ 80 volts). The alkali ions are then drawn through a four stage uniform accelerating field (zero potential to -60 volts); the entrance and exit electrodes of the accelerating field consist of a 50 gauge stainless steel mesh to prevent non-uniformity of the field. This prepares the ion beam for efficient focussing by the quadrupole lenses (12). ($V_{upper} = \pm$ 10 volts, $V_{lower} = \pm$ 15 volts). The focussed ions then enter the quadrupole mass filter. For stability the potentials for the electrodes are provided by batteries and the filament is heated by a constant current power supply Type CVCI.†

The ion optics are made from 0.5mm thick stainless steel (En58J) and are supported by four pieces of 8BA stainless steel studding surrounded by alumina insulators. The lenses are separated by alumina spacers. The electrical connections to the lenses are made by spot-

---

*Twentieth Century Electronics Ltd., King Henry's Drive, New Addington, Croydon, CR9 OBG.

†Farnell Industrial Control Ltd., Sandbeck Way, Wetherby, Yorkshire, LS22 4DH.

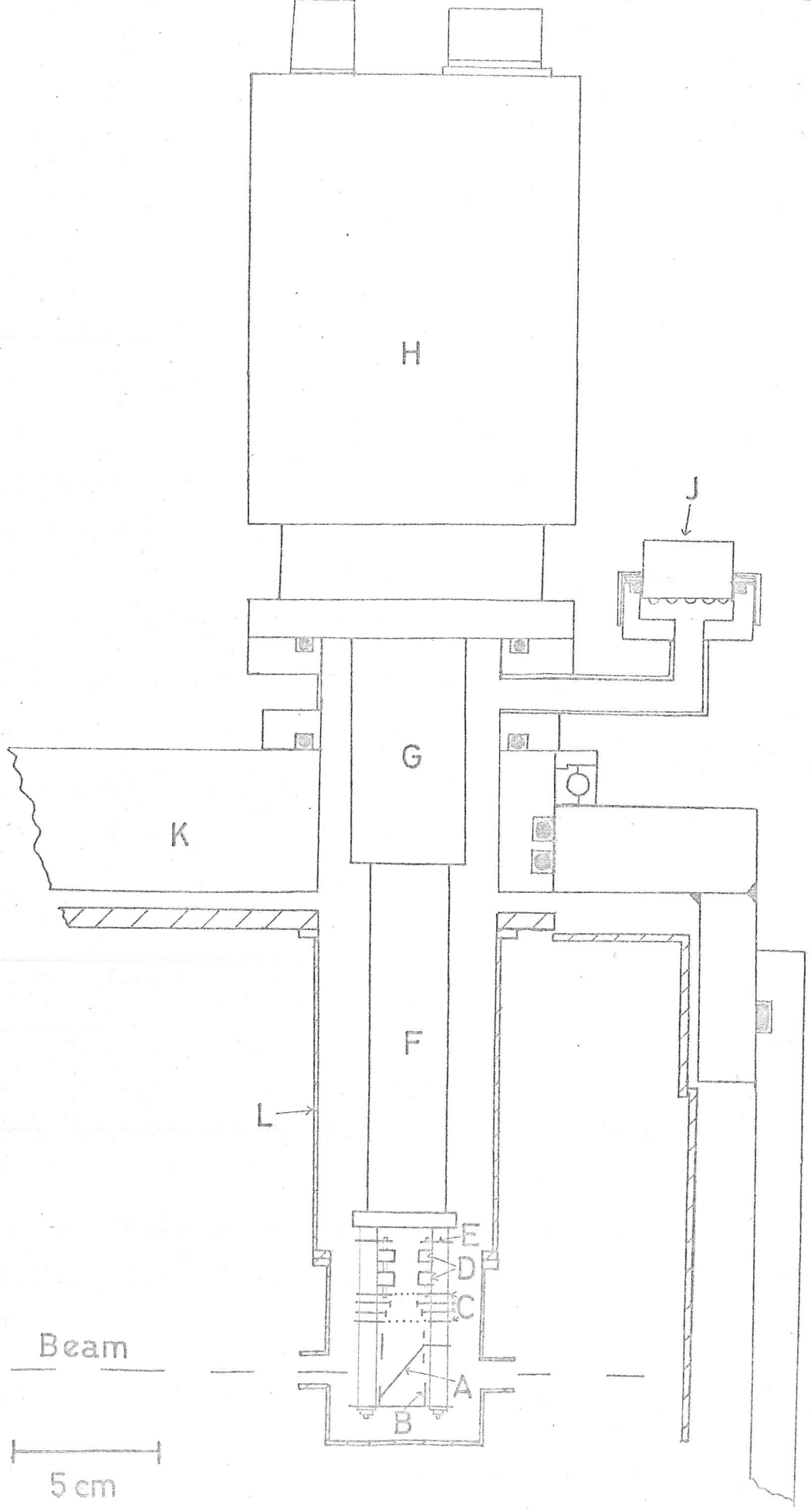

Figure 3 Cross section of machine showing quadrupole detector and cold shield. A Pt/W filament; B repeller cylinder; C accelerating field electrodes; D quadrupole lenses; E entrance electrode; F quadrupole mass filter; G electron multiplier; H R.F. oscillator; J multipin socket for leads to ion optics; K rotatable machine lid; L liquid nitrogen-cooled cold shielding.

welding 0.4 mm nichrome wire covered with P.T.F.E. sleeving.

The output from the electron multiplier of quadrupole detector is fed via a large resistor ($10^{10}\Omega$) to a vibrating capacitor electrometer. This proved to be a very low noise detection system.

Results and Kinematic Analysis

The laboratory data is shown in figure 4 for the exoergic reactions Na + K_2, Rb_2, Cs_2 and K + Rb_2 and in figure 5 for the endoergic reactions Cs, Rb + K_2 and Cs + Rb_2. The intensity (in arbitrary units) is plotted logarithmically against laboratory scattering angle Ⓗ . In each case the scattered signal is that obtained with the quadrupole mass filter being tuned to the mass of the alkali atom making up the diatomic molecule (e.g. tuned to K for Na + K_2). The reaction Na + K_2 was also run using only a Pt/W filament and an ion collector: the low ionising efficiency ($\sim 0.5\%$) of Na on a Pt/W filament (13) provides good mass discrimination. The results obtained by this method were identical with those obtained using the mass filter. The data shows pronounced asymmetry about the M_2 beam; the signal falling off more rapidly for Ⓗ $\gtrsim 90^\circ$ than for Ⓗ $< 90^\circ$. For the series of reactions Na + M_2, the scattering is broadest for K_2 and narrowest for Cs_2. For alkali atoms other than Na distributions were limited to an angular range Ⓗ $\gtrsim 60^\circ$ because of mass filter "cross-talk" due to the tail of alkali atom beam, which is ionised with near unit efficiency. The Newton diagrams constructed for the most probable velocities in the parent beams are shown in figure 6 for Na + K_2, Rb_2, Cs_2 and K + Rb_2 and in figure 7 for Cs, Rb + K_2 and Cs + Rb_2. Spheres (shown in part) about the tip of the centre of mass velocity vector c indicate accessible regions for

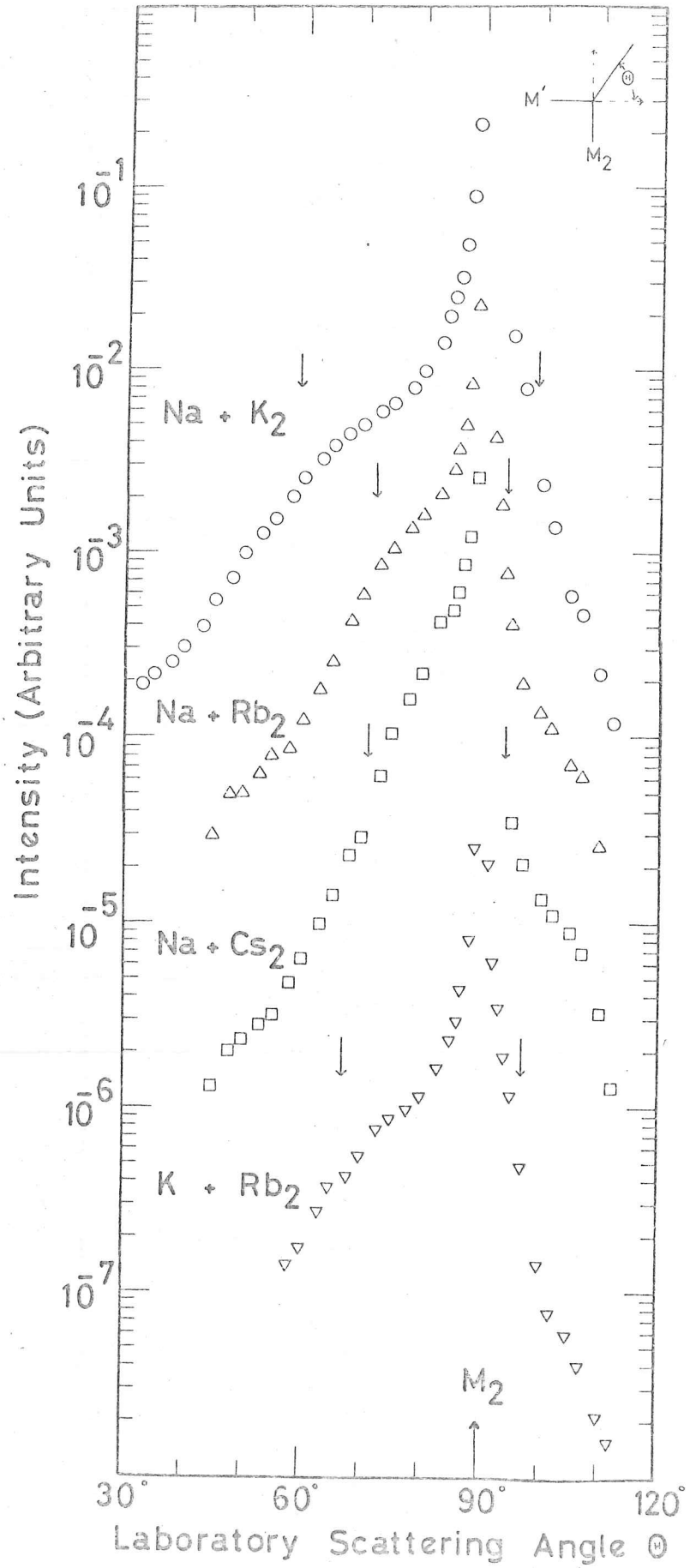

Figure 4 Laboratory angular distributions of scattering for Na + K_2, Rb_2, Cs_2 and K + Rb_2. The arrows indicate the allowed limits of elastic scattering. Successive curves are shifted down by one decade.

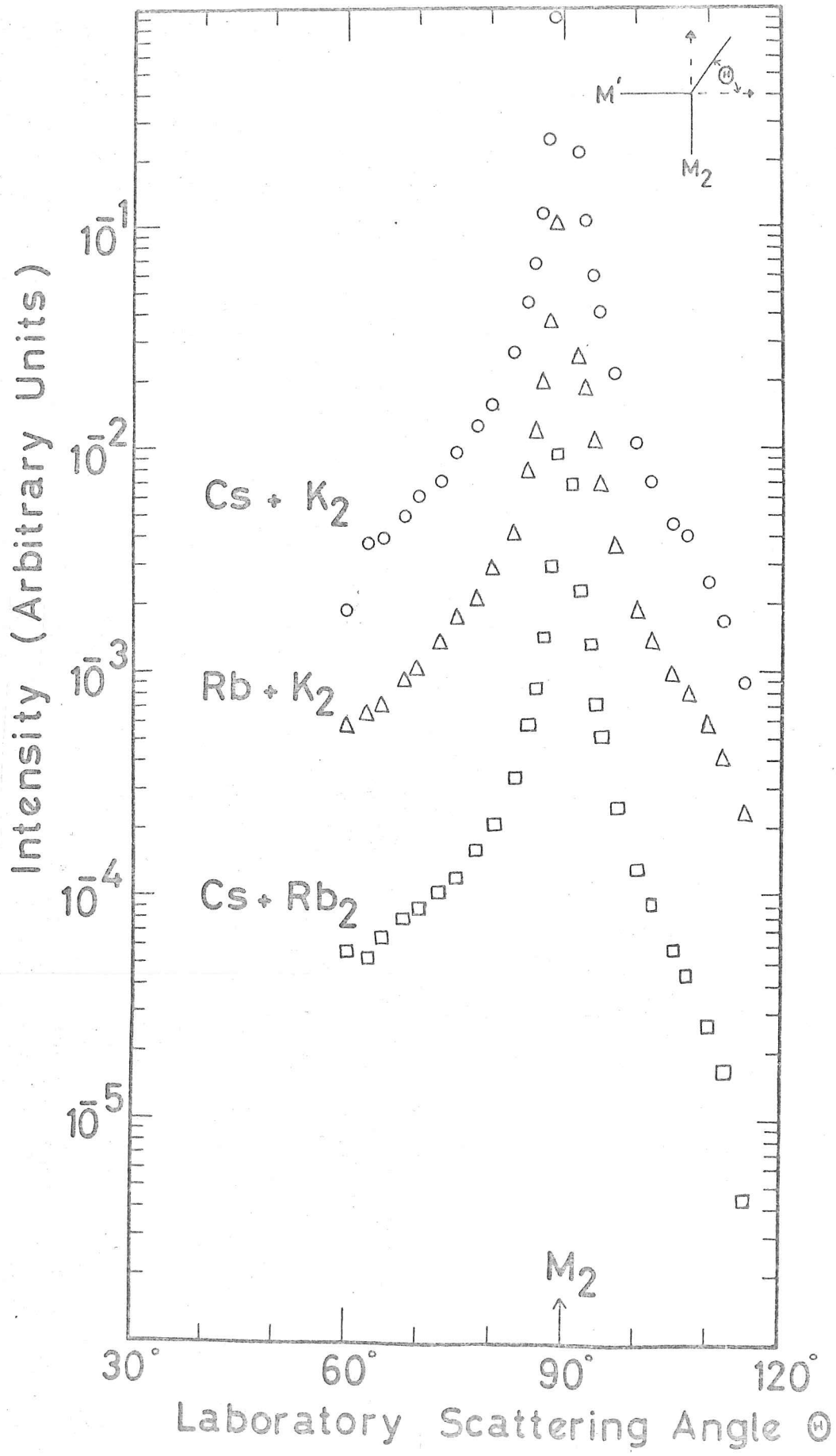

Figure 5 Laboratory angular distributions of scattering for Cs, Rb + K_2 and Cs + Rb_2. Successive curves are shifted down by one decade.

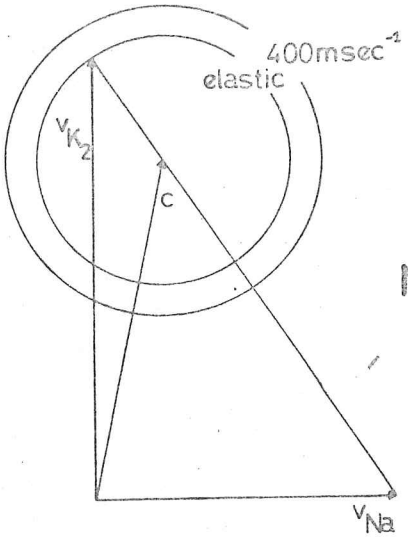

$Na + K_2$

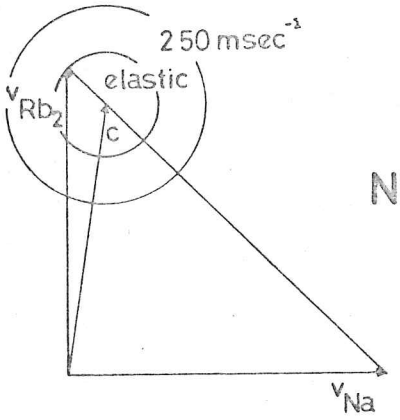

$Na + Rb_2$

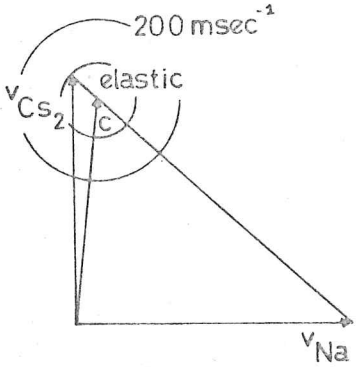

$Na + Cs_2$

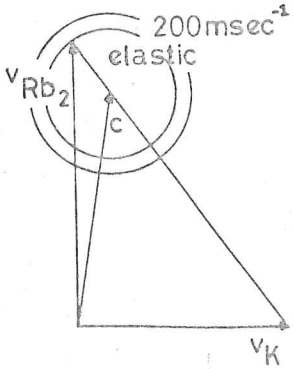

$K + Rb_2$

Figure 6 Newton diagrams for the most probable parent beam velocities for Na + K_2, Rb_2, Cs_2 and K + Rb_2.

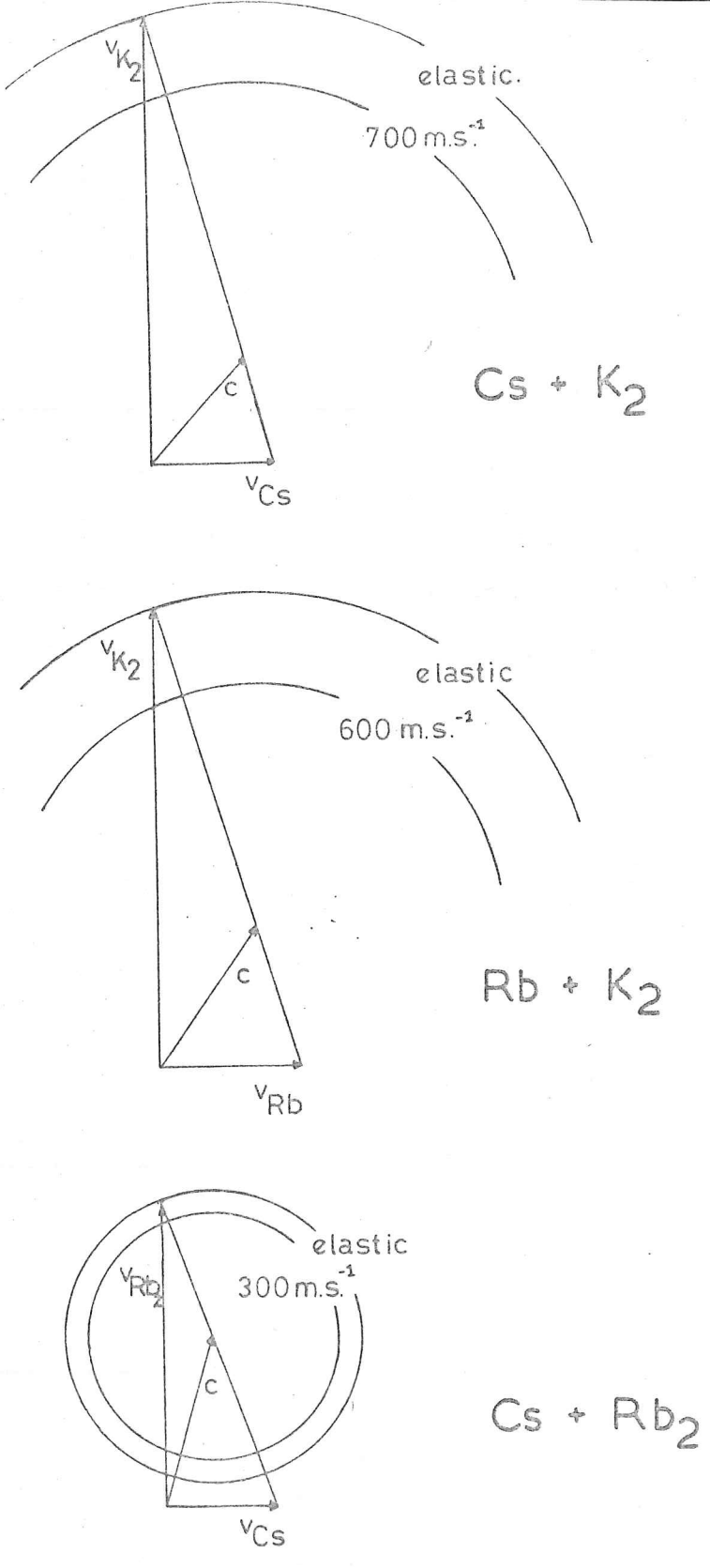

Figure 7 Newton diagrams for the most probable parent beam velocities for Cs, Rb + K_2 and Cs + Rb_2.

various recoil velocities. Figure 6 shows that for the exoergic systems the centre of mass vector lies close to the M_2 beam, confining the elastic scattering of M_2 to a narrow angular range around $\textcircled{H} = 90^\circ$. On figure 4, the limits of elastic scattering are indicated by arrows. For these reactions, then, the kinematics show that the observed scattering is not due solely to M_2 scattering as much of the observed scattering lies out with the elastic limits. For the systems Cs, Rb + K_2 and Cs + Rb_2 inspection of the Newton diagrams (figure 7) shows that all the observed scattering lies within the elastic M_2 angular range.

The scattering within the elastic limits for Na + K_2, Rb_2, Cs_2 and K + Rb_2 is transformed to the centre of mass coordinate system using the FV approximation with the elastic M_2 velocity. The intensity $I_{cm}(\Theta)$ weighted by sin Θ as a function of scattering angle Θ is shown in figure 8. ($\Theta = 0^\circ$ corresponds to the M_2 beam). The distributions are broad in shape and are not unlike those expected for a Lennard-Jones (12,6) potential (14), although comparison with the corresponding alkali atom-alkali atom systems (Chapter V) shows that they do not fall off as rapidly at small angles ($\Theta < 30^\circ$). The fact that small laboratory scattering angles correspond to quite large centre of mass angles meant that it was not possible to investigate the region ($\Theta \lesssim 10^\circ$) in which effects due to rainbow scattering might be expected. There is poor matching between the branches of the centre of mass scattering arising from laboratory scattering angles $\textcircled{H} > 90^\circ$ and $\textcircled{H} < 90^\circ$ that correspond to the same centre of mass scattering angle. This is probably due to the nature of the FV approximation which treats only the outer branch of the scattering (i.e. for a given $\textcircled{H}$ the branch with the larger laboratory velocity v). For large c.m. recoil velocities u,

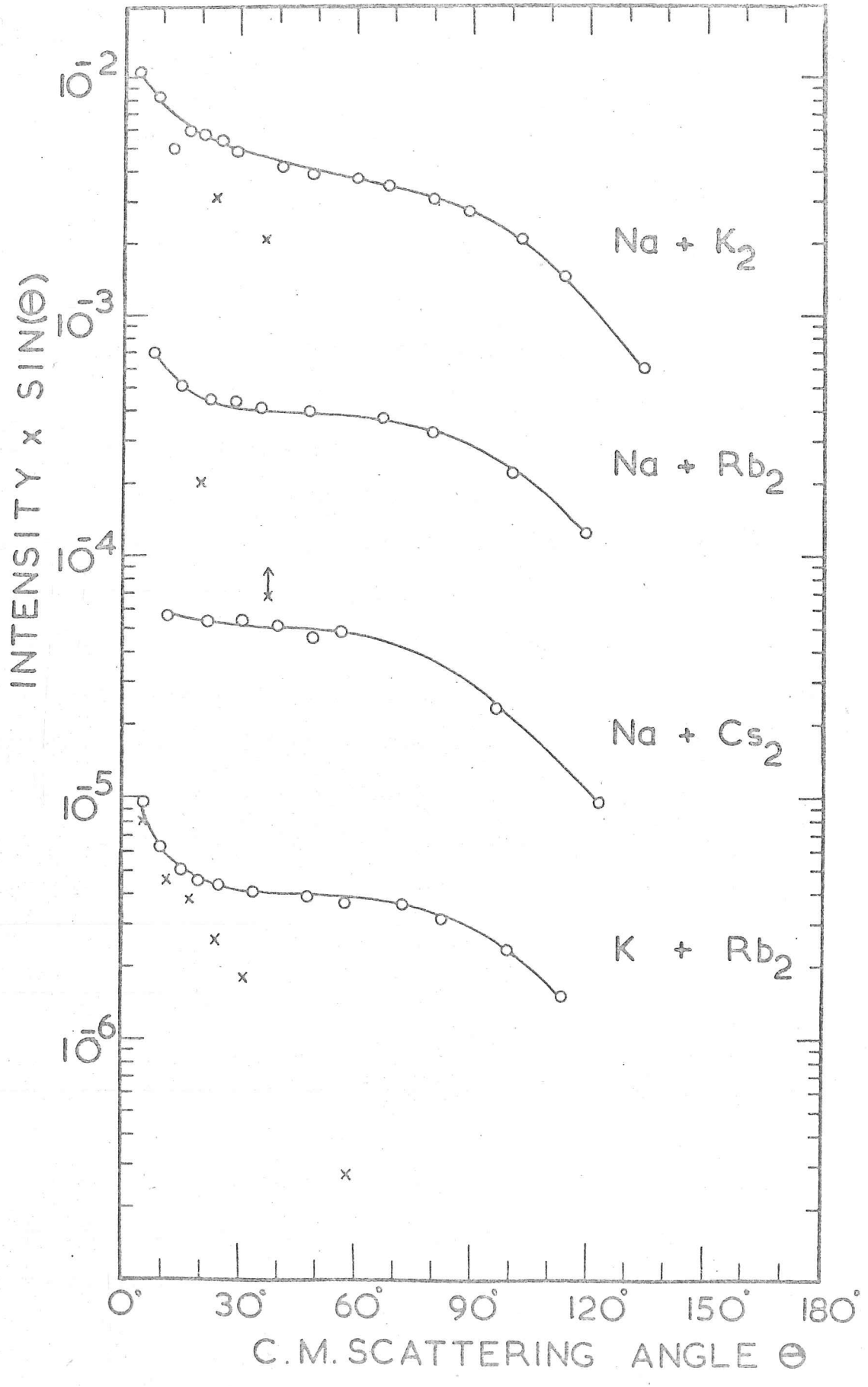

Figure 8 Centre of mass distributions of elastic scattering weighted by sin θ for Na + K_2, Rb_2, Cs_2 and K + Rb_2. Successive curves are shifted down by one decade.

the Jacobian factor makes the contribution from the inner branch insignificant, however for Na + M_2 and K + Rb_2 the elastic scattering velocity is small and both branches would be expected to contribute. It is also possible that the poor matching in part arises from the elastic M_2 scattering being enhanced at angles $\textcircled{H} < 90^{\circ}$ by reactive or inelastic scattering. Figure 9 shows the transformation of the entire observed scattering at the elastic M_2 velocity for Cs, Rb + K_2 and Cs + Rb_2. Although maxima in the elastic scattering are observed for the corresponding alkali atom-alkali atom systems (Chapter V), no such structure is observed here. As previous measurements (14,15) of elastic scattering of alkali atoms with halogen-containing molecules have shown, this could mean that reaction occurs at large impact parameters, comparable to the van der Waals radius r_m. Again, there is poor matching between the different branches of the centre of mass scattering, which could be due to reactive or inelastic scattering.

Stochastic Analysis

For the systems Na + K_2, Rb_2, Cs_2 and K + Rb_2 an attempt was made to find a centre of mass differential cross section, $I_{cm}(\Theta,u)$, which when transformed to the laboratory coordinate system would reproduce the observed scattering data (figure 4) lying outwith the allowed M_2 elastic scattering range. This procedure cannot yield a unique distribution but does serve to indicate the range of possibilities. If the masses of the reaction products MM' and M are treated as being the same, then the same $I_{cm}(\Theta,u)$ distribution can be used to describe the centre of mass scattering of either product. Conservation of linear momentum requires that the products recoil in opposite directions in the centre of mass, so the $I_{cm}(\Theta,u)$ distributions must be symmetric about $\Theta = 90^{\circ}$.

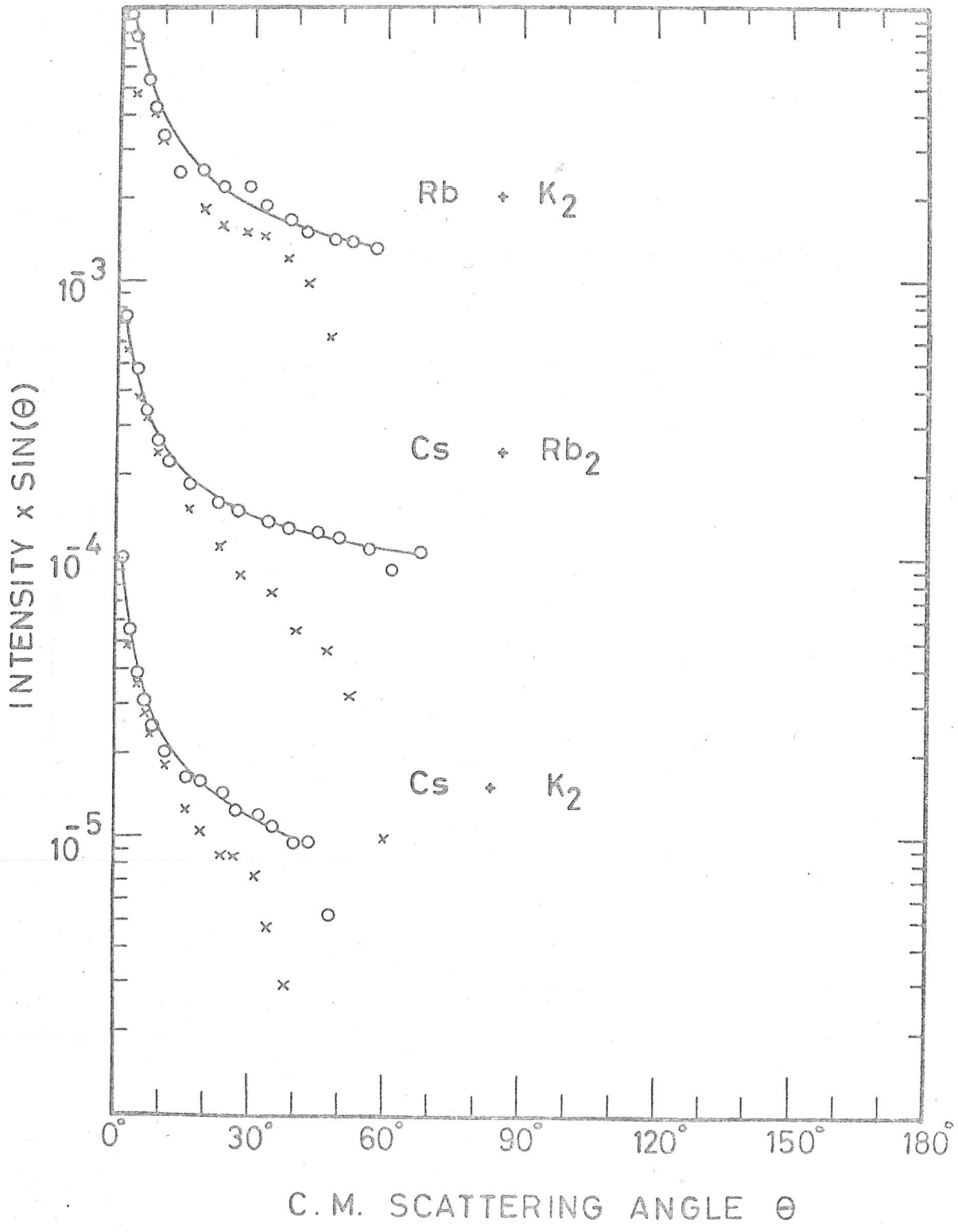

Figure 9 Centre of mass distributions of elastic scattering weighted by sin Θ for Cs, Rb + K_2 and Cs + Rb_2. Successive curves are shifted down by one decade.

A stochastic analysis procedure due to Entemann (16) was used. This assumes that the cross section is separable

$$I_{cm}(\theta,u) = T(\theta).\ U(u)\ . \qquad (1)$$

This distribution is then transformed to the laboratory coordinate system, averaging over the velocity distributions of the parent beams and the spread in their angle of intersection. The velocity distribution was assumed to be of the form

$$U(u) = (u/u^*)^3 \exp \tfrac{3}{2}\left[1 - (u/u^*)^2\right], \qquad (2)$$

a Gaussian flux distribution with u^* the most probable velocity (6). Three forms of the angular function were investigated: (i) isotropic

$$T(\theta) = 1.0 \text{ for all } \theta\ , \qquad (3)$$

(ii) a symmetric "complex" distribution with equal intensity forward ($\theta = 0^\circ$) and backward ($\theta = 180^\circ$) peaks

$$T(\theta) = \sin\theta^*/\sin\theta \quad \text{for} \quad \theta^* < \theta < 180^\circ - \theta^* \qquad (4a)$$

$$= 1.0 \quad \text{for} \quad \theta \leqslant \theta^* \text{ and } \theta \geqslant 180^\circ - \theta^* \qquad (4b)$$

and (iii) a sideways ($\theta = 90^\circ$) peaked distribution

$$T(\theta) = \exp\left[-\ln 2\ \left(\frac{\theta - 90^\circ}{H^*}\right)^2\right]\ , \qquad (5)$$

a Gaussian peaked at $\theta = 90^\circ$ with half intensity at $90^\circ \pm H^*$. The resulting transformed laboratory distributions which gave the best fits to the data are shown in figures 10, 11, 12 and 13 for $Na + K_2$, Rb_2, Cs_2 and $K + Rb_2$ respectively. Figure 14 shows the $T(\theta)$ distributions used in the stochastic analysis. Unfortunately, the predicted structure in the laboratory distributions occurs in the region where the reactive scattering is masked by the more intense M_2 elastic scattering, so no definitive $T(\theta)$ distribution can be deduced. However, there appears to be a change from a broad $T(\theta)$ distribution to one more sharply peaked in the forward and backward directions for the reactions $Na + M_2$ as M_2 changes from Cs_2 to K_2. Only for $Na + Cs_2$

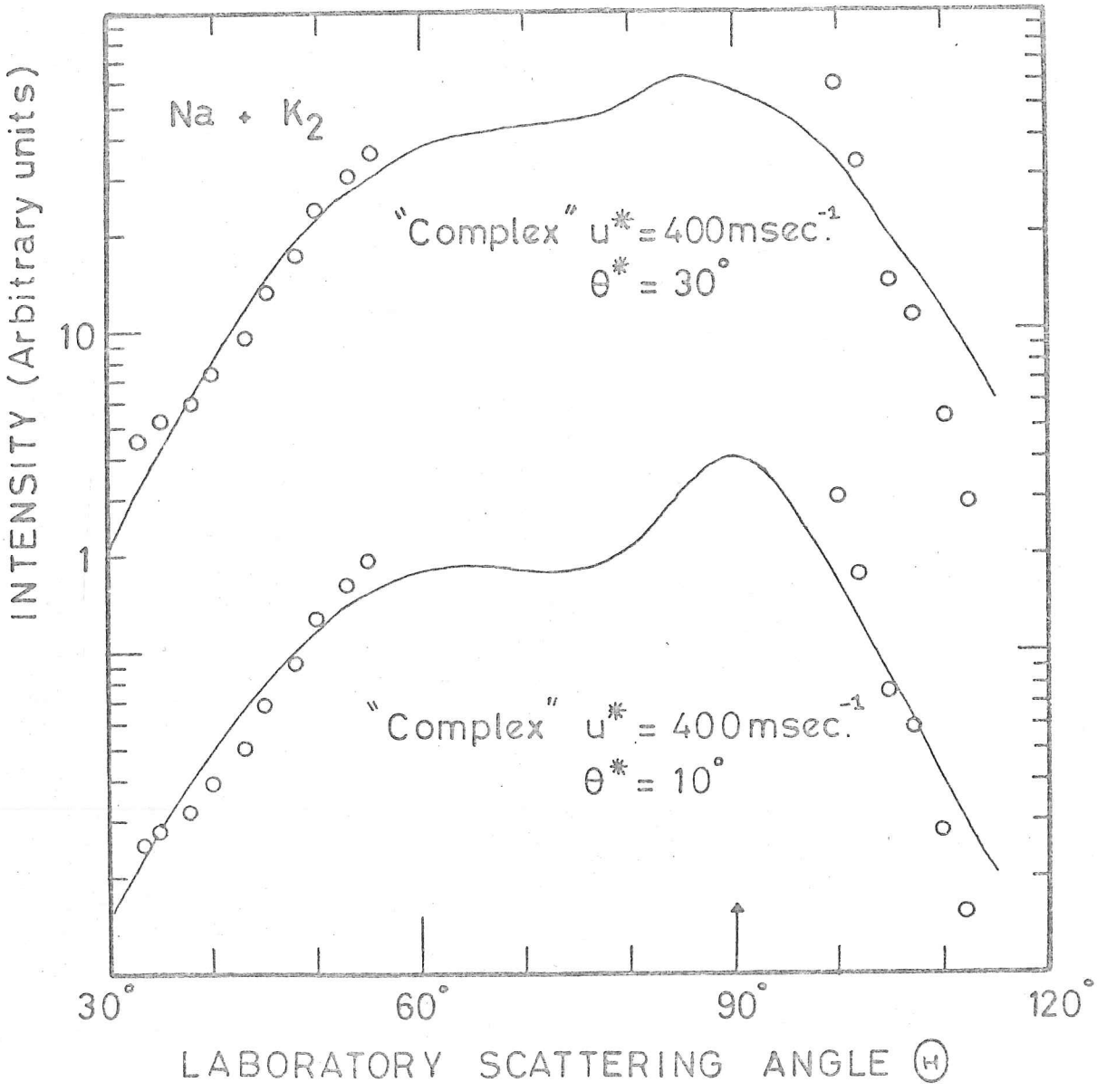

Figure 10 Laboratory distributions for Na + K_2 calculated by the stochastic analysis. Circles are the observed data.

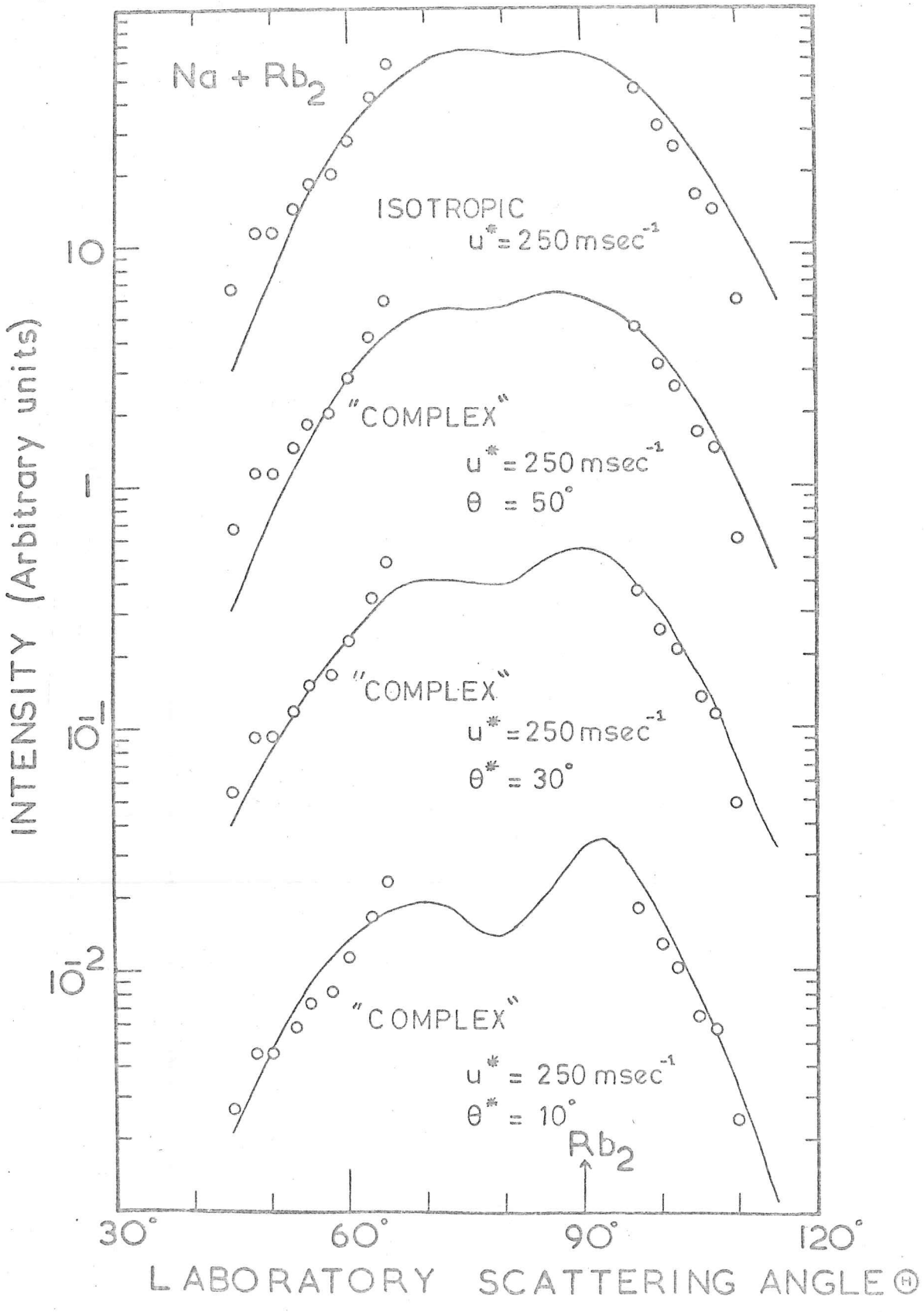

Figure 11 Laboratory distributions for Na + Rb_2 calculated by the stochastic analysis. Circles are the observed data.

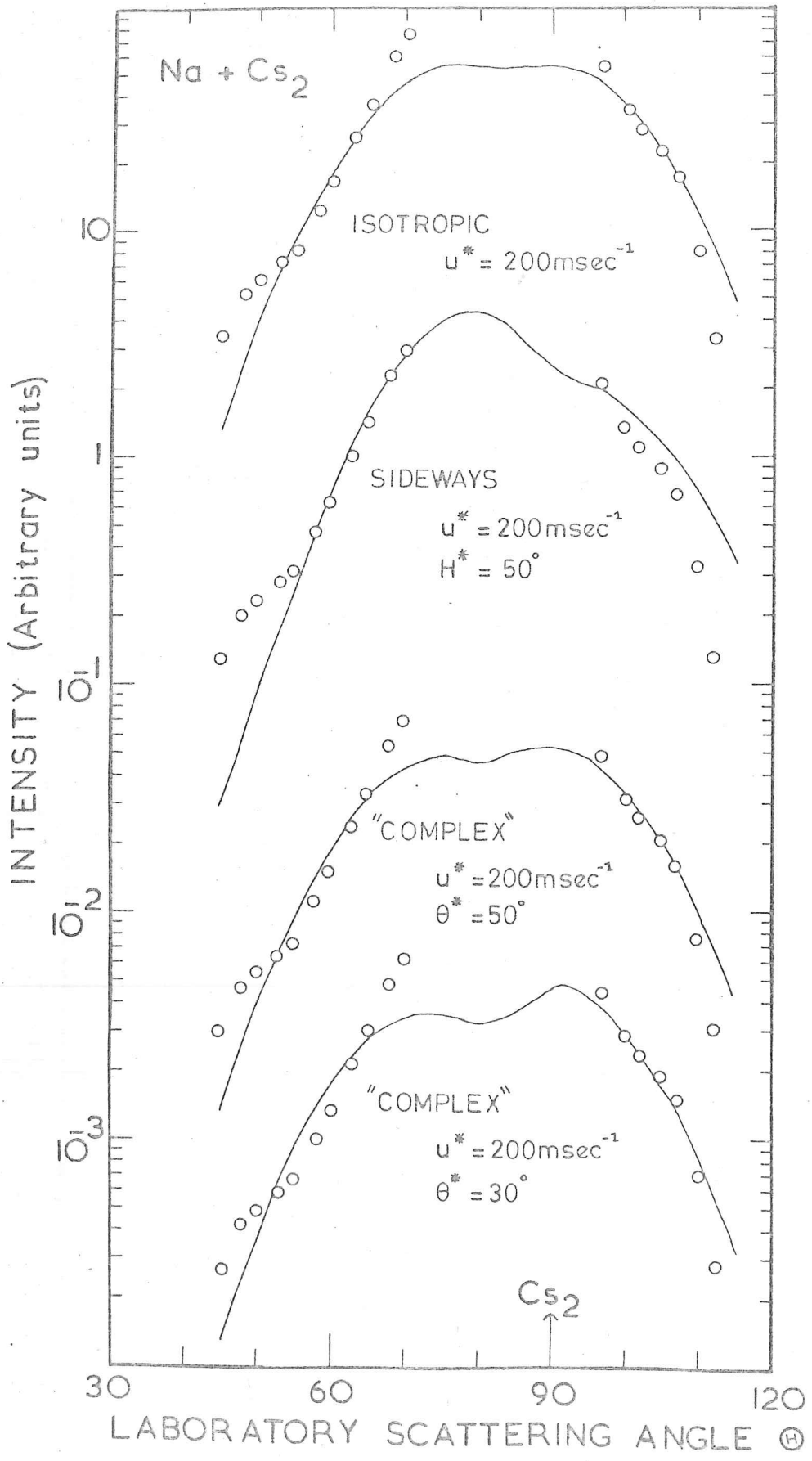

Figure 12 Laboratory distributions for Na + Cs_2 calculated by the stochastic analysis. Circles are the observed data.

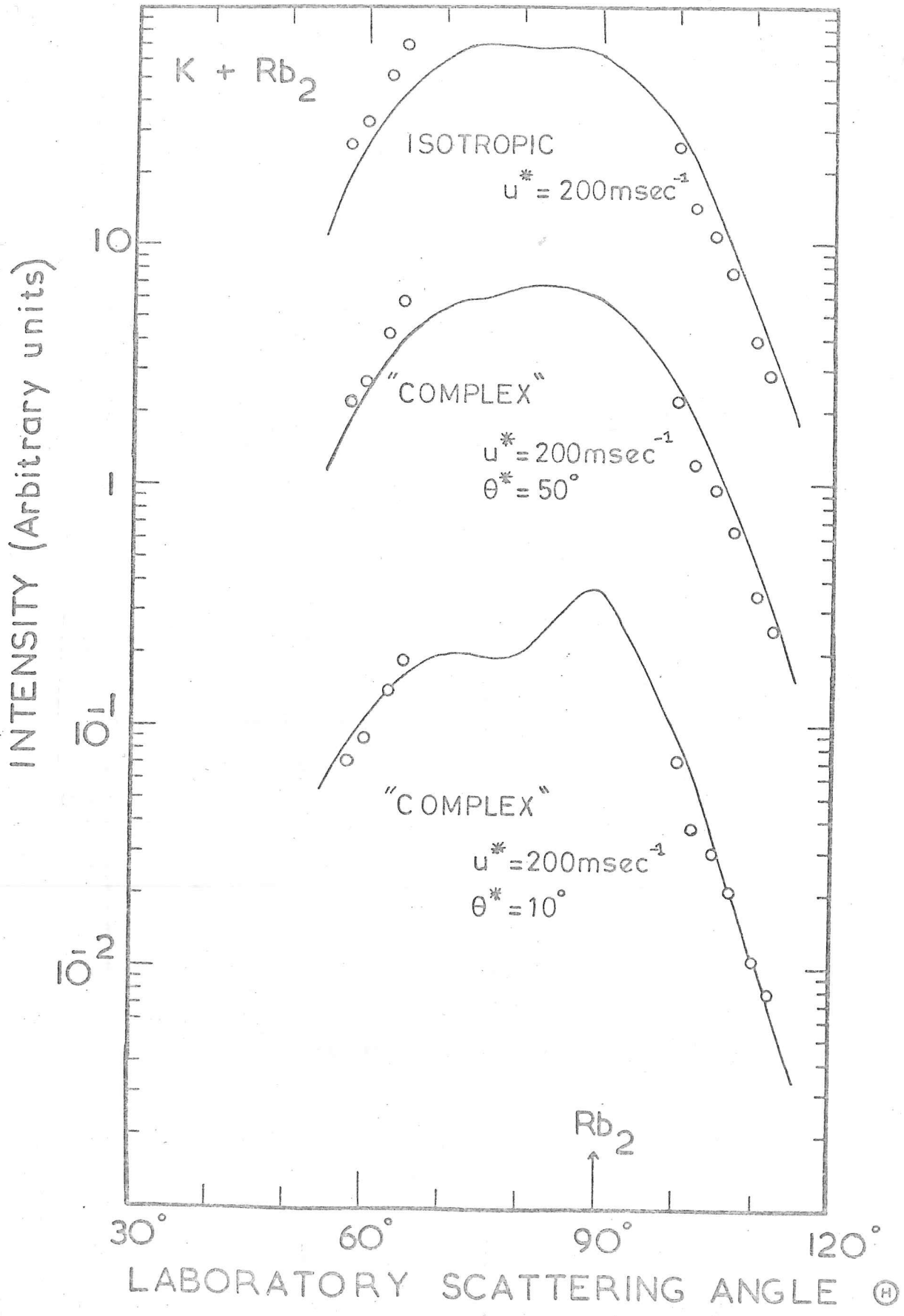

Figure 13 Laboratory distributions for K + Rb_2 calculated by the stochastic analysis. Circles are the observed data.

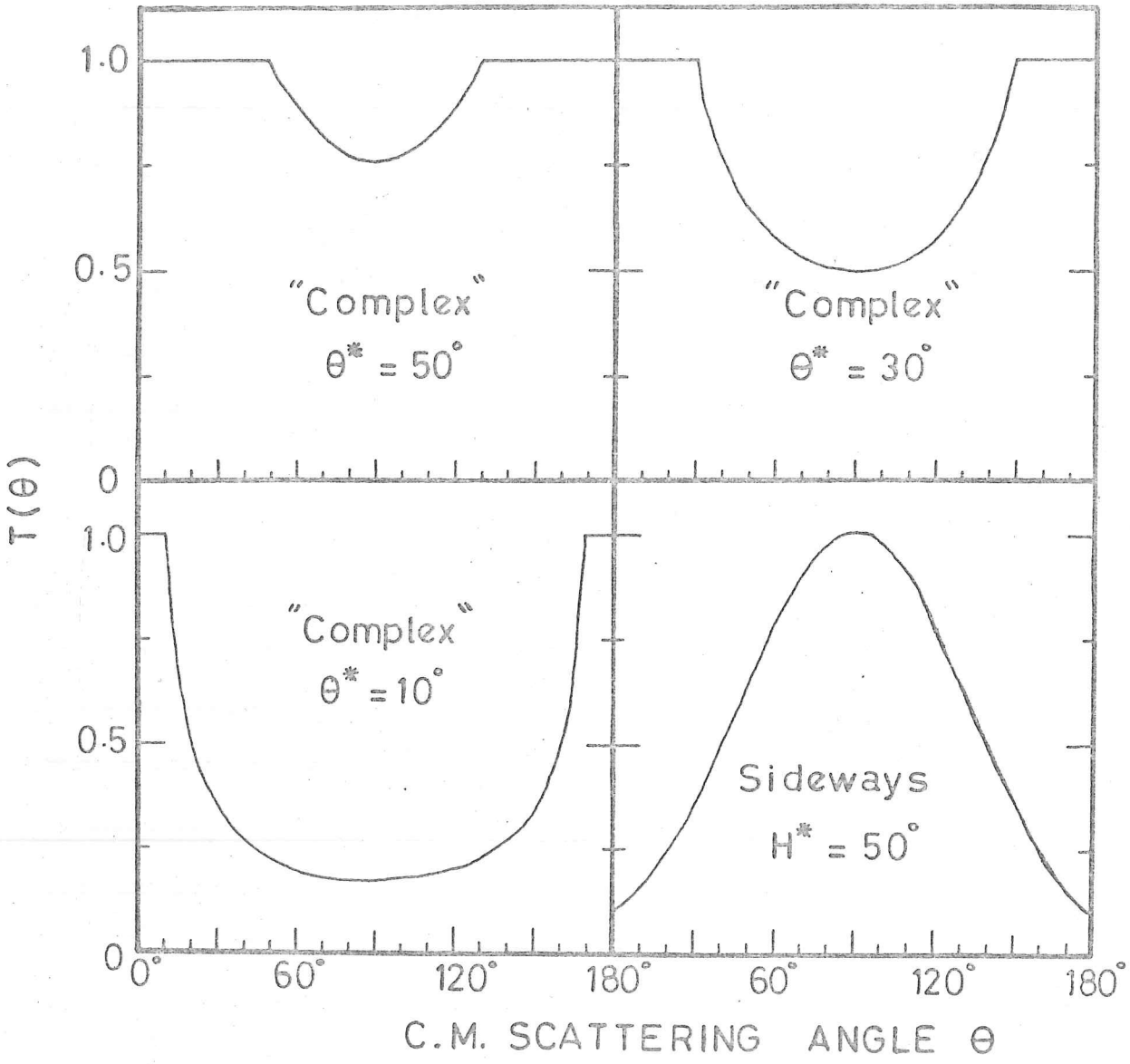

Figure 14 T(θ) functions used in the stochastic analysis of Na + K_2, Rb_2, Cs_2 and K + Rb_2.

did a sideways peaked $T(\theta)$ distribution reproduce the observed data, although not as well as the isotropic or forward-backward distributions.

For the reaction Na + K_2 the assumption of equal product masses is least valid and differences in the laboratory scattering distributions due to the identity of the products might be expected. A complete stochastic analysis using the appropriate K, KNa masses and velocities was undertaken. The centre of mass recoil velocities of the products are related by the requirement of the conservation of linear momentum

$$M_K \underline{U}_K = - M_{KNa} \underline{U}_{KNa} \quad . \qquad (6)$$

A velocity distribution $U(u)$ of the form of equation 2 was used to describe both products and the u* values were obtained from equation 6. The laboratory distributions for each product were summed and compared with the observed data. A forward and backward peaked $T(\theta)$ distribution (equation 4) for each product was investigated. In addition, a forward distribution (i.e. in the direction of the incident M' beam) for one product

$$T(\theta) = (1 - C^*) \exp\left[-\ln 2 \left(\frac{\theta}{H^*}\right)^2\right] + C^* \qquad (7)$$

combined with a backward distribution for the other product

$$T(\theta) = (1 - C^*) \exp\left[-\ln 2 \left(\frac{180^\circ - \theta}{H^*}\right)^2\right] + C^* \qquad (8)$$

was used. The best fitting laboratory distributions are shown in figure 15. As before, the predicted peaks in the laboratory distributions occur within the elastic scattering range, making it impossible to determine definitively the scattering distribution of either reaction product.

For the systems Cs, Rb + K_2 and Cs + Rb_2, there is no kinematic separation of elastic and reactive scattering, so an attempt was made to reproduce the laboratory data for $80^\circ \lesssim (H) \lesssim 100^\circ$ (which corresponds to the regions where the branches of the elastic scattering (figure 8)

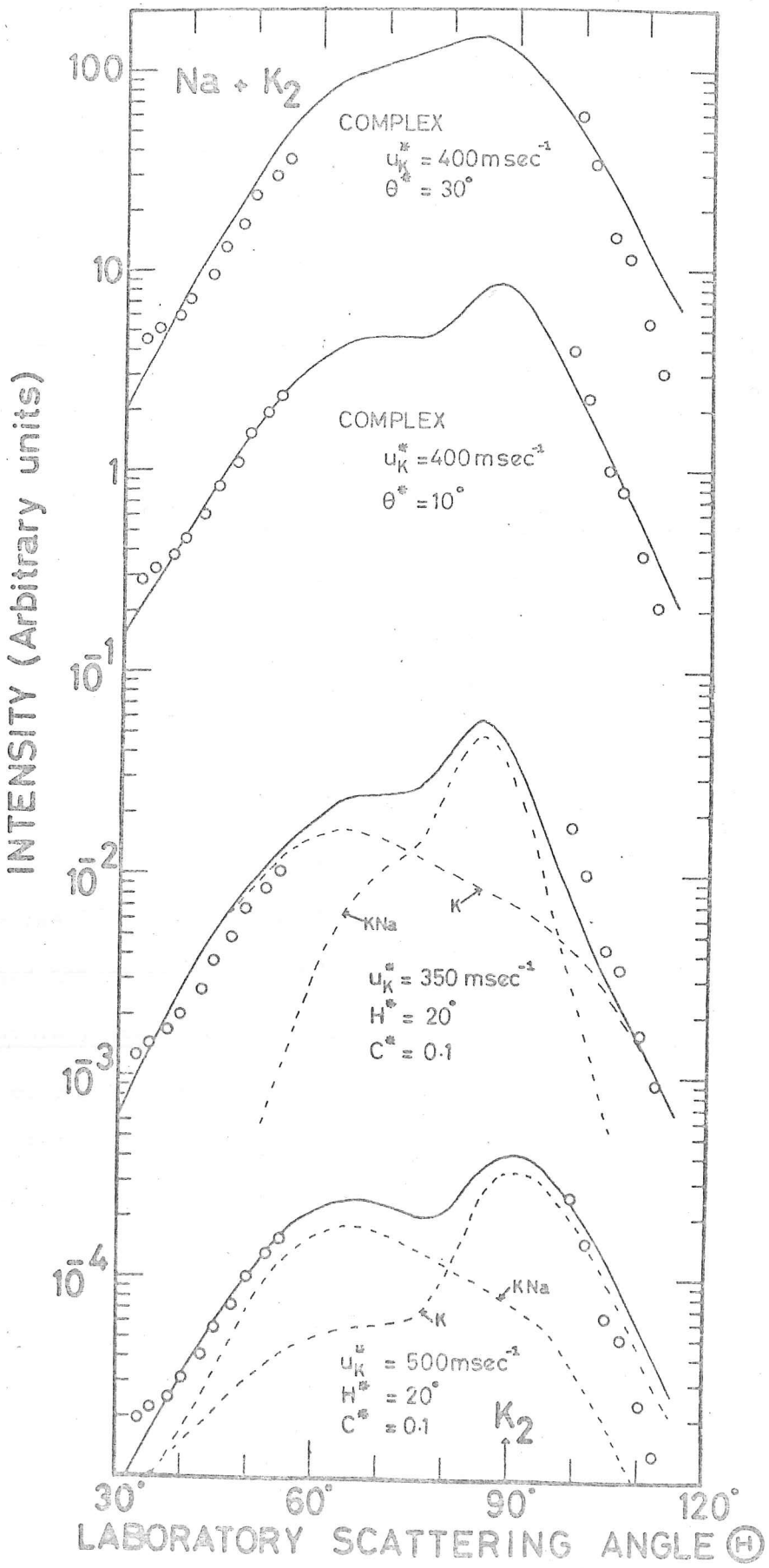

Figure 15 Laboratory distributions for Na + K_2 calculated by the stochastic analysis for reaction products K and KNa. Circles are the observed data.

diverge). It was found that the laboratory data could be best accounted for by a backward distribution of the form of equation 8. Examination of the resulting c.m. recoil velocity u* indicates that it is slightly less than the elastic M_2 velocity and would imply an inaccessibly large recoil velocity for KCs and KRb from the reactions Cs, Rb + K_2. It would then correspond to K or K_2 scattering (surface ionisation cannot distinguish between these possibilities) and is most likely to correspond to elastic K_2 scattering. These distributions are shown as solid curves in figures 16, 17 and 18 for Cs, Rb + K_2 and Cs + Rb_2, respectively. If this backward distribution is due to reactively scattered M, then conservation of linear momentum would require the MM' product to go forwards. The dashed curves (labelled "a") in figures 16 - 18 indicate the resulting combined distributions. The increased intensity for $\textcircled{H} < 90^{\circ}$ makes a matching of the laboratory data impossible in this case. Various values of u*, H* and c* were tried but no $I_{cm}(\Theta,u)$ gave a laboratory distribution to match the data. However, it is likely that most of the observed data is elastic M_2 scattering and that a distribution of reactively scattered products is "hidden" beneath the more intense elastic M_2 scattering. The possibility of a forward distribution of MM' with a backward distribution of M is shown as curve "a'" in figures 16 - 18. Similarly, a forward distribution of M and backward MM' was investigated (curve "b"). In both these cases the value of u* was determined by allowing all the initial relative kinetic energy E to appear as product recoil energy E'. Table 2 gives the value of the initial relative kinetic energies E, the initial relative velocities v, the centre of mass recoil velocities u* determined by the stochastic analysis, the recoil energies E' (calculated for a product mass M in the reactions Na + M_2 and K + M_2) and the reaction exoergicities ΔD_o. For the reactions Na + M_2 and K + Rb_2,

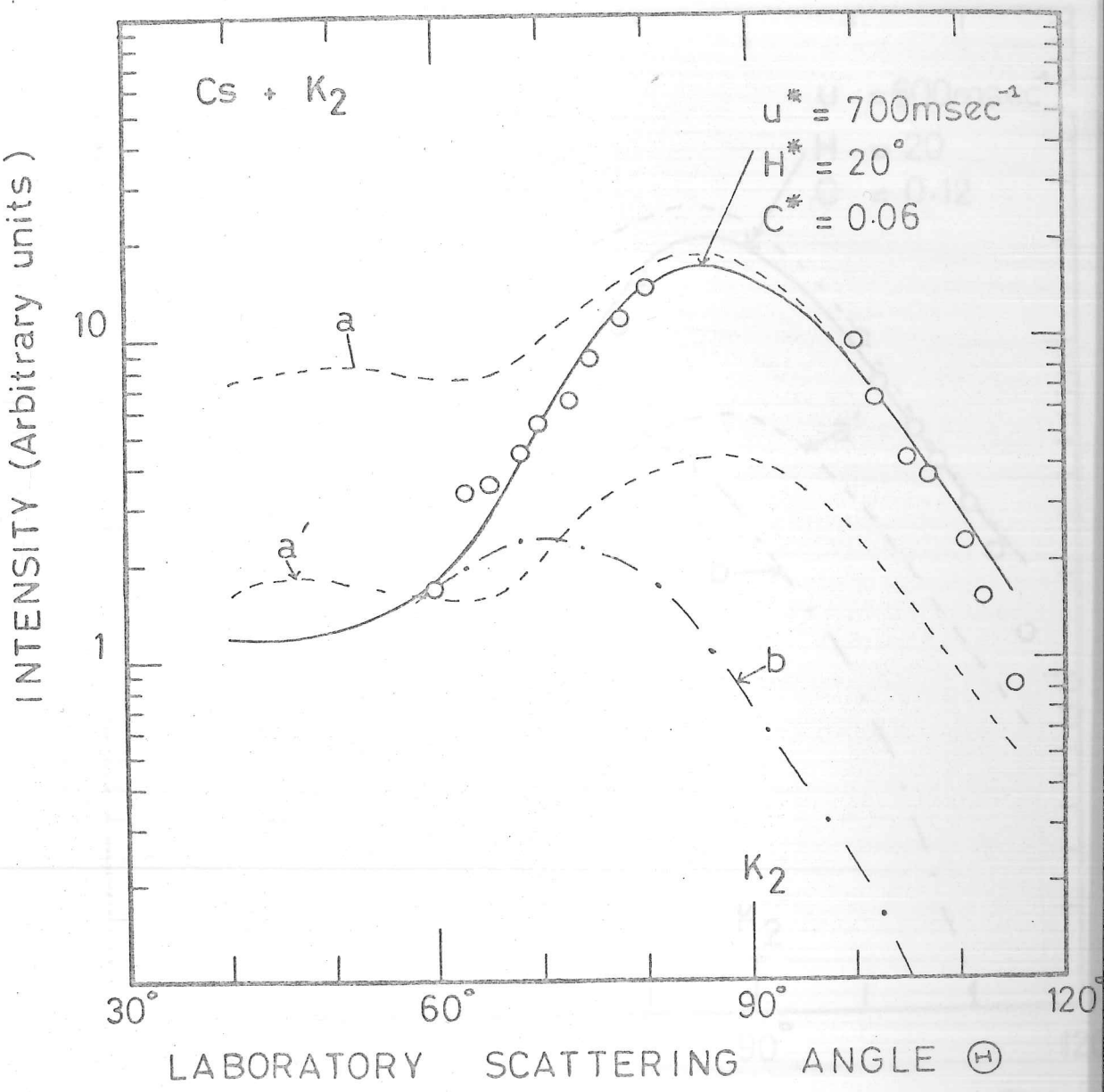

Figure 16 Laboratory distributions for Cs + K_2 calculated by the stochastic analysis. Circles are the observed data.

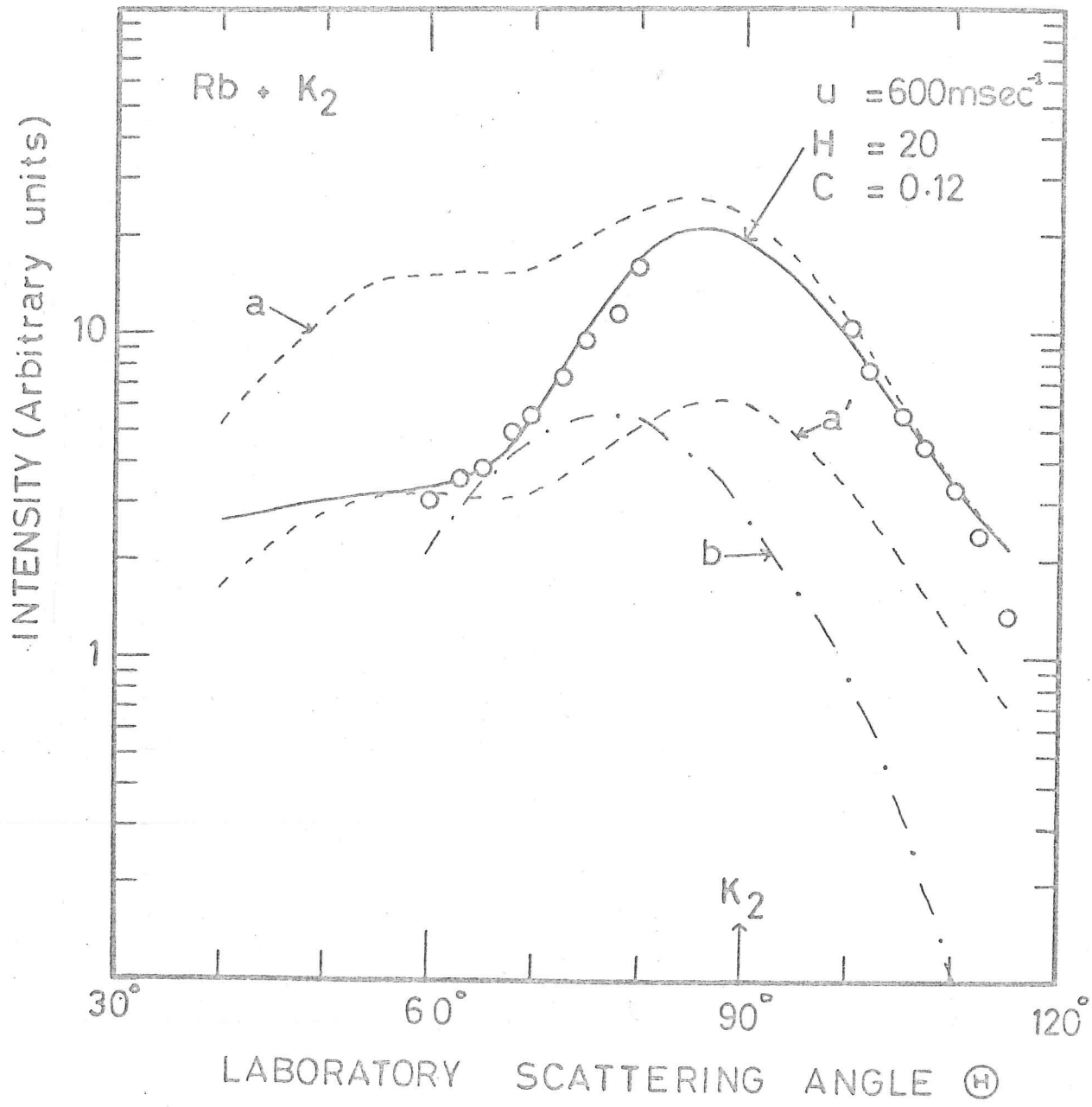

Figure 17 Laboratory distributions for Rb + K_2 calculated by the stochastic analysis. Circles are the observed data.

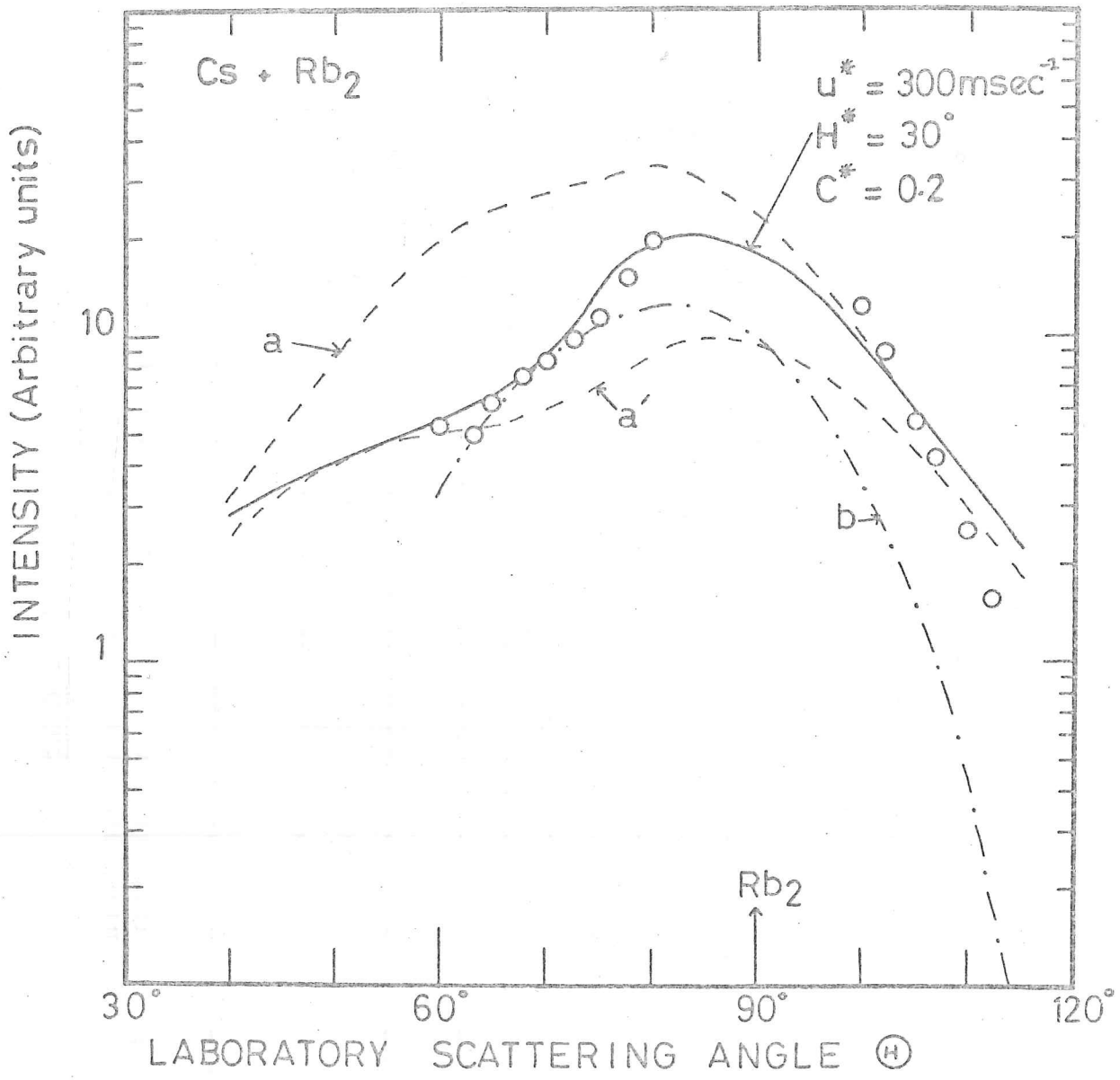

Figure 18 Laboratory distributions for Cs + Rb_2 calculated by the stochastic analysis. Circles are the observed data.

TABLE 2

Translational energies and velocities,
reaction exoergicities and total reaction cross sections

	E	V	u*	E'	ΔD_o	Q_r					
						Isotropic	Complex 50°	Complex 30°	Complex 10°	Sideways	Average
$Na + K_2$	3.93	1350	400	1.21	2.5	-	-	75	57	-	66
$Na + Rb_2$	2.90	1090	250	1.14	2.3	147	143	133	159	-	146
$Na + Cs_2$	2.10	910	200	1.17	3.0	118	116	106	-	156	124
$K + Rb_2$	3.28	930	200	0.69	0.4	124	116	78	-	-	106
$Cs + K_2$	8.19	1180	-	-	- 0.7	-	-	-	-	-	123,36
$Rb + K_2$	6.90	1190	-	-	- 0.2	-	-	-	-	-	147,46
$Cs + Rb_2$	5.98	820	-	-	- 0.5	-	-	-	-	-	198,88

Notes: a) Energy, ΔD_o kcal.mole^{-1}; velocity msec^{-1}; Q_r $\mathring{A}^2$.

b) For Cs, Rb + K_2 and Cs + Rb_2, first value of Q_r corresponds to forward MM' and backward M; second value to backward MM' and forward M.

only part of the initial kinetic energy and none of the reaction exoergicity appears as product recoil kinetic energy.

Total Reaction Cross Sections

Estimates of the total reaction cross sections were obtained from the "best fit" centre of mass differential cross sections by a method described by Entemann (16). A conversion factor n_1 is obtained from the ratio of the observed c.m. elastic scattering at $\Theta = 10^o$ to the calculated elastic scattering at the same angle in absolute units. The latter is calculated from the small angle scattering formula using the Slater-Kirkwood van der Waals coefficient and the average collision energy. Another factor n_2 is the ratio of the experimental reactive scattering intensity at a given angle to the laboratory flux at the same angle calculated from $I_{cm}(\Theta,u)$ by the stochastic analysis. The total reaction cross section is then given by

$$Q_r = n_1 n_2 2\pi \int_0^{\pi} T(\Theta) \sin\Theta d\Theta \int_0^{U_{max}} U(u)du \qquad (9)$$

where U_{max} is the largest energetically possible product recoil velocity.

Despite the seeming differences in the range of "best fits" in the case of Na + M_2 and K + Rb_2, the calculated Q_r values are in close agreement; these values and a mean Q_r for each system are presented in Table 2. These values can only be regarded as order of magnitude estimates as there is considerable uncertainty in the experimental elastic scattering and the true nature of U(u) is quite undertermined.

For the systems Cs, Rb + K_2 and Cs + Rb_2, the stochastic analysis does not provide a $T(\Theta)$ distribution for reactive scattering. However, a crude estimate of reactive scattering masked by the M_2 elastic scattering may be made for the distributions "a'" and "b" of figures 16 - 18.

The value of n_2 was obtained by normalising the peak of the calculated laboratory flux to the difference between the branches of the elastic scattering at the corresponding centre of mass angle in figure 7 when transformed back to the laboratory system. The values of Q_r are shown in Table 2 for both of distributions "a'" and "b".

Discussion

As the previous sections show, the stochastic analysis is not capable of providing definitive distributions of reaction products; indeed for the endoergic reactions it is not even possible to kinematically separate reactive scattering from elastic. Velocity analysis or magentic deflection analysis of the scattered signal is necessary to determine the product distributions. For the exoergic reactions, the total reaction cross sections are large ($\sim 100 - 140 \text{Å}^2$) and correspond to hard-sphere impact parameters of $\sim 5 - 7$ Å. At these separations the chemical bonding is small (see the previous chapter) but the van der Waals interaction contributes $\sim 0.5 - 2.0$ kcal.mole^{-1}. This is to be expected when one considers the very large polarisibilities of the alkali atoms ($\sim 20 - 50 \text{Å}^3$). For collisions subject to a $-C/r^6$ potential, there is a centrifugal barrier in the radial potential.

$$U(L,r) = -\frac{C}{r^6} + \frac{L^2}{2\mu r^2} \quad , \qquad (10)$$

where C is the van der Waals coefficient. If reaction takes place for all collisions which can clear this centrifugal barrier then the reaction cross section (17) is determined solely by the C constant and the initial kinetic energy E

$$Q_{cap} = \frac{3\pi}{2} \left(\frac{2C}{E}\right)^{1/3} \qquad (11)$$

The value of C is obtained from the Slater-Kirkwood formula using the atomic (18) and molecular polarisibilities. The molecular polarisibility

is taken to be the sum of the atomic polarisibilities (19). The values of Q_{cap} are listed in Table 3. The polarisibilities of alkali diatomic molecules together with other properties are listed in Table 4. The observed total reaction cross sections Q_r are in good agreement with those calculated above, Q_{cap}. This would seem to indicate that the reactions are governed by a long range van der Waals interaction.

For the endoergic reactions, two values of Q_r have been estimated; for a forward distribution of MM' $Q_r \sim 150 \text{Å}^2$ and for a rebound MM' distribution $Q_r \sim 50 \text{Å}^2$. However, these are values estimated without any knowledge of the angular distributions of reaction products and no significance can be attached to them. For that reason, the subsequent discussion will be confined to the exoergic reactions Na + K_2, Rb_2, Cs_2 and K + Rb_2.

The uncertainty in the angular distributions for the exoergic reactions arises from the intense elastic M_2 scattering which obscures the peaks in the reactive distributions. Even the more refined analysis for Na + K_2 is unable to resolve the scattering distribution, although in this case the assumption of equal masses for the products K and KNa is least appropriate. However the distributions appear consistent with symmetrical forward and backward peaking in M intensity (without identifying the respective distributions of the products M and MM'). This peaking is broadest for Na + Cs_2 and becomes sharper as the M_2 mass changes from Cs_2, through Rb_2 to K_2. A discussion of the angular distributions must await a detection system which can identify the scattering due to elastic M_2 and each of the reaction products MM' and M.

Although the product angular distributions are uncertain, the product recoil energies E' are known. Inspection of Table 2 shows

TABLE 3

	Q_{cap}	C	L_m	τ
$Na + K_2$	140	35.0	253	$2.1/\sqrt{}$
$Na + Rb_2$	156	37.3	246	$2.3/\sqrt{}$
$Na + Cs_2$	180	45.1	230	$2.0/\sqrt{}$
$K + Rb_2$	176	59.4	348	$3.9/\sqrt{}$
$Cs + K_2$	139	72.6	608	$3.2/\sqrt{}$
$Rb + K_2$	138	59.4	507	$3.1/\sqrt{}$
$Rb + Cs_2$	158	77.9	685	$3.7/\sqrt{}$

Note: (a) Q_{cap} $\mathring{A}^2$; C x 10^{58} erg sec^6; L_m $\hbar$

(b) L_m (the maximum orbital angular momentum) is calculated from Q_{cap}.

TABLE 4

Properties of alkali diatomic molecules.
D_e kcal.mole^{-1}, ω_e, B_e cm^{-1}, r_e Å, α Å^3.

	D_e (a)	r_e (b)	ω_e (c)	B_e (c)	α (d)
Na K	14.3±0.7		123.29		56.5
Na Rb	13.1±0.9		106.64		60
Na Cs	(13.4)		~ 98		72.5
K_2	11.8±1.2	3.923	92.64	0.05622	73
K Rb	(11.3)				76.5
K Cs	(11.1)				89
Rb_2	10.8±1.2	4.127	57.28	0.0231(e)	80
Rb Cs	(10.6)		49.41		92.5
Cs_2	10.4±0.9	4.465(e)	41.990	0.0127(e)	105

Notes: (a) D_e from A. G. Gaydon, Dissociation Energies and Spectra of Diatomic Molecules (3rd Ed., Chapman & Hall, 1968). Values in parenthesis from relation $D_{MN} = (D_{M_2} \cdot D_{N_2})^{\frac{1}{2}}$.

(b) r_e from T. L. Cottrell, Strength of Chemical Bonds (Butterworths, 1958).

(c) ω_e, B_e from G. Herzberg, Spectra of Diatomic Molecules (2nd Ed., D. Van Nostrand Company Inc., 1950).

(d) α from Ref.18 using the assumption that the diatomic polarisibility is the sum of the atomic values.

(e) W. H. Evans, R. Jacobsen, T. R. Munson and D. D. Wagman, J.Res.Nat.Bur.Stand.55, 83 (1955).

that the recoil energies are considerably less than the total available energy (initial kinetic energy, vibrational excitation of M_2 and reaction exoergicity). If the vibrational excitation of M_2 is taken to be 4 kcal.mole^{-1}(8) the total energy available to products is $\sim$ 9 kcal.mole^{-1} of which only $\lesssim$ 1 kcal.mole^{-1} appears in translation. It would appear then that these reactions provide an efficient mechanism for energy transfer to internal motion of MM'.

Table 4 shows that the alkali diatomic molecules differ only slightly in their molecular properties; in particular their dissociation energies D_e are very similar. It would be reasonable to suppose that the alkali metal exchange reactions will have similar potential energy surfaces. In the previous chapter, it was shown that for exchange reactions involving Li and Na the potential energy surfaces all show a shallow well which is not very dependent on the orientation of the $M'M_2$ molecule, but is most stable in a linear or near linear configuration. For the mixed cases the linear configuration with the lightest atom in the centre is the more stable, i.e. for $NaLi_2$ the unsymmetric Na-Li-Li is more stable than the symmetric Li-Na-Li but for $LiNa_2$ the symmetric Na-Li-Na is more stable. Our M' + M_2 systems have similar exoergicities to Li + Na_2, so we might expect a well of depth $\sim$ 6 kcal.mole^{-1} and that M-M'-M will be $\sim$ 2 kcal.mole^{-1} more stable than a M'-M-M orientation. Pickup and Byers Brown (20) predict that Na_3 and K_3 are unstable with respect to separated atom and molecule by $\sim$ 1 kcal.mole^{-1} (using their calculated D_e for Na_2 and K_2 as a comparison). Thus their surfaces have an activation energy of about 1 kcal.mole^{-1}.

The existence of a stable M_3 molecule might affect the reaction dynamics considerably; an angular distribution appropriate to a long-lived complex is anticipated if the lifetime of the intermediate is

greater than its rotational period (2). Applying the RRKM equation (17) for the lifetime τ of a species with s independent oscillators of frequency ν, with energy E and dissociation energy E_o, one obtains

$$\tau = \nu^{-1} \left[E/(E - E_o)\right]^{s-\frac{1}{2}}. \qquad (12)$$

For a well depth of about 6 kcal.mole^{-1}, the values of τ are listed in Table 3. For the reaction Na + M_2 it is small ($\sim 2/\nu$) and is only twice as large for K + Rb_2 ($\sim 4/\nu$). This means that any intermediate complex will be very short lived. This is to be expected as reaction exoergicities ($\Delta D_o \sim 2.5 - 3.0$ kcal.mole^{-1}) offset most of the well and the initial kinetic energy, ($E \sim 3$ kcal.mole^{-1}) is large enough compared with the well depth to inhibit complex formation. For K + Rb_2 the longer lifetime results from the near thermoneutral nature of the reaction. It should be borne in mind that the vibrational excitation of M_2, the reaction exoergicities and the well depth are subject to uncertainties which will affect the lifetimes considerably. It is perhaps misleading to think of the oscillators in M_2Na as having a single frequency because of the light mass of Na. Inspection of Table 4 shows that the vibrational frequencies of NaRb and NaCs are about twice those of Rb_2 and Cs_2, respectively, but for KNa and K_2 the frequencies are much the same. Thus the lifetimes in terms of the heteronuclear diatomic frequencies might be $\tau \simeq 4/\nu$ which is similar to K + Rb_2 but still very short. The shortest lived system would appear to be Na + K_2.

The observation of equal forward and backward centre of mass intensity arises from the small ratio of masses of MM' and M and conservation of linear momentum requiring MM' and M to recoil in opposite directions. It does not necessarily mean that the reaction

dynamics are those of a long-lived complex, it could equally well imply a direct mechanism and we have no way of saying which is correct. Borne and Bunker (21) have performed a Monte-Carlo trajectory study of halogen atom-molecule exchange reactions which have similar well depths to our alkali atom-molecule exchange reactions. They found that they could not reproduce the forward-backward peaking of the experimental data (4) and attribute this to their surfaces not having the correct long range interactions. They do however find that the initial and final orbital angular momentum vectors are nearly parallel, a situation that would encourage forward and backward peaking. They also find that the collision lifetimes are shorter than those found by experiment, where it is assumed that the reactions are influenced by short range interactions and their dynamics are governed by a short-lived complex with lifetime less than a rotational period ("osculating complex" model (3)). For the halogen molecules the molecular polarisibilities are much lower than for alkali diatomics (4.6, 6.2 and 9.7 $\mathring{A}^3$ for Cl_2, Br_2, I_2 respectively (22, 23)), giving cross sections, Q_{cap}, of 31 and 39 $\mathring{A}^2$ for the systems Cl + Br_2 and Br + I_2. These should be compared with the experimental estimate of $\sim$ 5 - 20 $\mathring{A}^2$, indicating that these reaction cross sections are possibly compatible with a van der Waals interaction.

Polanyi and Nomura (24) have investigated the effect of the location of a well (7 kcal.mole^{-1} deep) in either the entrance or exit valley of a thermoneutral potential energy surface, using Monte Carlo trajectory studies of A + BC $\longrightarrow$ AB + C exchange reactions with equal masses for A, B and C. They find that for low collision energies (0.5 - 2 kcal.mole^{-1}) with the hollow in the entrance valley (surface - I) reactant vibration was more effective in giving products and that for a well in the exit valley (surface - II) reactant

translation is more efficient. However these effects are not very marked. For the surface - II, the products tended to cling together causing orbiting collisions and a nearly isotropic distribution of products, with slight forward and backward peaking of both products. For the surface - I the angular distribution of products is very broad with a forward peak of AB and a backward peak of C. However the low reaction cross sections ($\sim 2\text{Å}^2$) do not make comparison with our experiments very meaningful. Also our experiments have both a high degree of initial vibrational excitation and translational energy compared with their cases.

Perhaps the closest analogy to our experiments are those of the alkali atom - alkali halide exchange reactions $M + XM' \longrightarrow MX + M'$ (2, 25). These reactions are also governed by long range interactions (dipole-induced dipole interactions) and show long-lived complex behaviour for reaction exoergicities as high as 9 kcal.mole^{-1} moderating to short-lived complexes as the reaction exoergicity becomes $\sim$ 20 kcal. mole^{-1}. Psuedo-potential calculations for KClNa (26) have shown that the surfaces have a well $\sim$ 13.5 kcal.mole^{-1} and are strongly orientation dependent, favouring a triangular complex. The long range interaction, because of the permanent dipole moment of M'X, is about twice as large as for the alkali exchange reactions and gives larger total reaction cross section ($\sim 200\text{Å}^2$). In our case, the initial kinetic energy E is about 50% of the estimated well depth, compared with $\sim$ 20% for M + XM and the vibrational excitation of M_2 is about 4 kcal.mole^{-1} compared with $\sim$ 1.6 kcal.mole^{-1} for M'X (17). As can be seen from the RRKM formula (equation 12) this will tend to reduce the lifetime of the complex. The effect of a well in the potential energy surface on the reaction dynamics, then, depends considerably on the total energy available to the molecule as compared to the well

depth and on the extent to which the reaction exoergicity removes the well with respect to the exit valley. These differences are seen mainly in the lifetime of the collision complex which can range from several rotational periods giving rise to symmetrical scattering and statistical partitioning of energy amongst the available degrees of freedom, through a lifetime comparable to the complex rotational period which gives an angular distribution of products with a large forward peak and smaller backward peak and less randomisation of energy disposal to the direct mechanism of spectator stripping.

Finally, the exchange reactions would appear to provide an efficient method of vibrational energy transfer from M_2 to MM' via the three body M_2M' intermediate. In considering the nozzle expansion of alkali atoms and the subsequent condensation to form vibrationally excited M_2 by three body recombination processes Gordon, Lee and Herschbach (27) found that the three body intermediate M_3 was less important than the three body $M + M + M \longrightarrow M_2 + M$ collision route. They also found that for one $M + M_2$ collision only $\sim$ 0.07 kcal.mole^{-1} of vibrational energy can be lost by the M_2 molecule. This would agree with our results in which the vibrational excitation of M_2 is transferred to MM' internal excitation and enhanced by the reaction exoergicity.

References

(1) D. R. Herschbach, Proceedings of the Conference on Potential Energy Surfaces in Chemistry (I.B.M. Research Laboratory, San Jose, California, 1970) p.44.

(2) W. B. Miller, S. A. Safron and D. R. Herschbach, Disc.Farad. Soc.44, 108 (1967).

(3) G. A. Fisk, J. D. McDonald and D. R. Herschbach, Disc.Farad. Soc.44, 228 (1967).

(4) Y. T. Lee, J. D. McDonald, P. R. LeBreton and D. R. Herschbach, J.Chem.Phys.49, 2447 (1968); 51, 455 (1969).
D. Beck, F. Engelke and H. J. Loesch, Ber.Bunsenges.phys.Chem. 72, 1105 (1968); 73, 921 (1969).
J. B. Cross and N. C. Blais, J.Chem.Phys.50, 4108 (1969); 52, 3580 (1970).
H. J. Loesch and D. Beck, Ber.Bunsenges.phys.Chem.75, 736 (1971).

(5) J. D. McDonald, P. R. LeBreton, Y. T. Lee and D. R. Herschbach, J.Chem.Phys.56, 769 (1972).
J. Grosser and H. Haberland, Chem.Phys.Letters 7, 442 (1970).

(6) Y. T. Lee, R. J. Gordon and D. R. Herschbach, J.Chem.Phys.54, 2410 (1971).

(7) E. J. Robbins, R. E. Leckenby and P. Willis, Adv.Phys.16, 739 (1967).
P. J. Foster, R. E. Leckenby and E. J. Robbins, J.Phys.B2, 478 (1969).

(8) P. B. Foreman, G. M. Kendall and R. Grice, Mol.Phys.23, 117 (1972)

(9) P. B. Foreman, Ph.D. Thesis (Cambridge, 1971).

(10) G. M. Kendall, Ph.D. Thesis (Cambridge, 1972).

(11) A. N. Nesmeyanov, Vapor Pressures of the Chemical Elements (Elsevier, 1963).

(12) C. F. Giese, Rev.Sci.Instr.30, 260 (1959).

(13) J. H. Birely, E. A. Entemann, R. R. Herm and K. R. Wilson, J.Chem.Phys.51, 5461 (1969).

(14) R. M. Harris and J. F. Wilson, J.Chem.Phys.54, 2088 (1971).

(15) J. R. Airey, E. F. Greene, G. P. Reck and J. Ross, J.Chem. Phys.46, 3295 (1967).
E. F. Greene, L. F. Hoffman, M. W. Lee, J. Ross and C. E. Young, J.Chem.Phys.50, 3450 (1969).

(16) E. A. Entemann, Ph.D. Thesis (Harvard, 1967).

(17) S. A. Safron, Ph.D. Thesis (Harvard, 1969).

(18) B. Bederson and E. J. Robinson, Adv.Chem.Phys.10, 1 (1966).

(19) P. J. Dagdigian, J. Graff and L. Wharton, J.Chem.Phys.55, 4980 (1971).

(20) B. J. Pickup and W. Byers Brown, Mol.Phys.23, 1189 (1972).

(21) T. B. Borne and D. R. Bunker, J.Chem.Phys.55, 4861 (1971).

(22) J. H. Birely, R. R. Herm, K. R. Wilson and D. R. Herschbach, J.Chem.Phys.47, 993 (1967).

(23) R. Grice and P. B. Empedocles, J.Chem.Phys.48, 5352 (1968).

(24) J. C. Polanyi, Proceedings of the Conference on Potential Energy Surfaces in Chemistry (I.B.M.Research Laboratory, San Jose, California, 1970) p.10.
Y. Nomura, M.Sc. Thesis (Toronto, 1971).
J. C. Polanyi, Acc.Chem.Res.5, 161, (1972).

(25) G. H. Kwei, A. B. Lees and J. A. Silver, J.Chem.Phys.55, 456 (1971).

(26) A. C. Roach and M. S. Child, Mol.Phys.14, 1 (1968).

(27) R. J. Gordon, Y. T. Lee and D. R. Herschbach, J.Chem.Phys.54, 2393 (1971).

CHAPTER V

ELASTIC SCATTERING OF ALKALI ATOM - ALKALI ATOM SYSTEMS: ANGULAR DISTRIBUTION MEASUREMENTS

Molecular beam techniques have been widely used to study intermolecular forces (1). For alkali atom - alkali atom systems most of the previous work has been concerned with the study of total elastic cross sections as a function of collision energy. Buck and Pauly (2) have studied the elastic scattering of Na, K, Rb, Cs atom - atom systems and interpreted the variation of total cross section with energy, via the Massey-Mohr approximation to yield the C_6 coefficients of the van der Waals interaction - C_6/r^6. Using higher collision energies (15 - 1000eV) glory undulations in the energy dependence of the total cross section have been analysed to give information about the singlet potentials of NaCs and LiCs (3,4). Glory undulations due to the triplet state ($^3\Sigma^-$) have been observed (5) for Li + Na, K, Rb, Cs and Na + Cs.

There have been few measurements of the angular distribution of elastic scattering for alkali atom - alkali atom systems, although this method is capable of providing as much information as total cross section measurements, particularly if angular structure can be resolved. Cowley, Fluendy and Lawley (6) have studied the very small angle scattering ($\theta \leq 2^o$) of Na and K and resolved quantum undulations, yielding information about the triplet well depth. Differential cross section measurements (7) for the scattering of both a spin-polarised and an unpolarised Na beam from an unpolarised Cs beam showed structure due to the triplet rainbow scattering.

Because of the two possible spin states of a pair of alkali atoms, two interaction potentials, the singlet and triplet, govern the cross section. These two potentials scatter independently with scattering

amplitudes $f_1(\theta)$ and $f_3(\theta)$, respectively. The total scattering is given by

$$Q(\theta) = \tfrac{1}{4}\left|f_1(\theta)\right|^2 + \tfrac{3}{4}\left|f_3(\theta)\right|^2. \qquad (1)$$

The singlet and triplet well depths are very different ($\sim$ 10 kcal.mole^{-1} for singlet and $\sim$ 0.7 kcal.mole^{-1} for triplet), so the singlet and triplet scattering characteristics occur in different energy regions.

This chapter describes the measurement of angular distributions for elastic scattering of Cs, Rb, K + Na, Rb + K, K + Cs, Rb and Rb + Cs. The apparatus used is not primarily designed for elastic scattering measurements, in particular the collision energy cannot be varied, the beams are not velocity selected (although the Laval nozzle provides a velocity resolution of 18% FWHM (8), compared with a velocity selector resolution of 15% FWHM in the work of Cowley et al (6)) and the angular resolution ($\sim 1^\circ$) is not as good as that of Beck (9) ($\sim 0.6^\circ$) or Cowley et al (6) ($\sim 0.05^\circ$).

Method

The apparatus used in these experiments was the same as that of the previous chapter, where an inhomogeneous magnetic field deflected out atoms from the beam and allowed only dimers to pass into the scattering chamber. If the magnet energizing current is switched off, a mixed beam of alkali atoms and dimers enters the chamber. At a given angle, measurements are made with the magnet off and then on, the scattering due to atoms being obtained by subtraction. As before, the scattered signal is ionised on a Pt/W filament and mass-analysed by a quadrupole mass filter.

In these experiments the laboratory scattering angle (H) is measured from the supersonic atom beam (not the thermal source as in the previous chapter).

Results

The laboratory scattering as a function of laboratory scattering angle (H) is shown in figure 1 for Cs, Rb, K + Na and Rb + K and in figure 2 for K + Cs, Rb and Rb + Cs. The scattering falls rapidly for small positive angles ($(H) \lesssim 10^{\circ}$) and then less steeply for wider angles; for negative angles, the scattering falls very rapidly. The Newton diagrams constructed from the most probable velocities in each parent beam are shown in figures 3 and 4. For the systems Cs, Rb, K + Na and Rb + K the light mass of the target molecule constrains the elastic scattering to a region around the main beam. For K + Cs, Rb and Rb + Cs the angular range for elastic scattering is not confined. The laboratory scattering data, transformed to the centre of mass coordinate system and weighted by sin Θ, is shown as a function of the centre of mass scattering angle Θ in figure 5 for Cs, Rb, K + Na and Rb + K and in figure 6 for K + Cs, Rb and Rb + Cs. For the systems Cs, Rb, K + Na the entire centre of mass scattering is observed. The scattering shows the nearly isotropic distribution characteristic of hard-sphere interactions, falling off at wide angles. Any small angle structure in the scattering that might be present is not observed as it would correspond to inaccessibly small laboratory scattering angles. For these systems, the magnitude of the centre of mass vector $\underline{c}$ is greater than that of the elastic recoil velocity $\underline{u}$, so that a given laboratory scattering angle corresponds to two centre of mass angles. In the FV approximation only the "outer branch" in the c.m. system is considered. If the ratio of c/u is not too large most of the laboratory intensity comes from the outer branch. Thus the FV transformation is most accurate for K + Na and less so for Cs + Na. For the systems K + Cs, Rb and Rb + Cs there can be seen structure due to triplet rainbow scattering at small angles ($\Theta \sim 10^{\circ}$). The data is corrected (9, 10)

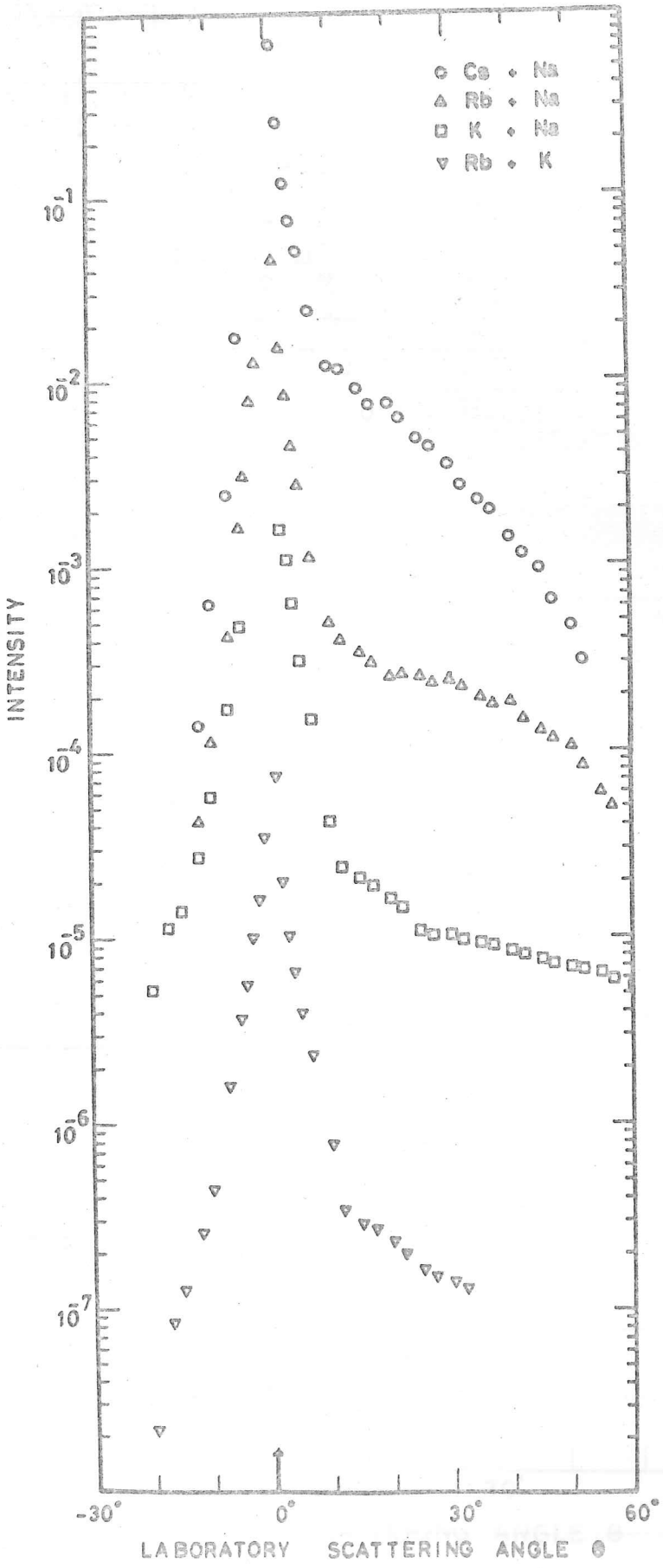

Figure 1 Laboratory angular distributions of scattering for Cs, Rb, K + Na and Rb + K. Successive curves are shifted down by one decade.

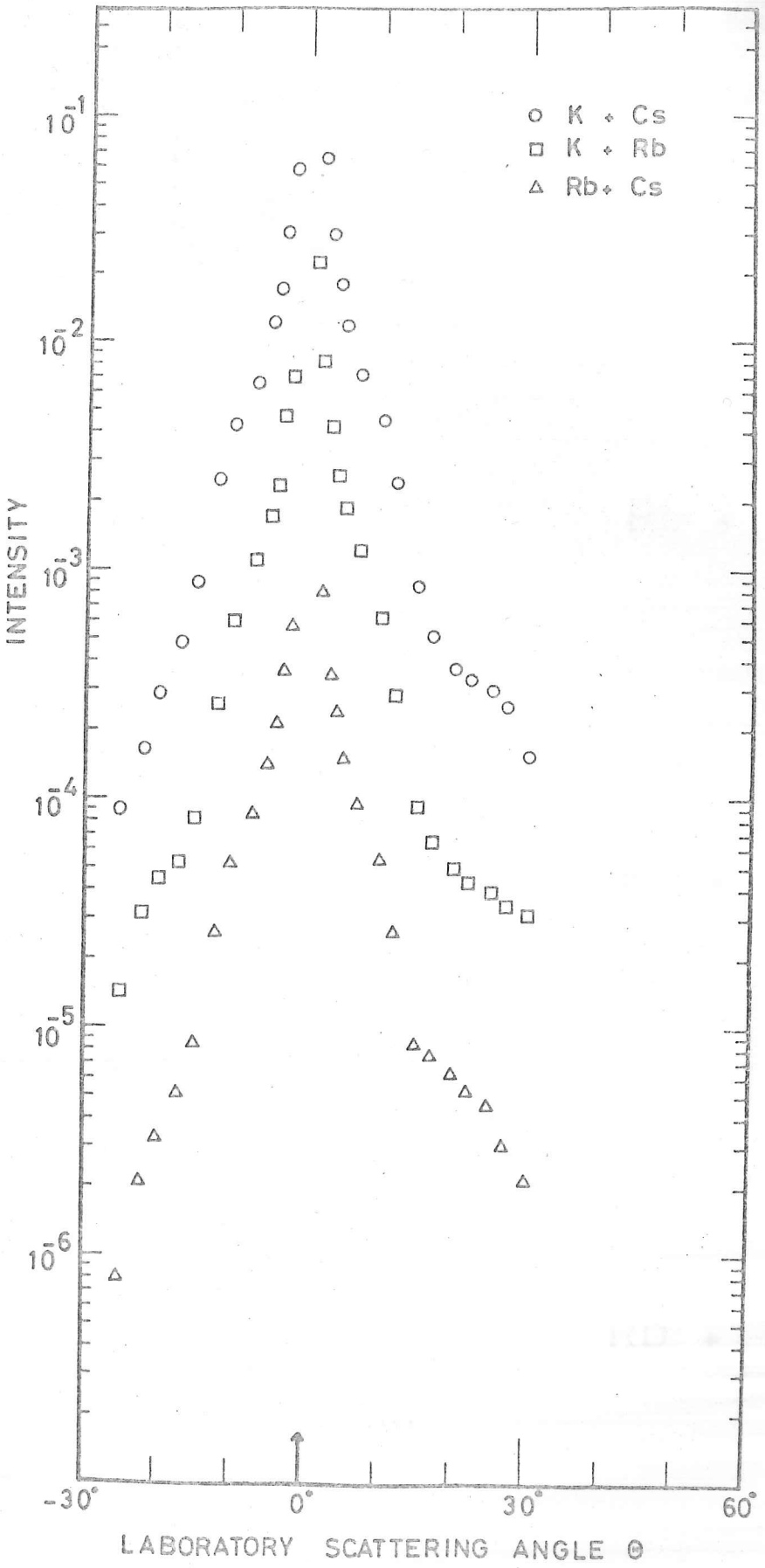

Figure 2 Laboratory angular distributions of scattering for K + Cs, Rb and Rb + Cs. Successive curves are shifted down by one decade.

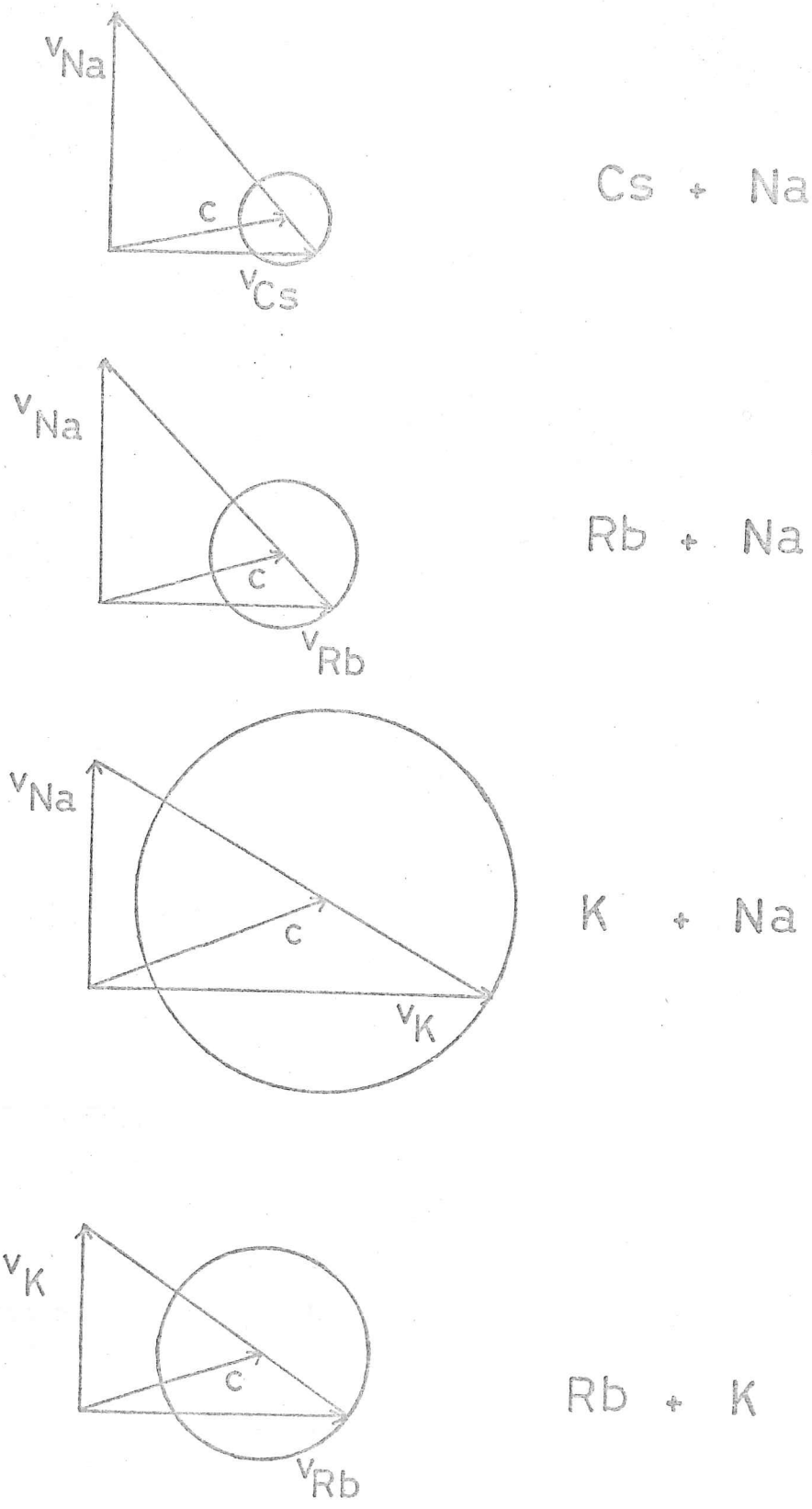

Figure 3 Newton diagrams for the most probable parent beam velocities for Cs, Rb, K + Na and Rb + K. The circles indicate the accessible regions for inplane elastic scattering

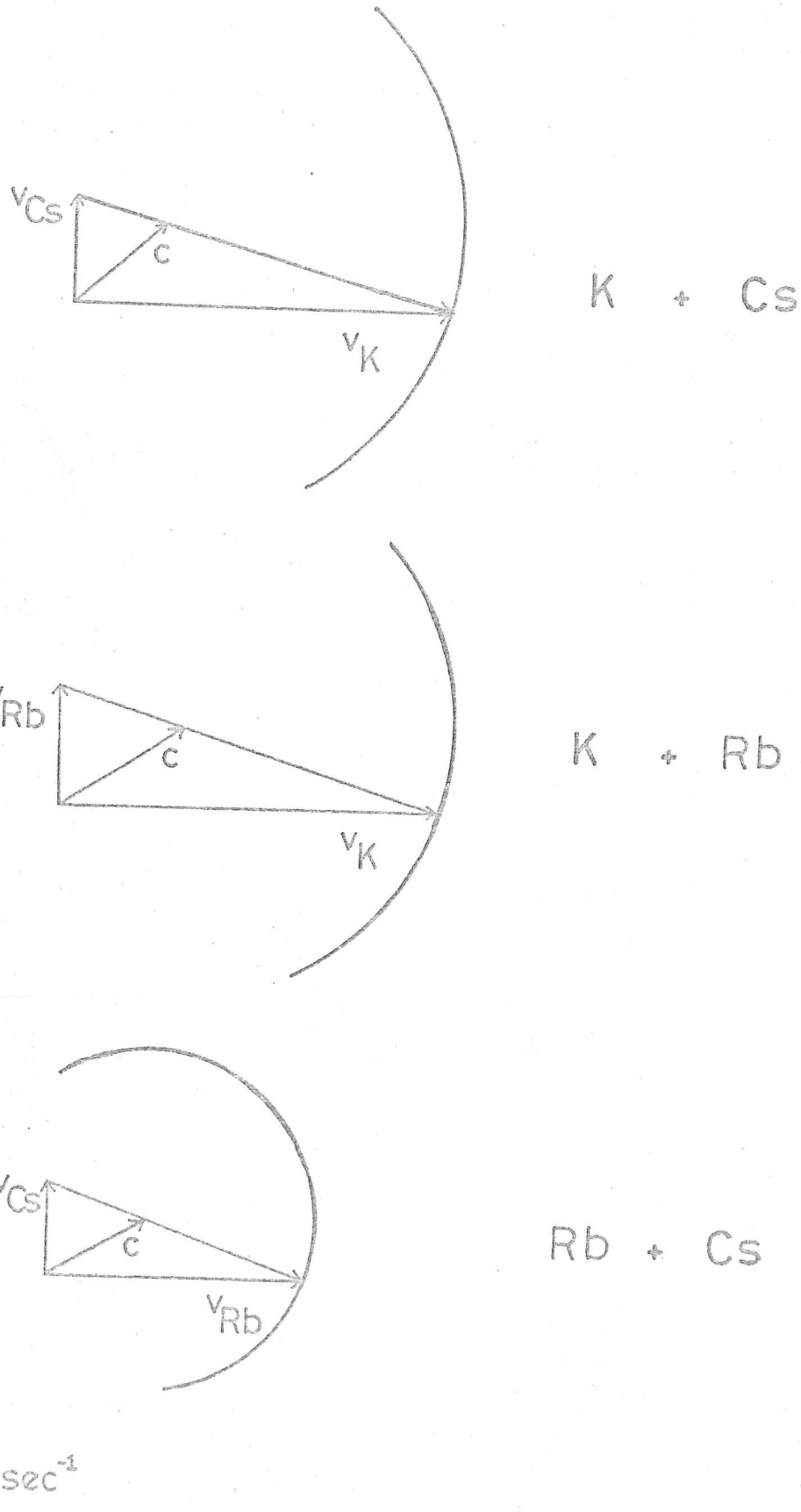

Figure 4 Newton diagrams for the most probable parent beam velocities for K + Cs, Rb and Rb + Cs. The circles (shown in part) indicate the accessible regions for inplane elastic scattering.

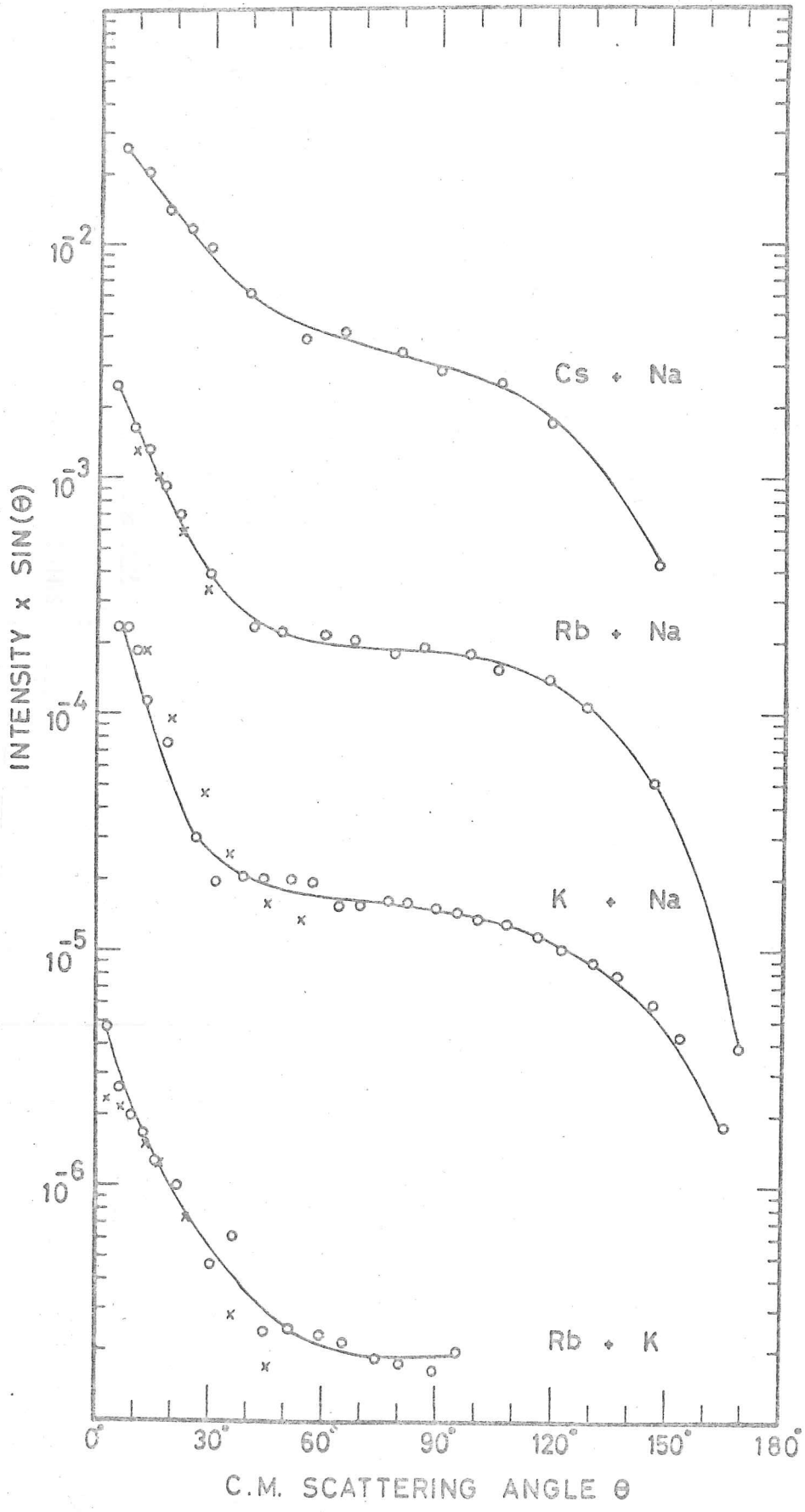

Figure 5 Angular distributions of elastic scattering in centre of mass coordinates for Cs, Rb, K + Na and K + Rb. Successive curves are shifted down by one decade, except for that for K + Rb which is shifted by two decades. Circles represent positive branch data, crosses negative branch data.

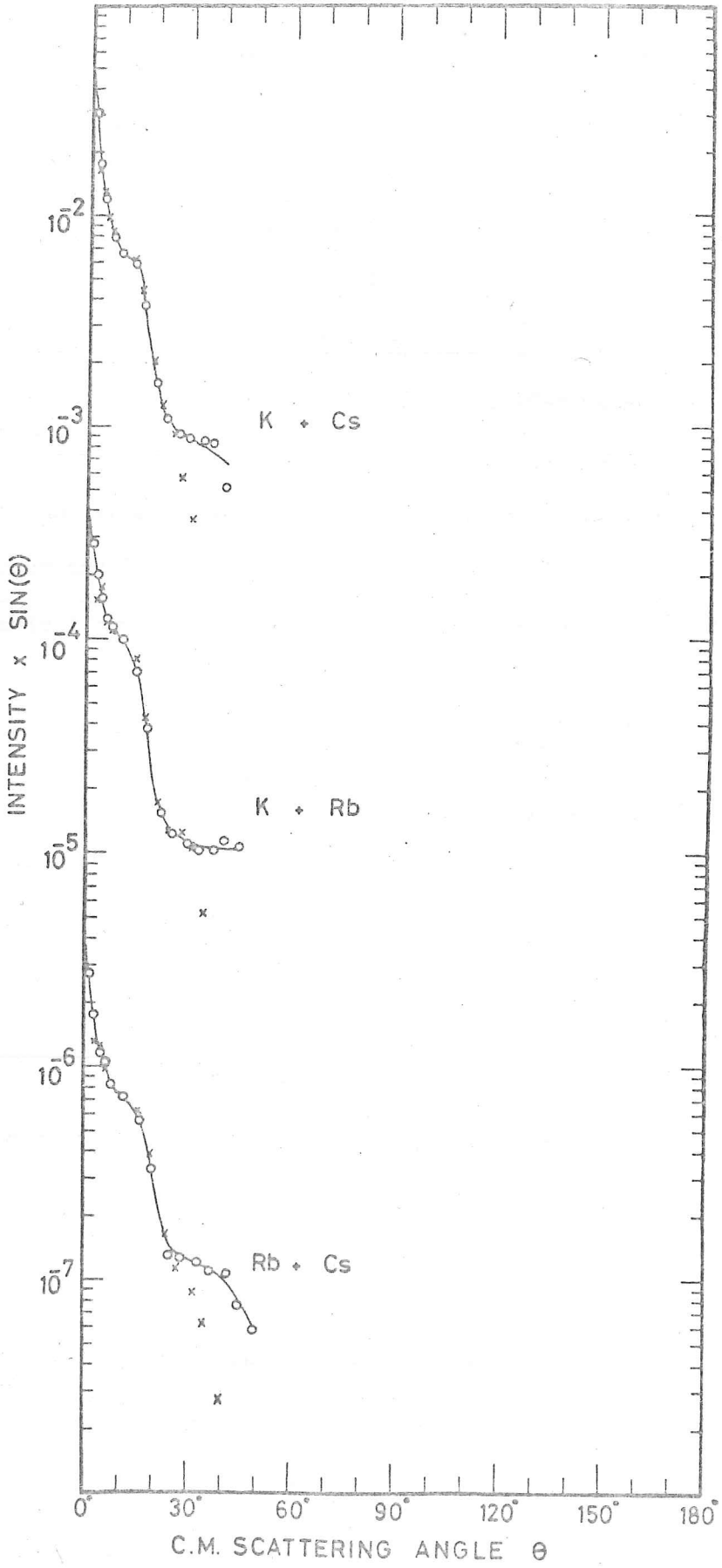

Figure 6 Angular distributions of elastic scattering in centre of mass coordinates for K + Cs, Rb and Rb + Cs. Successive curves are shifted down by two decades. Circles represent positive branch data, crosses negative branch data.

for finite detector height; the treated and untreated data are shown in figure 7. The position of the rainbow angles Θ_r and estimates of the triplet well depths ϵ were obtained using the semi-classical procedures of Beck (9, 11) for a Lennard Jones 12-6 potential. These values together with the collision energies and the experimental estimates of the coefficients C_6 for the van der Waals interaction $-C_6/r$ of Buck and Pauly (2) are listed in Table 1. Using the C_6 value in Table 1 and the relation for a Lennard-Jones 12-6 potential

$$2\epsilon\, r_m^6 = C_6 \qquad (2)$$

it is possible to determine the positions of the van der Waals minima, r_m. The values are in Table 1. For NaCs, Pritchard et al (7) found $\epsilon = 4.2 \times 10^{-14}$ ergs at $r_m = 4.5\text{Å}$ from rainbow scattering analysis. Cowley et al (6) deduced a value of $\epsilon = 2 \times 10^{-14}$ ergs at $r_m = 5.6\text{Å}$ for NaK.

In our measurements, the rainbow is most clearly resolved for KCs and less clearly for KRb and RbCs. Based on the uncertainty in the position of Θ_r, we estimate the error in our values of ϵ to be about $\pm$ 10%.

Discussion

For KCs, KRb and RbCs the observed positions of the rainbow angles Θ_r agree well with the predicted positions tabulated by Hundhausen and Pauly (12) for the calculated values of ϵ and r_m. At the triplet maximum, $f_3(\Theta) \gg f_1(\Theta)$ (7) so that any effects due to scattering from the singlet potential are expected to be negligible. For the collision energies of these experiments ($E \sim 5$ kcal.mole^{-1}) and the singlet well depths of alkali diatomic molecules (~ 10 kcal.mole^{-1}), the rainbow angle due to the singlet potential will be at $\Theta_r \gtrsim 60^\circ$.

The results of this chapter allow interesting comparison with the

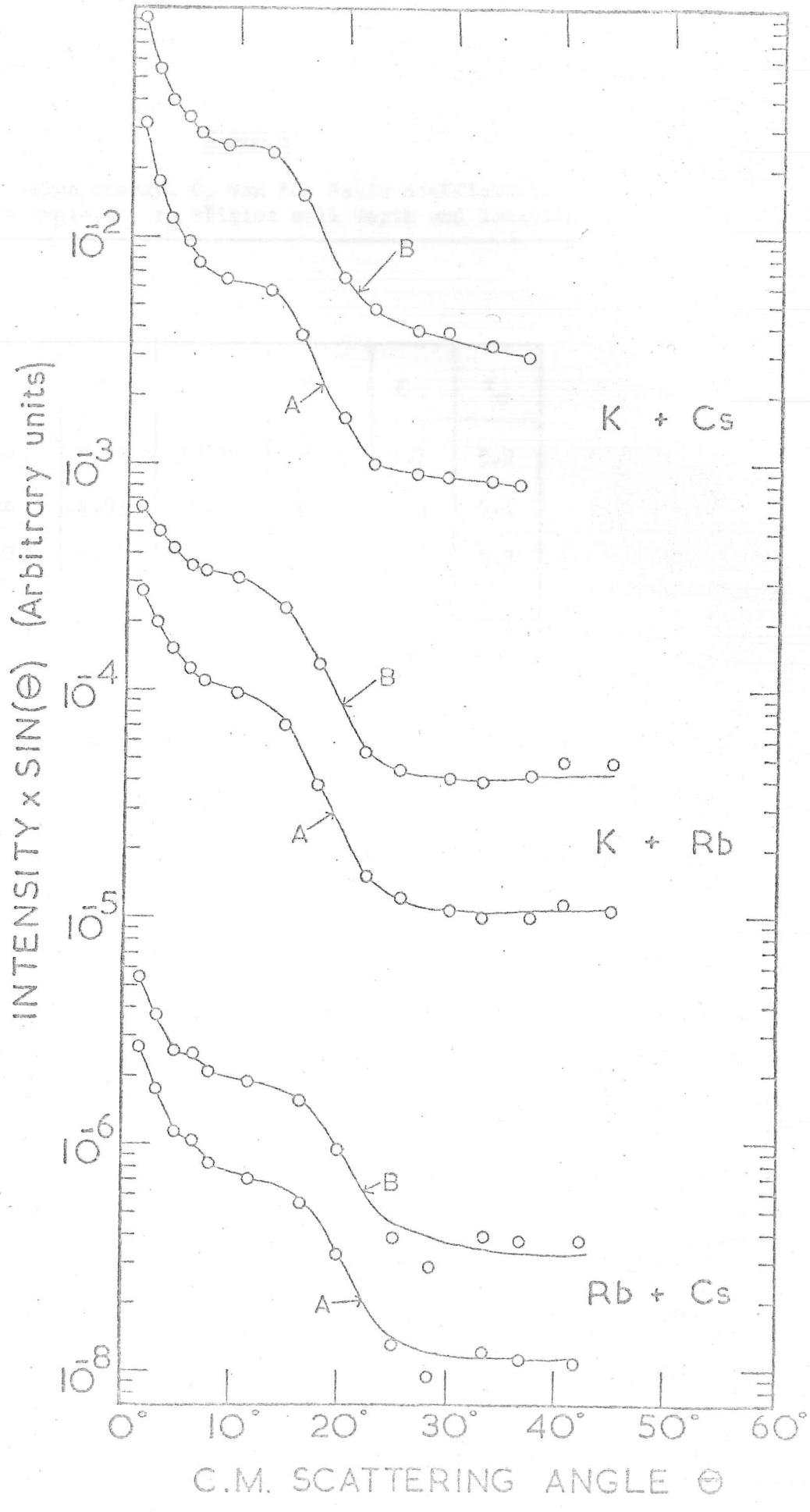

Figure 7 Centre of mass angular distributions for K + Cs, Rb and Rb + Cs. (A) untreated data. (B) corrected to infinitesimal detector height.

TABLE 1

E collision energy, C_6 van der Waals coefficient, θ_r rainbow angle, ϵ , r_m triplet well depth and location

	E	C_6	θ_r	ϵ	r_m
K + Cs	5.02	18.39	16.0	4.7	5.2
K + Rb	4.53	15.61	16.2	4.3	5.1
Rb + Cs	4.17	20.53	19.2	4.6	5.3

Notes: 1) Units. E kcal.mole^{-1}, C_6 x 10^{58} erg cm^6, θ_r degrees, ϵ x 10^{14} ergs, r_m Å.

2) C_6 from Ref.2.

corresponding dimer-atom systems of the previous chapter. For K + Cs, Rb and Rb + Cs rainbow structure is observed, but for K_2 + Cs, Rb and Rb_2 + Cs no such structure is observed. This suggests that for the dimer systems reaction is occurring at impact parameters comparable to the van der Waals radius ($r_m \simeq 5\text{Å}$). Indeed one of the methods of estimating cross sections for these systems, given in the previous chapter, gives maximum impact parameters for reaction of this magnitude.

If the laboratory angular distributions for the systems M + Na and M_2 + Na are matched at small angles ($\Theta_L \leq 5^\circ$) then for negative angles (i.e. the other side of the M_2/M beam from the Na beam) the two distributions are virtually superimposible, the M_2 + Na being slightly more intense at wide negative angles. However at the other side of the M_2/M beam, the scattering from M_2 + Na is as much as three times more intense than the elastic M + Na scattering, before falling below the M + Na intensity at wider angles. The previous chapter shows that this is due to reactive scattering from M_2 + Na peaked at a velocity slightly larger than the M_2 elastic velocity. For the system M_2 + Na the angular range of total scattering (reactive and elastic) is smaller for positive angles than that for elastic M + Na scattering; at negative angles the ranges are about the same, that for M_2 + Na being slightly wider.

References

(1) R. B. Bernstein and J. T. Muckermann, Adv.Chem.Phys.12, 389 (1967).

(2) U. Buck and H. Pauly, Z.Physik 185, 155 (1965).

(3) W. Neumann and H. Pauly, J.Chem.Phys.52, 2548 (1970).

(4) H. Kanes, H. Pauly and E. Vietske, Z.Natur.26, 689 (1971).

(5) E. W. Rothe and R. K. B. Helbing, J.Chem.Phys.49, 4750 (1968).

(6) L. T. Cowley, M. A. D. Fluendy and K. P. Lawley, Trans.Farad. Soc.65, 2027 (1969).

(7) D. E. Pritchard, D. C. Burnham and D. Kleppner, Phys.Rev.Letters 19, 1363 (1967).

(8) P. B. Foreman, G. M. Kendall and R. Grice, Mol.Phys.23, 117 (1972).

(9) D. Beck, J. Chem.Phys.36, 2884 (1962).

(10) D. R. Hardin, work in progress (Cambridge).

(11) D. Beck, Proceedings of the International School of Physics (Enrico Fermi), Course XLIV (Academic Press, 1970) p.15.

(12) E. Hundhausen and H. Pauly, Z.Physik 187, 305 (1965).

Appendix A

The determination of force constants and vibrational frequencies from London-type potential energy surfaces.

The vibrational frequencies of Table 1 in Chapter III are calculated by extension of the methods used by Cashion and Herschbach* for linear symmetric systems. The energy of an X Y Z molecule

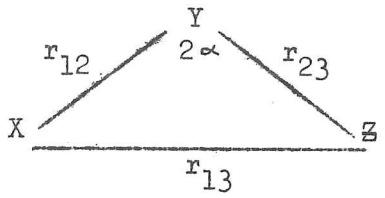

is given by the London equation (equation 3, Chapter III), where the coulomb and exchange integrals, Q, J are obtained from the diatomic singlet and triplet potentials (equation 7, Chapter III). A quadratic expansion of the London equation about the XYZ equilibrium position gives

$$E = \tfrac{1}{2}f_{12}\Delta r_{12}^2 + \tfrac{1}{2}f_{23}\Delta r_{23}^2 + f_{13}\Delta r_{12}\Delta r_{23} + \tfrac{1}{2}f_{\theta}(\Delta\theta)^2 \qquad (1)$$

For a linear symmetric molecule X_3 (i.e. $r_{12} = r_{23} = r$, $r_{13} = 2r$, $2\alpha = 180^{\circ}$) then the force constants ($f_{12} = f_{23}$) are given by

$$f_{12} + f_{13} = \tfrac{3}{4}\,{}^1\Sigma''(r) + \tfrac{1}{4}\,{}^3\Sigma''(r) + 2\,{}^3\Sigma''(2r) \qquad (2a)$$

$$f_{13} = {}^3\Sigma''(2r) + \tfrac{3}{4}[J'(r)]^2/[J(2r)-J(r)] \qquad (2b)$$

$$f_{\theta}/r^2 = -\,{}^3\Sigma'(2r)/(2r) \qquad (2c)$$

For a non linear symmetric molecule XYX (i.e. $r_{12} = r_{23} = r$) then the force constants ($f_{12} = f_{23}$) are given by

$$f_{12} + f_{13} = \tfrac{3}{4}\,{}^1\Sigma''(r) + \tfrac{1}{4}\,{}^3\Sigma''(r) + 2\sin^2\alpha\,.\,{}^3\Sigma''(r_{13}) \qquad (3a)$$

$$f_{13} = \sin^2\alpha\,.\,{}^3\Sigma''(r_{13}) + \tfrac{3}{4}[J'(r)]^2/[J(r_{13})-J(r)] \qquad (3b)$$

$$f_{\theta}/r^2 = -[r_{13}.\sin^2\alpha\,.\,{}^3\Sigma'(r_{13})]/4r^2 + \sin^2\alpha\,.\cos^2\alpha\,.\,{}^3\Sigma''(r_{13}) \qquad (3c)$$

---

*J. K. Cashion and D. R. Herschbach, J.Chem.Phys.40, 2358 (1964).

For a linear non-symmetric molecule XYZ the force constants are

$$f_{12} = Q''_{12} + Q''_{13} - (2S)^{-\frac{1}{2}}\{J''_{12}(2J_{12} - J_{23} - J_{13}) + J'_{12}(2J'_{12} - J'_{13}) + J''_{13}(2J_{13} - J_{12} - J_{23}) + J'_{13}(2J'_{13} - J'_{12})\} + 2^{-\frac{1}{2}}S^{-3/2}\{J'_{12}(2J_{12} - J_{23} - J_{13}) + J'_{13}(2J_{13} - J_{12} - J_{23})\}^2 \quad (4a)$$

$$f_{23} = Q''_{23} + Q''_{13} - (2S)^{-\frac{1}{2}}\{J''_{23}(2J_{23} - J_{12} - J_{13}) + J'_{23}(2J'_{23} - J'_{13}) + J''_{13}(2J_{13} - J_{12} - J_{23}) + J'_{13}(2J'_{13} - J'_{23})\} + 2^{-\frac{1}{2}}S^{-3/2}\{J'_{23}(2J_{23} - J_{12} - J_{13}) + J'_{13}(2J_{13} - J_{12} - J_{23})\}^2 \quad (4b)$$

$$f_{13} = Q''_{13} - (2S)^{-\frac{1}{2}}\{J''_{13}(2J_{13} - J_{12} - J_{23}) + J'_{13}(2J'_{13} - J'_{23}) - J'_{12}(J'_{23} + J'_{13})\} + 2^{-\frac{1}{2}}S^{-3/2}\{J'_{12}(2J_{12} - J_{23} - J_{13}) + J'_{13}(2J_{13} - J_{12} - J_{23})\}\cdot\{J'_{23}(2J_{23} - J_{12} - J_{13}) + J'_{13}(2J_{13} - J_{12} - J_{23})\} \quad (4c)$$

$$f_\theta/r_{12}\cdot r_{23} = -\{Q'_{13} - (2S)^{-\frac{1}{2}}\{J'_{13}(2J_{13} - J_{12} - J_{23})\}\}/r_{13} \quad (4d)$$

where $S = (J_{12} - J_{23})^2 + (J_{23} - J_{13})^2 + (J_{13} - J_{12})^2$

When the surfaces are evaluated including orbital overlap, the expressions for Q and J are given by equation 8 of Chapter III. It is then necessary to replace $^3\Sigma(x)$ by $(1 - S^2)/(1 + S^2)$. $^3\Sigma(x)$ before evaluating the differentials of equations 2 and 3.

The evaluation of the terms of equations 2, 3 and 4 was carried out by numerical differentiation of the appropriate diatomic potential curves at r_{12}, r_{23} and r_{13}. An interval of 0.0005 Å was used for small values of the internuclear distance and of 0.001 Å for larger values. The values of the potentials for these intervals were by Lagrangian interpolation of the diatomic potential data.

The vibrational frequencies were then calculated from the force constants using the standard methods.*

*G. Herzberg, Infrared and Raman Spectra (D. Van Nostrand Company, Inc., Princeton, New Jersey, 1945) Chapter II.